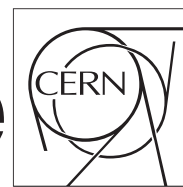


The Compact Muon Solenoid Experiment

CMS Draft Note

Mailing address: CMS CERN, CH-1211 GENEVA 23, Switzerland



2020/12/18

Archive Hash: 84304bd-D

Archive Date: 2020/12/18

Measurements of Higgs differential cross section and interpretations in $H \rightarrow ZZ \rightarrow 4\ell$ ($\ell = e, \mu$) channel

M. Bonanomi², M.S. Chen¹, Q.Y. Guo^{1,4}, T. Javaid^{1,4}, P. Milenovic⁵, V. Milosevic⁵, M. Ahmad⁷, C. Ochando², G. Ortona², R. Salerno², R. Sharma¹, T. Sculac³, and D. Sperka⁶

¹ IHEP, Beijing

² Laboratoire Leprince-Ringuet

³ University of Split

⁴ Beihang University

⁵ University of Belgrade

⁶ Boston University

⁷ Tsinghua University

Abstract

Properties of the Higgs boson are measured in the $H \rightarrow ZZ \rightarrow 4\ell$ ($\ell = e, \mu$) decay channel. A data sample of proton-proton collisions at a center-of-mass energy of 13 TeV is used, corresponding to an integrated luminosity of 137 fb^{-1} recorded by the CMS detector at the LHC. The fiducial cross section is measured with respect to several observables sensitive to production and decay of Higgs where the observed results are compared with POWHEG, MADGRAPH5 and NNLOPS theory predictions. The possible interpretations of the results are reported.

This box is only visible in draft mode. Please make sure the values below make sense.

PDFAuthor: Tahir Javaid

PDFTitle: Measurements of Higgs differential cross section and interpretations in HZZ4 "(=e,") channel

PDFSubject: CMS

PDFKeywords: CMS, your topics

Please also verify that the abstract does not use any user defined symbols

Acknowledgments

Contents

1	Introduction	2
2	EFT interpretations	3
3	Datasets	4
3.1	Data	4
3.2	Simulation	8
4	Objects	11
4.1	Electrons	11
4.2	Muons	27
4.3	Photons for FSR recovery	37
4.4	Jets	37
4.5	Object Summary	42
5	Event Selection	44
5.1	Trigger Selection	44
5.2	Vertex Selection	44
5.3	ZZ Candidate Selection	44
5.4	Choice of the best ZZ Candidate	45
6	Background Estimation	46
6.1	Irreducible Backgrounds	46
6.2	Reducible Background	48
6.3	Rare Backgrounds	69
7	Signal Modelling	71
7.1	Signal modeling of the SM Higgs	71
8	Systematic uncertainties	73
8.1	Systematic uncertainties treatment when combining the data sets	74
9	Yields and distributions	75
9.1	Signal Region Yields	75
9.2	Signal Region Distributions	75
10	Results	79
10.1	Differential Cross Sections and EFT interpretations	80

32 1 Introduction

33 The ATLAS and CMS collaborations first reported the discovery of a new boson in 2012 [1,
 34 2] consistent with the standard model (SM) Higgs boson [3–8] based on proton-proton (pp)
 35 collisions delivered by the CERN LHC at a center-of-mass energy of $\sqrt{s} = 7\text{ TeV}$ in 2011 and
 36 8 TeV in 2012. Subsequent studies by CMS using the full LHC Run 1 data set in various decay
 37 channels and production modes and combined measurements from ATLAS and CMS [9–12]
 38 showed that the properties of the new boson are so far consistent with expectations for the SM
 39 Higgs boson.

40 The $H \rightarrow ZZ \rightarrow 4\ell$ decay channel ($\ell = e, \mu$) has a large signal-to-background ratio due to the
 41 complete reconstruction of the final state decay products and excellent lepton momentum res-
 42 olution and is one of the most important channels for studies of the Higgs boson’s properties.
 43 Measurements performed using this decay channel and the Run 1 data set include the deter-
 44 mination of the mass and spin-parity of the new boson [13–15], its width [16, 17] and fiducial
 45 cross sections [18], as well as tests for anomalous HVV couplings [15, 17].

46 This analysis note presents measurements of properties of the Higgs boson in the $H \rightarrow ZZ \rightarrow$
 47 4ℓ decay channel at $\sqrt{s} = 13\text{ TeV}$ using 137 fb^{-1} of pp collision data collected with the CMS
 48 experiment at the LHC in 2016, 2017 and 2018. Compared to the previous public result [19], the
 49 full available dataset has been fully re-analyzed, with several improvements:

- 50 • analysis of re-recoed 2016 data (17July2018 [20]) and v2 version of the Fall17MiniAOD
 51 for 2017 MC samples.
- 52 • estimation of rare backgrounds ($t\bar{t}+V$, $t\bar{t}+VV$, $VVV\dots$ where V stands for W or Z)
 53 from MC samples (see Section 6.3).
- 54 • development of a BDT combining identification and isolation observables to im-
 55 prove electron selection performance (2016), similar to what was already done for
 56 2017 and 2018 (see Section 4.1.2).
- 57 • improved measurement of lepton scale factors (see Sections 4.1.5, 4.2.5).
- 58 • in-depth studies of jets treatment (implementation of L1 pre-firing emulation for
 59 2016, 2017, removal of noisy jets in 2017, impact assessment of HEM 16/17 failures
 60 in 2018, new and improved Jet Energy Scale and Resolutions corrections for 2018),
 61 see Section 4.4.3.
- 62 • Jet PU-ID properly applied (only for jets with $30 < p_T < 50\text{ GeV}$) as recommended
 63 by the JetMET POG.
- 64 • DeepCSV b-tagging algorithm used for all three years.
- 65 • better binning for differential measurement (especially $p_T(H)$).
- 66 • several additional (production and as well as decay) observables studied with opti-
 67 mized binning.
- 68 • in addition to POWHEG AND NNLOPS, MADGRAPH5 IS USED AS ADDITIONAL
 69 THEORY PREDICTION TO FOR COMPARISON OF THE OBSERVED RESULTS.
- 70 • EFFECTIVE FIELD THEORY (EFT) INTERPRETATION OF DIFFERENTIAL MEASURE-
 71 MENTS ARE ALSO MADE.

2 EFT interpretations

Effective Field Theory (EFT) is an model independent way to parametrize the high enregy scale effects in the enregy scale available to us. The general form of the lagrangian is:

$$\mathcal{L} = \mathcal{L}_{SM} + \mathcal{L}^5 + \mathcal{L}^6 + \mathcal{L}^7 + \dots, \quad \mathcal{L}^{(d)} = \sum_{i=1}^{n_d} \frac{C_i^{(d)}}{\Lambda^{d-4}} Q_i^{(d)} \quad \text{for } d > 4, \quad (1)$$

Where Λ is the New Physics (NP) enregy scale, the parameter $C_i(d)$ are the Wilson Coefficients.

One of most promissing EFT model is the SMEFT [21, 22]. Since the operators $Q_i^{(d)}$ are suppressed by the power of cutoff scale Λ , so we will work with dimension-6 operators only.

Currently, we are trying to produce the Leading Order (LO) ggH process with additional jets upto 2 jets. Like:

```
import model SMEFTsim_A_general_MwScheme_UFO_v2
# import model SMEFTsim_A_general_alphaScheme_UFO_v2
generate p p > h QED=1 NP<=1 @0
add process p p > h j QED=1 NP<=1 @1
add process p p > h j j QED=1 NP<=1 @2
```

Our plan with this is following:

- Generate SM from the SMEFT model and compare it with the NNNLOPS official samples (from HIG-19-001).
- Decide the set of parameter for which our analysis is sensitive.
- Validate the reweight method for our model.
- After finalizing previous step we will try to submit for official full CMSSW simulation.

92 3 Datasets

93 3.1 Data

94 3.1.1 Triggers and Datasets

95 This analysis uses a data sample recorded by the CMS experiment during 2016, 2017 and 2018,
 96 corresponding to 137 fb^{-1} of data.

97 The datasets used for 2016, 2017 and 2018 data taking are listed in Tables 1, 3, and 5, respec-
 98 tively, along with the integrated luminosity. The analysis relies on four different primary
 99 datasets (PDs), *DoubleMuon*, *MuEG*, *EGamma* (or *DoubleEG* and *SingleElectron* for 2016 and
 100 2017), and *SingleMuon*, each of which combines a certain collections of HLT paths. To avoid
 101 duplicate events from different primary datasets, events are taken:

- 102 • from EGamma if they pass the diEle or triEle or singleElectron triggers,
- 103 • from DoubleMuon if they pass the diMuon or triMuon triggers and fail the diEle
 104 and triEle triggers,
- 105 • from MuEG if they pass the MuEle or MuDiEle or DiMuEle triggers and fail the
 106 diEle, triEle, singleElectron, diMuon and triMuon triggers,
- 107 • from SingleMuon if they pass the singleMuon trigger and fail all the above triggers.

108 The HLT paths used for 2016, 2017 and 2018 collision data are listed in Tables 2, 4 and 6, respec-
 109 tively.

Run-range	Dataset	Integrated luminosity
272007-275376	/DoubleMuon/Run2016B-17Jul2018-v1/MINIAOD /DoubleEG/Run2016B-17Jul2018-v1/MINIAOD /MuonEG/Run2016B-17Jul2018-v1/MINIAOD /SingleElectron/Run2016B-17Jul2018-v1/MINIAOD /SingleMuon/Run2016B-17Jul2018-v1/MINIAOD	5.892 fb^{-1}
275657-276283	/DoubleMuon/Run2016C-17Jul2018-v1/MINIAOD /DoubleEG/Run2016C-17Jul2018-v1/MINIAOD /MuonEG/Run2016C-17Jul2018-v1/MINIAOD /SingleElectron/Run2016C-17Jul2018-v1/MINIAOD /SingleMuon/Run2016C-17Jul2018-v1/MINIAOD	2.646 fb^{-1}
276315-276811	/DoubleMuon/Run2016D-17Jul2018-v1/MINIAOD /DoubleEG/Run2016D-17Jul2018-v1/MINIAOD /MuonEG/Run2016D-17Jul2018-v1/MINIAOD /SingleElectron/Run2016D-17Jul2018-v1/MINIAOD /SingleMuon/Run2016D-17Jul2018-v1/MINIAOD	4.353 fb^{-1}
276831-277420	/DoubleMuon/Run2016E-17Jul2018-v1/MINIAOD /DoubleEG/Run2016E-17Jul2018-v1/MINIAOD /MuonEG/Run2016E-17Jul2018-v1/MINIAOD /SingleElectron/Run2016E-17Jul2018-v1/MINIAOD /SingleMuon/Run2016E-17Jul2018-v1/MINIAOD	4.117 fb^{-1}
277772-278808	/DoubleMuon/Run2016F-17Jul2018-v1/MINIAOD /DoubleEG/Run2016F-17Jul2018-v1/MINIAOD /MuonEG/Run2016F-17Jul2018-v1/MINIAOD /SingleElectron/Run2016F-17Jul2018-v1/MINIAOD /SingleMuon/Run2016F-17Jul2018-v1/MINIAOD	3.186 fb^{-1}
278820-280385	/DoubleMuon/Run2016G-17Jul2018-v1/MINIAOD /DoubleEG/Run2016G-17Jul2018-v1/MINIAOD /MuonEG/Run2016G-17Jul2018-v1/MINIAOD /SingleElectron/Run2016G-17Jul2018-v1/MINIAOD /SingleMuon/Run2016G-17Jul2018-v1/MINIAOD	7.721 fb^{-1}
280919-284044	/DoubleMuon/Run2016H-17Jul2018-v1/MINIAOD /DoubleEG/Run2016H-17Jul2018-v1/MINIAOD /MuonEG/Run2016H-17Jul2018-v1/MINIAOD /SingleElectron/Run2016H-17Jul2018-v1/MINIAOD /SingleMuon/Run2016H-17Jul2018-v1/MINIAOD /DoubleMuon/Run2016H-17Jul2018-v1/MINIAOD /DoubleEG/Run2016H-17Jul2018-v1/MINIAOD /MuonEG/Run2016H-17Jul2018-v1/MINIAOD /SingleElectron/Run2016H-17Jul2018-v1/MINIAOD /SingleMuon/Run2016H-17Jul2018-v1/MINIAOD	8.857 fb^{-1}

Table 1: Datasets used in the 2016 analysis.

HLT path	prescale	primary dataset
HLT_Ele17_Ele12_CaloIdL_TrackIdL_IsoVL_DZ	1	DoubleEG
HLT_Ele23_Ele12_CaloIdL_TrackIdL_IsoVL_DZ	1	DoubleEG
HLT_DoubleEle33_CaloIdL_GsfTrkIdVL	1	DoubleEG
HLT_Ele16_Ele12_Ele8_CaloIdL_TrackIdL	1	DoubleEG
HLT_Mu17_TrkIsoVVL_Mu8_TrkIsoVVL	1	DoubleMuon
HLT_Mu17_TrkIsoVVL_TkMu8_TrkIsoVVL	1	DoubleMuon
HLT_TripleMu_12_10_5	1	DoubleMuon
HLT_Mu8_TrkIsoVVL_Ele17_CaloIdL_TrackIdL_IsoVL	1	MuonEG
HLT_Mu8_TrkIsoVVL_Ele23_CaloIdL_TrackIdL_IsoVL	1	MuonEG
HLT_Mu17_TrkIsoVVL_Ele12_CaloIdL_TrackIdL_IsoVL	1	MuonEG
HLT_Mu23_TrkIsoVVL_Ele12_CaloIdL_TrackIdL_IsoVL	1	MuonEG
HLT_Mu23_TrkIsoVVL_Ele8_CaloIdL_TrackIdL_IsoVL	1	MuonEG
HLT_Mu8_DiEle12_CaloIdL_TrackIdL	1	MuonEG
HLT_DiMu9_Ele9_CaloIdL_TrackIdL	1	MuonEG
HLT_Ele25_eta2p1_WPTight	1	SingleElectron
HLT_Ele27_WPTight	1	SingleElectron
HLT_Ele27_eta2p1_WPLoose_Gsf	1	SingleElectron
HLT_IsoMu20 OR HLT_IsoTkMu20	1	SingleMuon
HLT_IsoMu22 OR HLT_IsoTkMu22	1	SingleMuon

Table 2: Trigger paths used in 2016 collision data.

Run-range	Dataset	Integrated luminosity
297046-299329	/DoubleMuon/Run2017B-17Nov2017-v1/MINIAOD /DoubleEG/Run2017B-17Nov2017-v1/MINIAOD /MuonEG/Run2017B-17Nov2017-v1/MINIAOD /SingleElectron/Run2017B-17Nov2017-v1/MINIAOD /SingleMuon/Run2017B-17Nov2017-v1/MINIAOD	4.792 fb ⁻¹
299368-300676	/DoubleMuon/Run2017C-17Nov2017-v1/MINIAOD /DoubleEG/Run2017C-17Nov2017-v1/MINIAOD /MuonEG/Run2017C-17Nov2017-v1/MINIAOD /SingleElectron/Run2017C-17Nov2017-v1/MINIAOD /SingleMuon/Run2017C-17Nov2017-v1/MINIAOD	9.755 fb ⁻¹
302030-303434	/DoubleMuon/Run2017D-17Nov2017-v1/MINIAOD /DoubleEG/Run2017D-17Nov2017-v1/MINIAOD /MuonEG/Run2017D-17Nov2017-v1/MINIAOD /SingleElectron/Run2017D-17Nov2017-v1/MINIAOD /SingleMuon/Run2017D-17Nov2017-v1/MINIAOD	4.319 fb ⁻¹
303824-304797	/DoubleMuon/Run2017E-17Nov2017-v1/MINIAOD /DoubleEG/Run2017E-17Nov2017-v1/MINIAOD /MuonEG/Run2017E-17Nov2017-v1/MINIAOD /SingleElectron/Run2017E-17Nov2017-v1/MINIAOD /SingleMuon/Run2017E-17Nov2017-v1/MINIAOD	9.424 fb ⁻¹
305040-306462	/DoubleMuon/Run2017F-17Nov2017-v1/MINIAOD /DoubleEG/Run2017F-17Nov2017-v1/MINIAOD /MuonEG/Run2017F-17Nov2017-v1/MINIAOD /SingleElectron/Run2017F-17Nov2017-v1/MINIAOD /SingleMuon/Run2017F-17Nov2017-v1/MINIAOD	13.50 fb ⁻¹
278820-280385	/DoubleMuon/Run2017G-PromptReco-v1/MINIAOD /DoubleEG/Run2017G-PromptReco-v1/MINIAOD /MuonEG/Run2017G-PromptReco-v1/MINIAOD /SingleElectron/Run2017G-PromptReco-v1/MINIAOD /SingleMuon/Run2017G-PromptReco-v1/MINIAOD	7.721 fb ⁻¹
281207-284068	/DoubleMuon/Run2017H-PromptReco-v1/MINIAOD /DoubleEG/Run2017H-PromptReco-v1/MINIAOD /MuonEG/Run2017H-PromptReco-v1/MINIAOD /SingleElectron/Run2017H-PromptReco-v1/MINIAOD /SingleMuon/Run2017H-PromptReco-v1/MINIAOD /DoubleMuon/Run2017H-PromptReco-v2/MINIAOD /DoubleEG/Run2017H-PromptReco-v2/MINIAOD /MuonEG/Run2017H-PromptReco-v2/MINIAOD /SingleElectron/Run2017H-PromptReco-v2/MINIAOD /SingleMuon/Run2017H-PromptReco-v2/MINIAOD /DoubleMuon/Run2017H-PromptReco-v3/MINIAOD /DoubleEG/Run2017H-PromptReco-v3/MINIAOD /MuonEG/Run2017H-PromptReco-v3/MINIAOD /SingleElectron/Run2017H-PromptReco-v3/MINIAOD /SingleMuon/Run2017H-PromptReco-v3/MINIAOD	8.857 fb ⁻¹

Table 3: Datasets used in the 2017 analysis.

HLT path	prescale	primary dataset
HLT_Ele23_Ele12_CaloIdL_TrackIdL_IsoVL_*	1	DoubleEG
HLT_DoubleEle33_CaloIdL_GsfTrkIdVL	1	DoubleEG
HLT_Ele16_Ele12_Ele8_CaloIdL_TrackIdL	1	DoubleEG
HLT_Mu17_TrkIsoVVL_Mu8_TrkIsoVVL_DZ_Mass3p8	1	DoubleMuon
HLT_Mu17_TrkIsoVVL_Mu8_TrkIsoVVL_DZ_Mass8	1	DoubleMuon
HLT_TripleMu_12_10_5	1	DoubleMuon
HLT_TripleMu_10_5_5_D2	1	DoubleMuon
HLT_Mu23_TrkIsoVVL_Ele12_CaloIdL_TrackIdL_IsoVL	1	MuonEG
HLT_Mu8_TrkIsoVVL_Ele23_CaloIdL_TrackIdL_IsoVL_DZ	1	MuonEG
HLT_Mu12_TrkIsoVVL_Ele23_CaloIdL_TrackIdL_IsoVL_DZ	1	MuonEG
HLT_Mu23_TrkIsoVVL_Ele12_CaloIdL_TrackIdL_IsoVL_DZ	1	MuonEG
HLT_DiMu9_Ele9_CaloIdL_TrackIdL_DZ	1	MuonEG
HLT_Mu8_DiEle12_CaloIdL_TrackIdL	1	MuonEG
HLT_Mu8_DiEle12_CaloIdL_TrackIdL_DZ	1	MuonEG
HLT_Ele35_WPTight_Gsf_v*	1	SingleElectron
HLT_Ele38_WPTight_Gsf_v*	1	SingleElectron
HLT_Ele40_WPTight_Gsf_v*	1	SingleElectron
HLT_IsoMu27	1	SingleMuon

Table 4: Trigger paths used in 2017 collision data.

Run-range	Dataset	Integrated luminosity
315252-316995	/DoubleMuon/Run2018A-17Sep2018-v2/MINIAOD /MuonEG/Run2018A-17Sep2018-v1/MINIAOD /EGamma/Run2018A-17Sep2018-v2/MINIAOD /SingleMuon/Run2018A-17Sep2018-v2/MINIAOD	X.XXX fb ⁻¹
317080-319310	/DoubleMuon/Run2018B-17Sep2018-v1/MINIAOD /MuonEG/Run2018B-17Sep2018-v1/MINIAOD /EGamma/Run2018B-17Sep2018-v1/MINIAOD /SingleMuon/Run2018B-17Sep2018-v1/MINIAOD	X.XXX fb ⁻¹
319337-320065	/DoubleMuon/Run2018C-17Sep2018-v1/MINIAOD /MuonEG/Run2018C-17Sep2018-v1/MINIAOD /EGamma/Run2018C-17Sep2018-v1/MINIAOD /SingleMuon/Run2018C-17Sep2018-v1/MINIAOD	X.XXX fb ⁻¹
320673-325175	/DoubleMuon/Run2018D-PromptReco-v2/MINIAOD /MuonEG/Run2018D-PromptReco-v2/MINIAOD /EGamma/Run2018D-PromptReco-v2/MINIAOD /SingleMuon/Run2018D-PromptReco-v2/MINIAOD	X.XXX fb ⁻¹

Table 5: Datasets used in the 2018 analysis.

HLT path	prescale	primary dataset
HLT_Ele23_Ele12_CaloIdL_TrackIdL_IsoVL_v*	1	DoubleEG
HLT_DoubleEle25_CaloIdL_MW_v*	1	DoubleEG
HLT_Mu17_TrkIsoVVL_Mu8_TrkIsoVVL_DZ_Mass3p8_v*	1	DoubleMuon
HLT_Mu23_TrkIsoVVL_Ele12_CaloIdL_TrackIdL_IsoVL_v*	1	MuonEG
HLT_Mu8_TrkIsoVVL_Ele23_CaloIdL_TrackIdL_IsoVL_DZ_v*	1	MuonEG
HLT_Mu12_TrkIsoVVL_Ele23_CaloIdL_TrackIdL_IsoVL_DZ_v*	1	MuonEG
HLT_DiMu9_Ele9_CaloIdL_TrackIdL_DZ_v*	1	MuonEG
HLT_Ele32_WPTight_Gsf_v*	1	SingleElectron
HLT_IsoMu24_v*	1	SingleMuon

Table 6: Trigger paths used in 2018 collision data.

110 **3.1.2 Trigger Efficiency**

111 The efficiency in data of the combination of triggers used in the analysis with respect to the
 112 offline reconstruction and selection is measured by considering 4ℓ events triggered by single
 113 lepton triggers. One of the four reconstructed leptons (the “tag”) is geometrically matched to
 114 a trigger object passing the final filter of one of the single muon or single electron triggers. The
 115 other three leptons are used as “probes”. In each 4ℓ event there are up to 4 possible tag-probe
 116 combinations, and all possible combinations are counted in the denominator of the efficiency.
 117 For each of the three probe leptons all matching trigger filter objects are collected. Then the
 118 matched trigger filter objects of the three probe leptons are combined in attempt to reconstruct
 119 any of the triggers used in the analysis. If any of the analysis triggers can be formed using the
 120 probe leptons, the set of probes is also counted in the numerator of the efficiency.

121 This method does not have a perfect closure in MC events due to the fact that the presence of
 122 a fourth lepton increases the trigger efficiency, and this effect is not accounted for. Also, in the
 123 $2e2\mu$ final state, the three probe leptons cannot be combined to form all possible triggers which
 124 can collect events with two electrons and two muons (e.g. if the tag lepton is an electron, the
 125 three remaining leptons cannot pass a double electron trigger). Therefore the method is also
 126 applied on MC and the difference between data and MC is used to determine the reliability
 127 of the simulation. The efficiency plotted as a function of the minimum p_T of the three probe
 128 leptons in data and MC using this method can be seen in Fig. 1 that shows the trigger efficiency
 129 in 2018 data for different final states. The MC efficiency describes well the data within the
 130 statistical uncertainties.

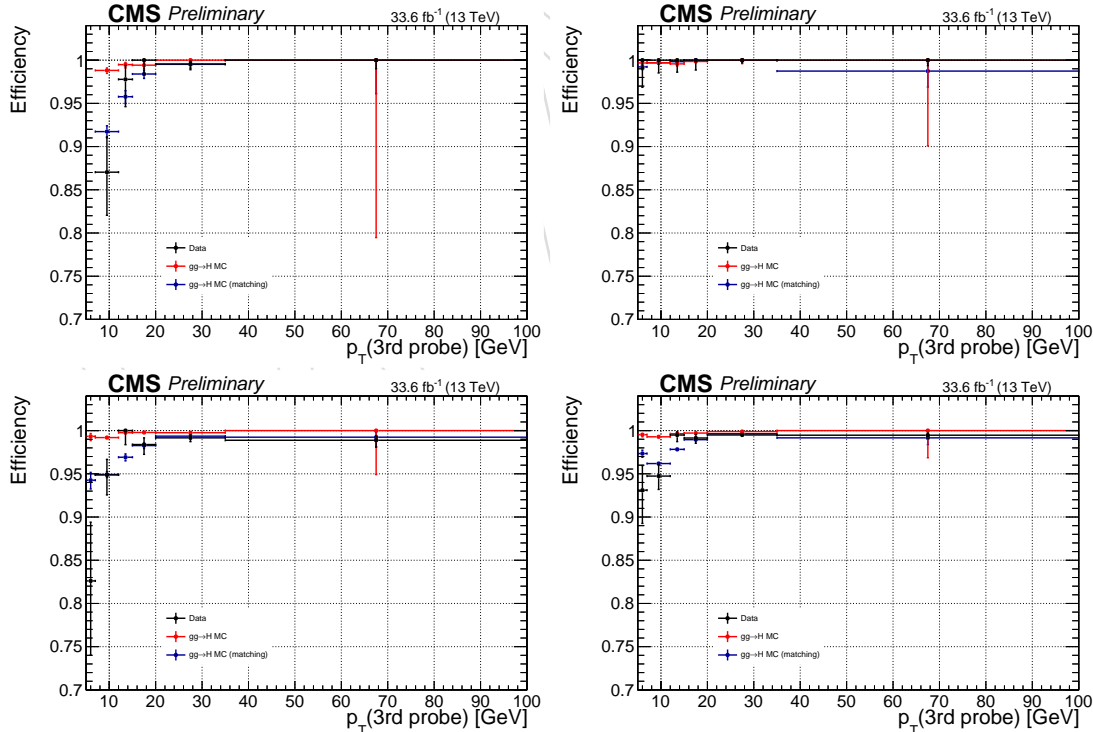


Figure 1: Trigger efficiency measured in 2016 data using 4ℓ events collected by single lepton triggers for the $4e$ (top left), 4μ (top right), $2e2\mu$ (bottom left) and 4ℓ (bottom right) final states.

131 A summary of the trigger efficiencies in MC truth, and in MC and data using the tag and probe
 132 method are summarized in table 7. The trigger efficiency in simulation is found to be $> 99\%$ in

133 each final state.

Final State	$gg \rightarrow H$ MC	$gg \rightarrow H$ MC (matching)	Data (matching)
$4e$	$0.991^{+.002}_{-.002}$	$0.948^{+.004}_{-.004}$	$0.982^{+.005}_{-.007}$
4μ	$0.997^{+.001}_{-.001}$	$0.997^{+.001}_{-.001}$	$1.000^{+.000}_{-.001}$
$2e2\mu$	$0.995^{+.001}_{-.001}$	$0.964^{+.002}_{-.002}$	$0.983^{+.003}_{-.004}$

Table 7: Trigger efficiencies measured using 4ℓ events in 2018 data.

134 3.2 Simulation

135 3.2.1 Signal Samples

136 Descriptions of the SM Higgs boson production are obtained using the POWHEG V2 [23–25]
 137 generator for the five main production modes: gluon fusion ($gg \rightarrow H$) including quark mass
 138 effects [26], vector boson fusion (VBF) [27], and associated production (WH, ZH and $t\bar{t} H$ [28]).
 139 In the case of WH and ZH the MiNLO HVJ extension of POWHEG is used [29]. The description
 140 of the decay of the Higgs boson to four leptons is obtained using the JHUGEN generator [30]. In
 141 the case of WH, ZH and $t\bar{t} H$, the Higgs boson is allowed to decay to $H \rightarrow ZZ \rightarrow 2\ell^2X$ such that
 142 4-lepton events where two leptons originate from the decay of associated Z, W bosons or top
 143 quarks are also taken into account in the simulation. Showering of parton-level events is done
 144 using PYTHIA8.209, and in all cases matching is performed by allowing QCD emissions at all
 145 energies in the shower and vetoing them afterwards according to the POWHEG internal scale.
 146 All samples are generated with the NNPDF 3.1 NLO parton distribution functions (PDFs) [31].
 147 The list of signal samples and their cross sections are shown in Table 8.

148 3.2.2 Background Samples

149 Production of ZZ via quark-antiquark annihilation is generated at next-to-leading order (NLO)
 150 using POWHEG V2 [32] and PYTHIA8, with the same settings as for the Higgs signal. As this
 151 simulation covers a large range of ZZ invariant masses, dynamical QCD factorization and
 152 renormalization scales have been chosen, equal to m_{ZZ} .

153 The $gg \rightarrow ZZ$ process is simulated at leading order (LO) with MCFM [33, 34]. In order to match
 154 the $gg \rightarrow H \rightarrow ZZ$ transverse momentum spectra predicted by POWHEG at NLO, the showering
 155 for MCFM samples is performed with different PYTHIA8 settings, allowing only emissions up
 156 to the parton-level scale (“wimpy” shower).

157 Although not directly used to model data observations, additional MC samples of WZ, Drell-
 158 Yan+jets, $t\bar{t}$, and tribosons are generated using MADGRAPH5_AMC@NLO [35] either inclu-
 159 sively or merging several jet multiplicities, as detailed in the table. Table 9 summarizes the MC
 160 simulation datasets used for this analysis.

Process	Dataset Name	$\sigma \times BR(\times \epsilon_{\text{filter}})$
$gg \rightarrow H \rightarrow ZZ \rightarrow 4\ell$	/GluGluHToZZTo4L_M125_13TeV_powheg2_JHUGenV709_pythia8/[1]	12.18 fb
$qq \rightarrow Hqq \rightarrow ZZqq \rightarrow 4\ell qq$	/VBF_HToZZTo4L_M125_13TeV_powheg2_JHUGenV709_pythia8/[1]	1.044 fb
$q\bar{q} \rightarrow W^+H \rightarrow W^+ZZ \rightarrow 4\ell + X$	/WplusH_HToZZTo4L_M125_13TeV_powheg2-minlo-HWJ_JHUGenV709_pythia8/[1]	0.232 fb
$q\bar{q} \rightarrow W^-H \rightarrow W^-ZZ \rightarrow 4\ell + X$	/WminusH_HToZZTo4L_M125_13TeV_powheg2-minlo-HWJ_JHUGenV709_pythia8/[1]	0.147 fb
$q\bar{q} \rightarrow ZH \rightarrow ZZZ \rightarrow 4\ell + X$	/ZH_HToZZ_4LFilter_M125_13TeV_powheg2-minlo-HZJ_JHUGenV709_pythia8/[1]	0.668 fb
$gg \rightarrow ttH \rightarrow ttZZ \rightarrow 4\ell + X$	/ttH_HToZZ_4LFilter_M125_13TeV_powheg_JHUGenV709_pythia8/[1]	0.393 fb
$gg \rightarrow bbH \rightarrow bbZZ \rightarrow 4\ell + X$	/bbH_HToZZTo4L_M125_13TeV_JHUGenV7011_pythia8/[1]	0.135 fb
$q\bar{q}/qg \rightarrow tHq \rightarrow tqZZ \rightarrow 4\ell + X$	/tqH_HToZZTo4L_M125_13TeV_JHUGenV7011_pythia8/[1]	0.0213 fb

[1] RunIIAutumn18MiniAOD-102X_upgrade2018_realistic_v15

Table 8: Signal Monte Carlo samples and cross sections.

Process	Dataset Name	$\sigma \cdot BR$
$qq \rightarrow ZZ \rightarrow 4\ell$	/ZZTo4L_13TeV_powheg_pythia8/[1]	1.256 pb
$qq \rightarrow ZZ \rightarrow 4\ell$	/ZZTo4L_13TeV-amcatnloFXFX-pythia8/[1]	1.212 pb
$gg \rightarrow ZZ \rightarrow 4e$	/GluGluToContinToZZTo4e_13TeV_MCFM701/[1]	0.00159 pb
$gg \rightarrow ZZ \rightarrow 4\mu$	/GluGluToContinToZZTo4mu_13TeV_MCFM701/[1]	0.00159 pb
$gg \rightarrow ZZ \rightarrow 4\tau$	/GluGluToContinToZZTo4tau_13TeV_MCFM701/[1]	0.00159 pb
$gg \rightarrow ZZ \rightarrow 2e2\mu$	/GluGluToContinToZZTo2e2mu_13TeV_MCFM701/[1]	0.00319 pb
$gg \rightarrow ZZ \rightarrow 2e2\tau$	/GluGluToContinToZZTo2e2tau_13TeV_MCFM701/[1]	0.00319 pb
$gg \rightarrow ZZ \rightarrow 2\mu2\tau$	/GluGluToContinToZZTo2mu2tau_13TeV_MCFM701/[1]	0.00319 pb
$Z \rightarrow \ell\ell + \text{jets}$	/DYJetsToLL_M-50.TuneCUETP8M1_13TeV-amcatnloFXFX-pythia8/[1]	6104 pb
$Z \rightarrow \ell\ell + \text{jets}$	/DYJetsToLL_M-10to50.TuneCUETP8M1_13TeV-amcatnloFXFX-pythia8/[1]	18610 pb
$WZ \rightarrow 3\ell\nu$	/WZTo3LNu_TuneCUETP8M1_13TeV-powheg-pythia8/[1]	4.430 pb
$t\bar{t}$	/TTJets_TuneCUETP8M1_13TeV-amcatnloFXFX-pythia8/[1]	815.96 pb
$t\bar{t} \rightarrow 2\ell 2\nu 2b$	/TTTo2L2Nu_13TeV-powheg/[1]	87.31 pb
ZZZ	/ZZZ_TuneCUETP8M1_13TeV-amcatnlo-pythia8/[1]	0.01398 pb
WZZ	/WZZ_TuneCUETP8M1_13TeV-amcatnlo-pythia8/[1]	0.05565 pb
WWZ	/WWZ_TuneCUETP8M1_13TeV-amcatnlo-pythia8/[1]	0.1651 pb
$t\bar{t}+ZZ$	/TTZZ_TuneCUETP8M2T4_13TeV-madgraph-pythia8/[1]	0.001572 pb
$t\bar{t}+WW$	/TTWW_TuneCUETP8M2T4_13TeV-madgraph-pythia8/[1]	0.007883 pb
$t\bar{t}+Z$	/ttZJets_13TeV_madgraphMLM/[1]	0.259 pb

where [1] = RunIIISummer16MiniAODv3-PUMoriond17_94X_mcRun2_asymptotic_v* for 2016,

[1] = RunIIFall17MiniAODv2-PU2017_12Apr2018_94X_mc2017_realistic_v* for 2017,

[1] = RunIIIAutumn18MiniAOD-102X_upgrade2018_realistic_v1* for 2018.

Table 9: Background Monte Carlo samples and cross sections.

3.2.3 Pileup Reweighting

- For each year, corresponding simulation samples are reweighted to match the pileup distribution in data, as shown on the Fig. 2. The minimum bias cross-section used for each year is 69.2 mb.

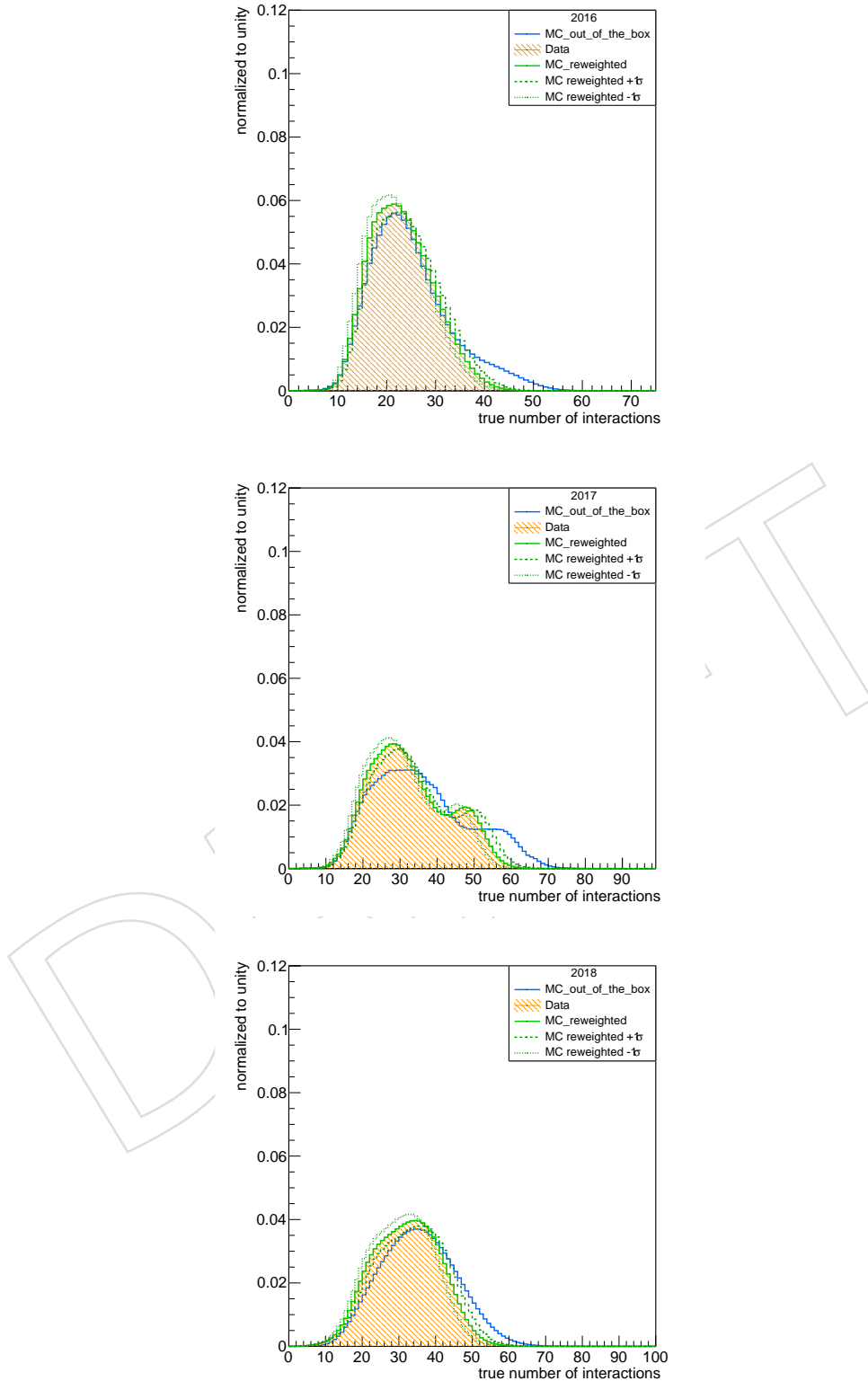


Figure 2: Distribution of pileup in 2016 (top), 2017 (middle) and 2018 (bottom) MC and Data shown before and after the application of PU weights. Up and down variations of 5% in the minimum bias cross section when calculating the weights are also shown.

165 4 Objects

166 The reconstruction of the SM Higgs boson in the decay chain $H \rightarrow ZZ \rightarrow 4\ell$ requires very
167 efficient lepton reconstruction and identification in order to be sensitive to a low mass Higgs,
168 for which at least one of the leptons has a p_T within the range 5 - 15 GeV. In this kinematic
169 region the need is for an optimal efficiency, while retaining the rate of misidentified leptons
170 low enough. On the same time, to allow a precise measurement of the Higgs boson mass and
171 together properties, which depend on the lepton kinematics, the analysis needs a precise mo-
172 mentum measurement. For both reasons, the analysis will make use of high statistics sources
173 of prompt leptons to measure efficiency, mis-identification rate, and energy scale/resolution.

174 In this chapter we describe the selection of leptons and jets and the calibrations done on data
175 control samples relevant for this analysis.

176 4.1 Electrons

177 4.1.1 Electron Reconstruction

178 More details on electron reconstruction can be found in Ref. [36].

179 Electron candidates are preselected using loose cuts on track-cluster matching observables, so
180 as to preserve the highest possible efficiency while rejecting part of the QCD background. To be
181 considered for the analysis, electrons are required to have a transverse momentum $p_T^e > 7$ GeV,
182 a reconstructed $|\eta^e| < 2.5$, and to satisfy a loose primary vertex constraint defined as $d_{xy} < 0.5$
183 cm and $d_z < 1$ cm. Such electrons are called **loose electrons**.

184 The data-MC discrepancy is corrected using scale factors as is done for the electron selection
185 with data efficiencies measured using the same tag-and-probe technique outlined later (see
186 Section 4.1.5). These studies for reconstructions are carried out by the EGM POG and the results
187 are only summarised here.

188 The electron reconstruction scale factors are shown Fig. 3 and are applied as a function of the
189 super cluster η and electron p_T .

190 4.1.2 Electron Identification and Isolation

191 One of the main improvements brought in the analysis is the usage of a new multivariate dis-
192 criminant for electron selection in all data taking periods.

193 Reconstructed electrons are now identified and isolated by means of an eXtreme Gradient
194 Boosting (XGBoost) optimized distributed gradient boosting library designed to be highly ef-
195 ficient, flexible and portable. It implements machine learning algorithms under the Gradient
196 Boosting framework and exploits observables from the electromagnetic cluster, the matching
197 between the cluster and the electron track, observables based exclusively on tracking mea-
198 surements as well as particle flow isolation sums. The full list of used features can be found in the
199 Table 10.

200 The model is trained on 2016, 2017, and 2018 Drell-Yan with jets MC sample for both signal and
201 background. The separate training for three periods guarantees optimal performance during
202 the whole Run 2 data taking period. The simulated samples used to train the model are listed
203 bellow.

204 • 2016

205 /DYJetsToLL_M-50_TuneCUETP8M1_13TeV-amcatnloFXFX-pythia8/RunIIISummer16MiniaO

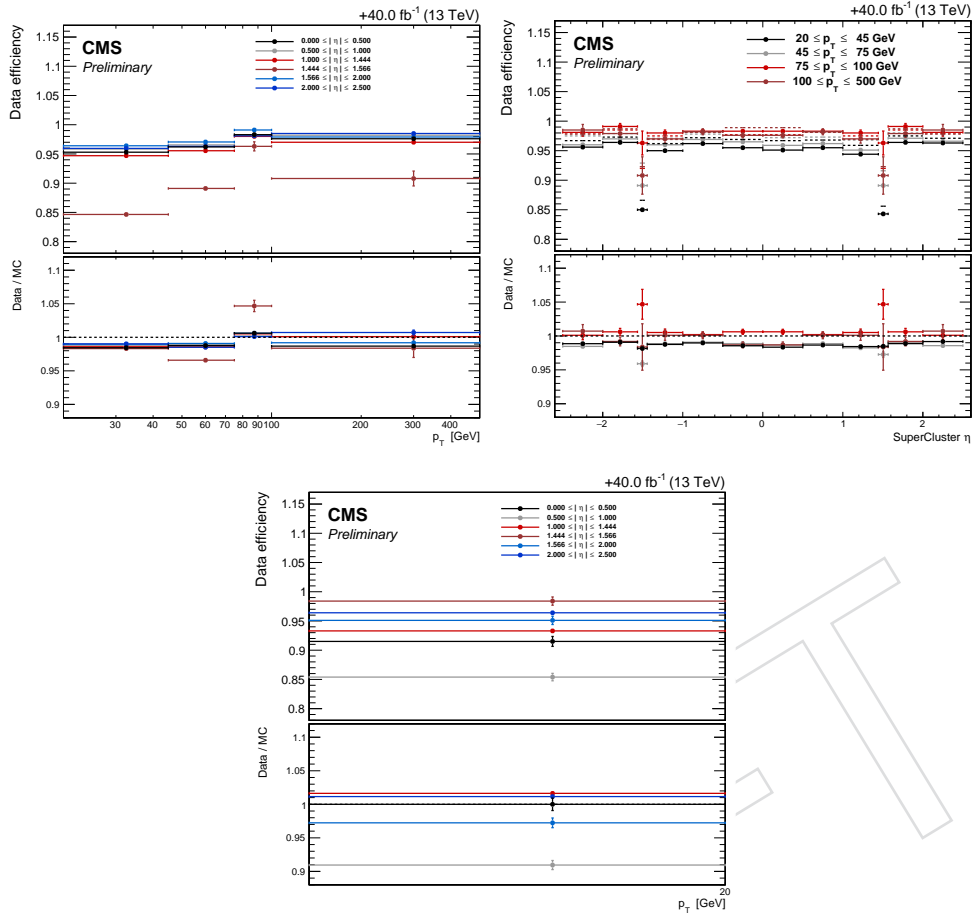


Figure 3: Electron reconstruction efficiencies efficiency in data versus p_T (left) and η (right) for electrons with $p_T > 20$ GeV (top) and $p_T < 20$ GeV (bottom) with corresponding data/MC scale factors as provided by the EGM POG. Errors are statistical only.

• 2017

/DYJetsToLL_M-50_TuneCP5_13TeV-madgraphMLM-pythia8/RunIIFall17MiniAOD-RECO

• 2018

/DYJetsToLL_M-50_TuneCP5_13TeV-madgraphMLM-pythia8/RunIIAutumn18MiniAOD-102X

Several studies have been conducted on 2016 Drell-Yan with jets MC sample. The XGBoost framework was first used in 2017 and the model was trained on 2017 Drell-Yan with jets MC sample. This model is known as 2017 ID+ISO V2. The same framework was then used to train the model on 2016 MC (2016 ID+ISO) and finally on 2018 MC (2018 ID+ISO). In Fig. 4 one can see the ROC curves obtained using 2016 Drell-Yan with jets MC sample. As expected, the model trained on 2016 MC using electron identification and isolation features outperforms the model trained on 2016 MC using only identification features and the model obtained after applying 2017 ID+ISO V2 training on 2016 Drell-Yan with jets MC sample.

In Fig. 5 one can see the ROC curve for the model trained on 2016 MC using electron identification and isolation features and ROC curve when applying sequential approach meaning applying isolation cut after cutting on the distribution obtained by training using only identification features. As expected, the model obtained using electron identification and isolation

222 features outperforms the sequential approach model.

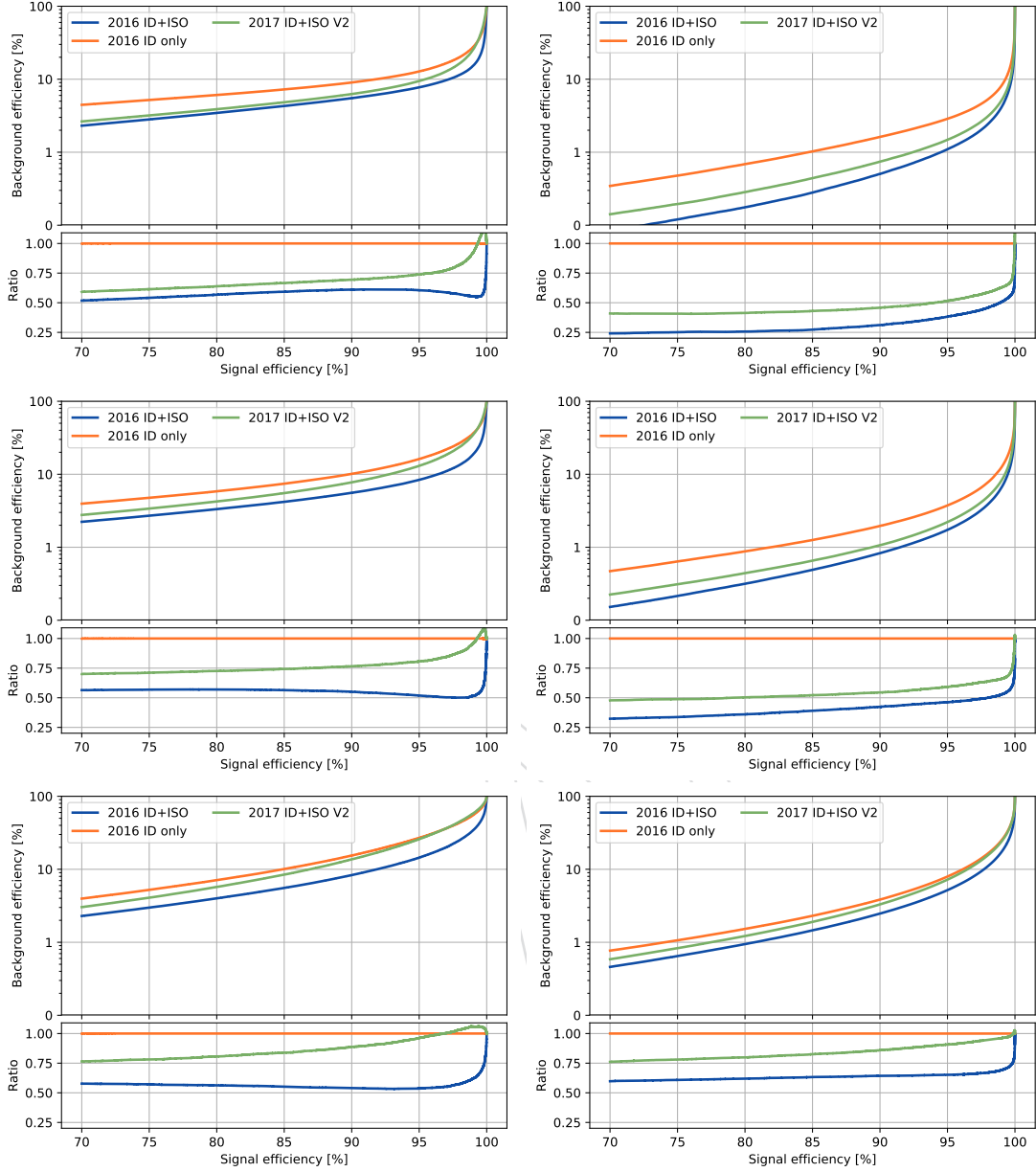


Figure 4: The receiver operating characteristic curves, representing the background efficiency vs signal efficiency, of the MVA trained on 2016 Drell-Yan with jets MC sample. Performance are shown for electrons with $5 < p_T < 10$ GeV (left), $p_T > 10$ GeV (right), and $|\eta| < 0.8$ (top), $0.8 < |\eta| < 1.479$ (middle), and $|\eta| > 1.479$ (bottom).

223 The Fig. 6 shows output of the multiclassifier discriminant i.e. MVA score for prompt electrons
 224 from Drell-Yan events and misidentified electrons originating from jets in Drell-Yan events. The
 225 performance of model trained on 2018 MC using electron identification and isolation features
 226 outperforms the model obtained after applying 2017 ID+ISO V2 training on 2018 Drell-Yan
 227 with jets MC sample as shown in Fig. 7.

228 The impact of the transition from the TMVA (V1) to the XGBoost(V2) training framework is
 229 shown in Fig. 8, showing a noticeable improvement.

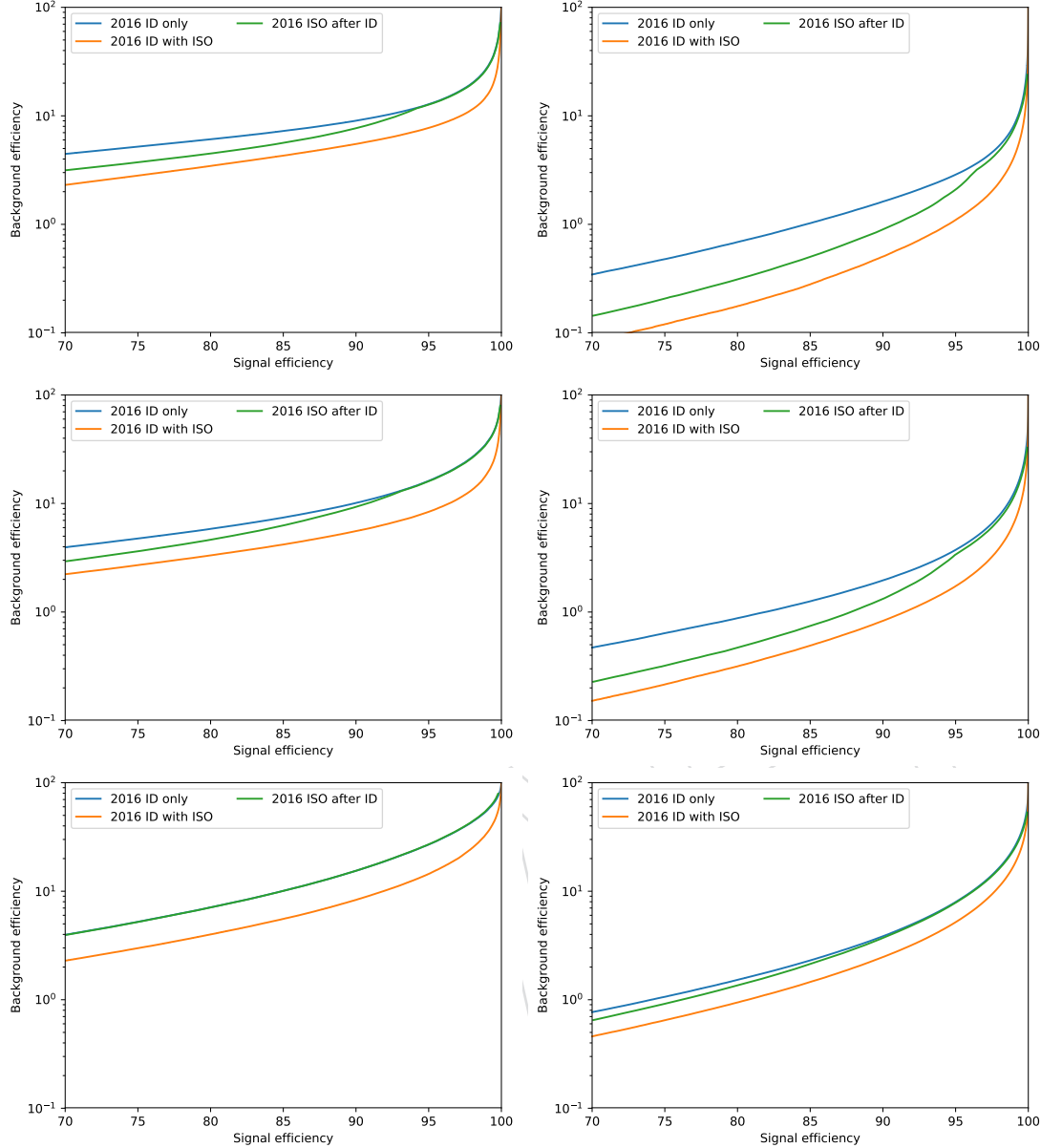


Figure 5: The receiver operating characteristic curves, representing the background efficiency vs signal efficiency, of the MVA trained on 2016 Drell-Yan with jets MC sample. Performance are shown for electrons with $5 < p_T < 10$ GeV (left), $p_T > 10$ GeV (right), and $|\eta| < 0.8$ (top), $0.8 < |\eta| < 1.479$ (middle), and $|\eta| > 1.479$ (bottom).

Tables 11, 12 and 13 list the cuts values applied to the MVA output for 2016, 2017, 2018 training, respectively. For 2018, the corresponding signal and background efficiencies are given as examples. They are very similar for 2016 and 2017. For the analysis, loose electrons have to pass this MVA identification and isolation working point.

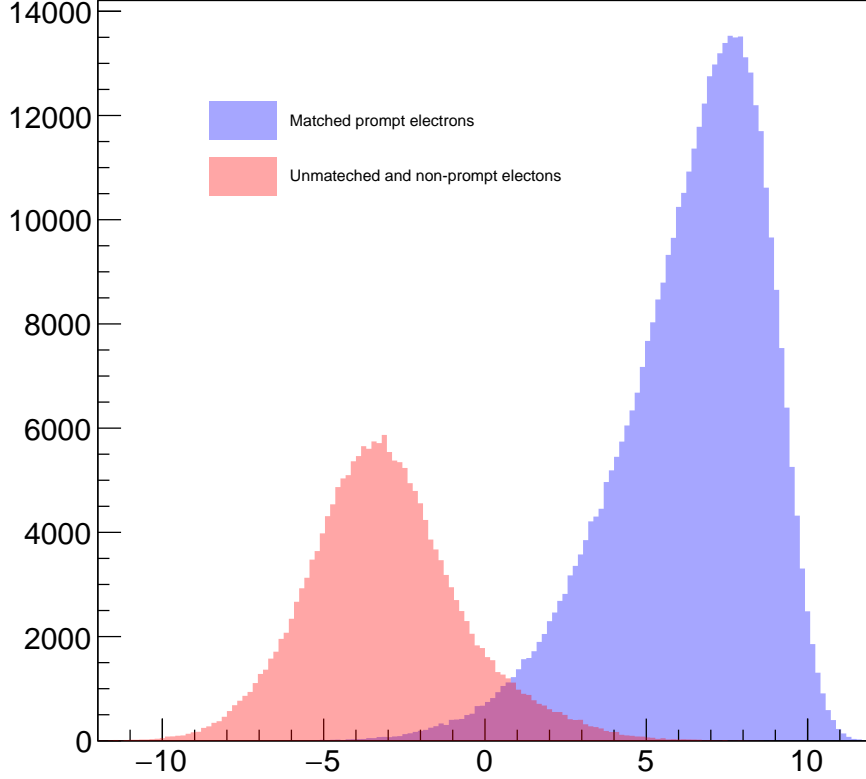


Figure 6: The Output of the multiclassifier discriminant for prompt electrons matched to truth electrons from Z decay (blue) and for misidentified electrons (red). Events are all taken from Drell-Yan with jets MC sample.

Observable type	Observable name
Cluster shape	RMS of the energy-crystal number spectrum along η and ϕ ; $\sigma_{i\eta i\eta}, \sigma_{i\phi i\phi}$
	Super cluster width along η and ϕ
	Ratio of the hadronic energy behind the electron supercluster to the supercluster energy, H/E
	Circularity $(E_{5\times 5} - E_{5\times 1})/E_{5\times 5}$
Track-cluster matching	Sum of the seed and adjacent crystal over the super cluster energy R_9
	For endcap traing bins: energy fraction in pre-shower $E_{\text{PS}}/E_{\text{raw}}$
	Energy-momentum agreement $E_{\text{tot}}/p_{in}, E_{\text{ele}}/p_{out}, 1/E_{\text{tot}} - 1/p_{in}$
tracking	Position matching $\Delta\eta_{in}, \Delta\varphi_{in}, \Delta\eta_{seed}$
	Fractional momentum loss $f_{\text{brem}} = 1 - p_{out}/p_{in}$
	Number of hits of the KF and GSF track N_{KF}, N_{GSF}
	Reduced χ^2 of the KF and GSF track $\chi^2_{KF}, \chi^2_{GSF}$
	Number of expected but missing inner hits
isolation	Probability transform of conversion vertex fit χ^2
	Particle Flow photon isolation sum
	Particle Flow charged hadrons isolation sum
For PU-resilience	Particle Flow neutral hadrons isolation sum
	Mean energy density in the event: ρ

Table 10: Overview of input features to the identification classifier.

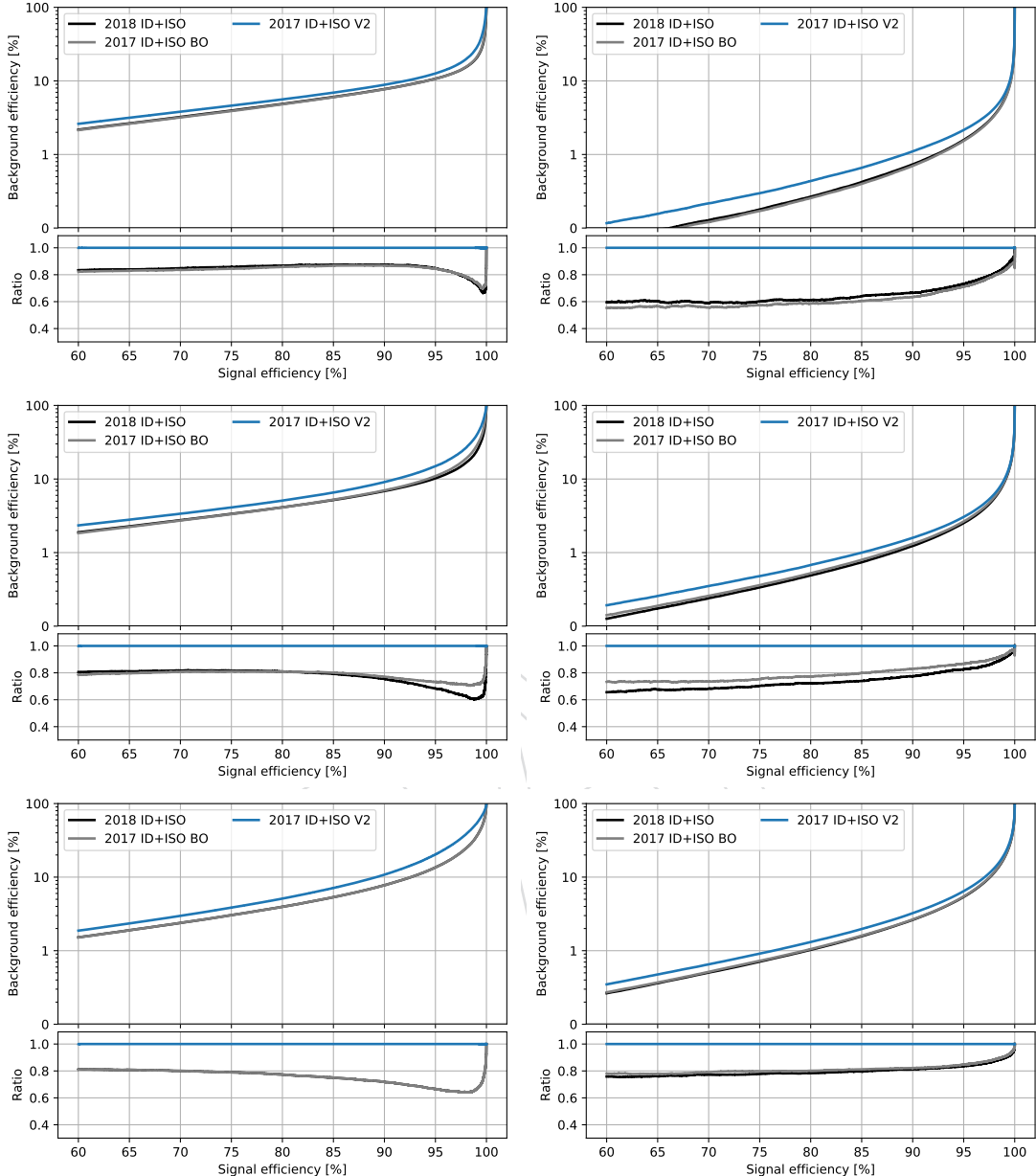


Figure 7: The receiver operating characteristic curves, representing the background efficiency vs signal efficiency, of the MVA trained on the 2017 Drell-Yan with jets MC sample and applied on the 2018 Drell-Yan with jets MC sample. The training combines identification and isolation features. Performance are shown for electrons with $5 < p_T < 10 \text{ GeV}$ (left), $p_T > 10 \text{ GeV}$ (right), and $|\eta| < 0.8$ (top), $0.8 < |\eta| < 1.479$ (middle), and $|\eta| > 1.479$ (bottom). V1 and V2 versions of training are compared, exploiting TMVA and xgboost training libraries respectively.

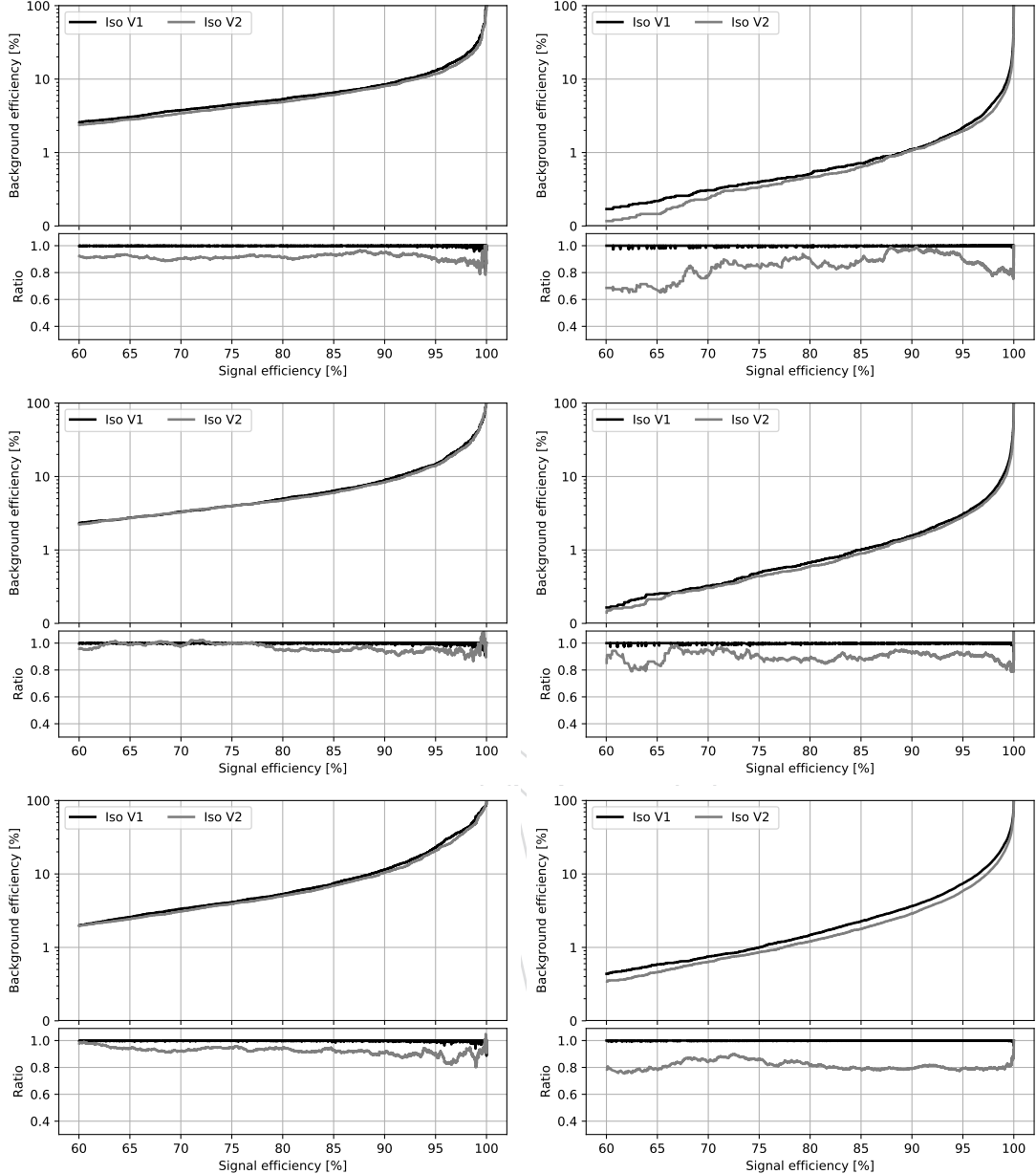


Figure 8: Performance comparison, background efficiency vs signal efficiency, of the MVA trained using TMVA framework (V1) and XGBoost framework (V2). The performance are shown for electrons with $5 < p_T < 10$ GeV (left), $p_T > 10$ GeV (right), and $|\eta| < 0.8$ (top), $0.8 < |\eta| < 1.479$ (middle), and $|\eta| > 1.479$ (bottom).

2016 Datasets			
minimum BDT score	$ \eta < 0.8$	$0.8 < \eta < 1.479$	$ \eta > 1.479$
$5 < p_T < 10$ GeV	0.9503	0.9461	0.9387
$p_T > 10$ GeV	0.3782	0.3587	-0.5745

Table 11: Minimum BDT score required for passing the electron identification, for 2016 samples.

2017 Datasets				
minimum BDT score	$ \eta < 0.8$	$0.8 < \eta < 1.479$	$ \eta > 1.479$	
$5 < p_T < 10 \text{ GeV}$	0.8521	0.8268	0.8694	
$p_T > 10 \text{ GeV}$	0.9825	0.9692	0.7935	

Table 12: Minimum BDT score required for passing the electron identification, for 2017 samples.

$ \eta < 0.8$			
	Cut on BDT score	Signal eff.	Background eff.
$5 < p_T < 10 \text{ GeV}$	0.8956	81.04%	4.4%
$p_T > 10 \text{ GeV}$	0.0424	97.1%	2.9%
$0.8 < \eta < 1.479$			
	Cut on BDT score	Signal eff.	Background eff.
$5 < p_T < 10 \text{ GeV}$	0.9111	79.3%	4.6%
$p_T > 10 \text{ GeV}$	0.0047	96.3%	3.6%
$ \eta > 1.479$			
	Cut on BDT score	Signal eff.	Background eff.
$5 < p_T < 10 \text{ GeV}$	0.9401	72.97%	3.6%
$p_T > 10 \text{ GeV}$	-0.6042	95.7%	6.7%

Table 13: Minimum MVA score required for passing the electron identification, together with the corresponding signal and background efficiencies, for 2018 samples.

234 4.1.3 Electron Impact Parameter Selection

235 In order to ensure that the leptons are consistent with a common primary vertex we require
236 that they have an associated track with a small impact parameter with respect to the event
237 primary vertex. We use the significance of the impact parameter to the event vertex, $SIP_{3D} =$
238 $\frac{IP}{\sigma_{IP}}$, where IP is the lepton impact parameter in three dimensions at the point of closest approach
239 with respect to the primary interaction vertex, and σ_{IP} the associated uncertainty. Hereafter, a
240 "primary lepton" is a lepton satisfying $|SIP_{3D}| < 4$.

241 4.1.4 Electron Energy Calibrations

242 Electrons in data are corrected for features in ECAL energy scale in bins of p_T and $|\eta|$. Corrections
243 are calculated on a $Z \rightarrow ee$ sample to align the dielectron mass spectrum in the data to
244 that in the MC, and to minimize its width.

245 The $Z \rightarrow ee$ mass resolution in Monte Carlo is made to match data by applying a pseudorandom
246 Gaussian smearing to electron energies, with Gaussian parameters varying in bins of p_T
247 and $|\eta|$. This has the effect of convoluting the electron energy spectrum with a Gaussian.

248 The electron energy scale is measured in data by fitting a Crystall-ball function to the di-
249 electron mass spectrum around the Z peak in the $Z \rightarrow ee$ control region. The energy scale
250 for the 2016, 2017 and 2018 dataset are shown in Fig. 9, 10, 11 (a), respectively, and decently
251 agrees with the MC with the preliminary corrections released so far by EGAMMA POG.

DRAFT

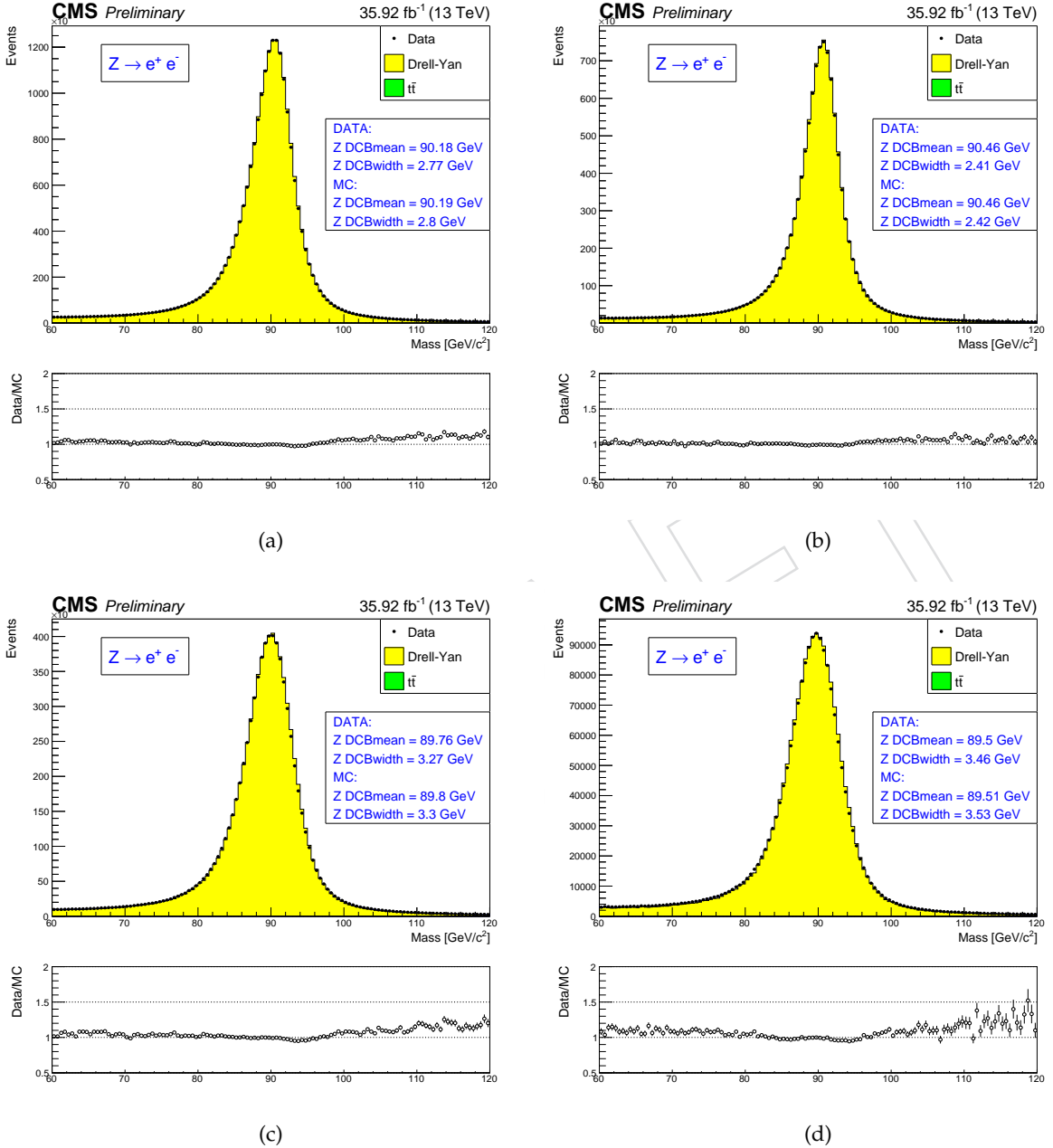


Figure 9: (a): electron energy scale measured in the $Z \rightarrow ee$ control region for all electrons, for both electrons in the barrel (b), for one electron in the barrel, one in the endcaps (c) and for both electrons in the endcaps (d), for 2016 data. The results of the Crystall-ball fit are reported in the figures.

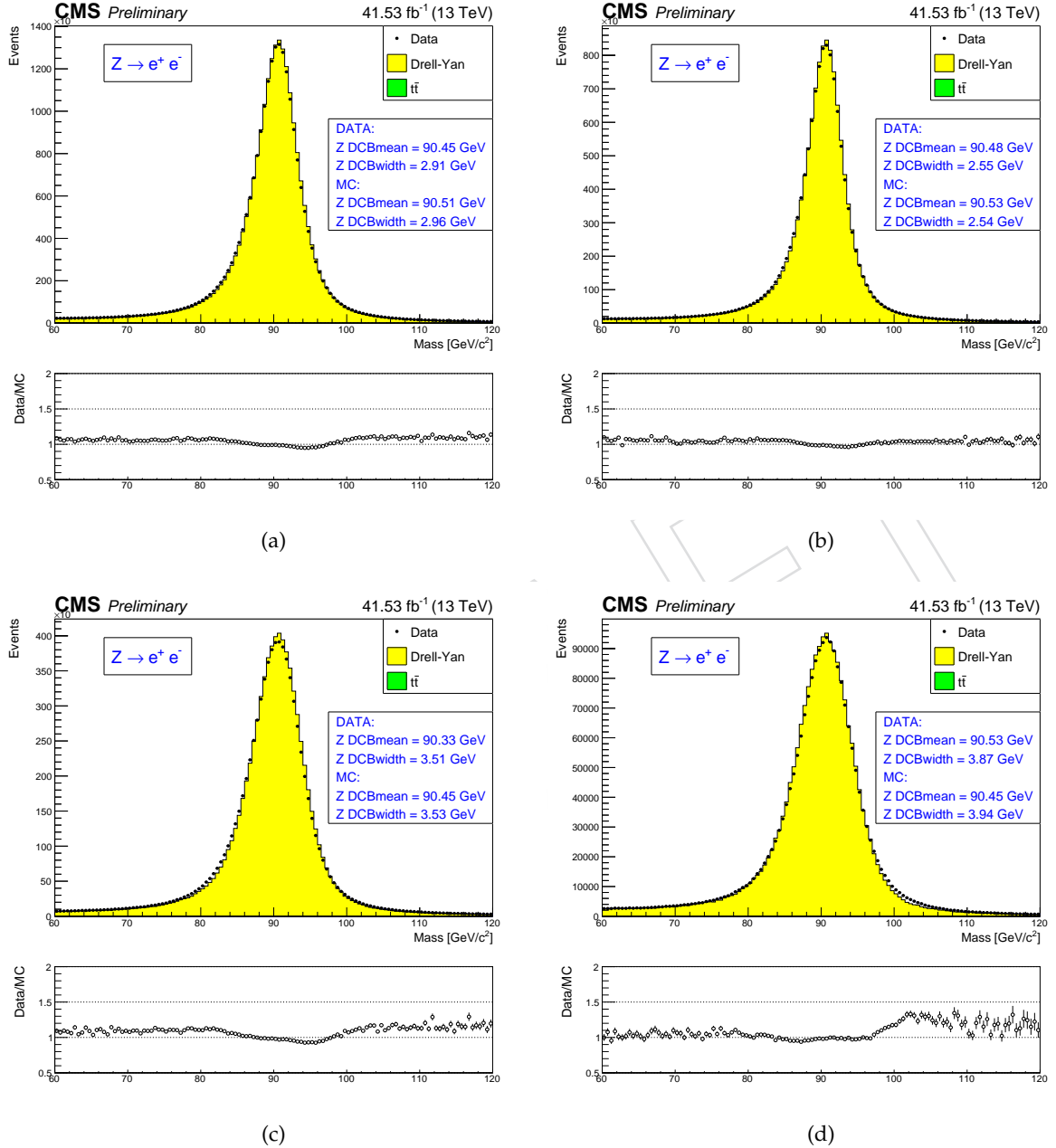


Figure 10: (a): electron energy scale measured in the $Z \rightarrow ee$ control region for all electrons, for both electrons in the barrel (b), for one electron in the barrel, one in the endcaps (c) and for both electrons in the endcaps (d), for 2017 data. The results of the Crystall-ball fit are reported in the figures.

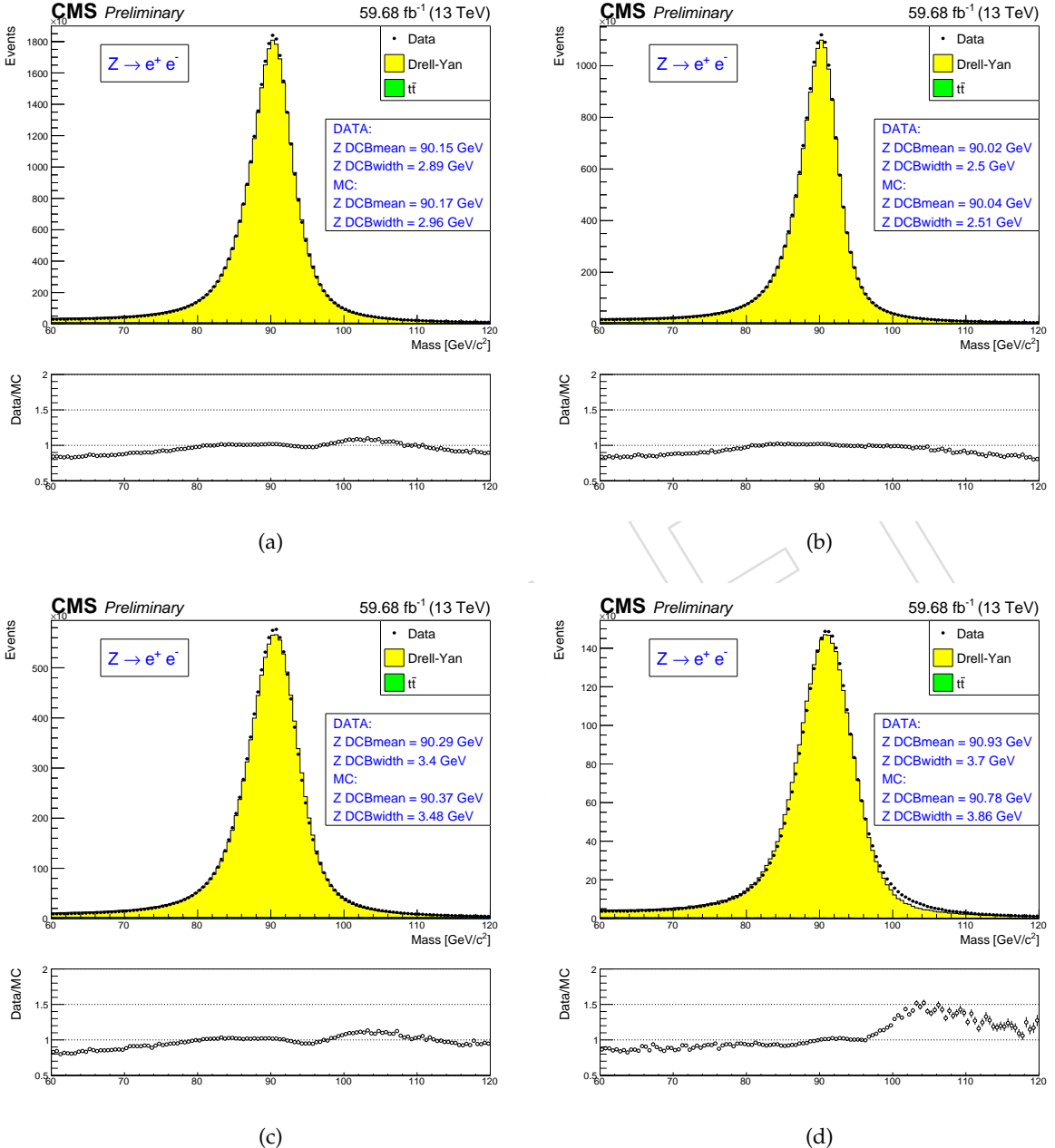


Figure 11: (a): electron energy scale measured in the $Z \rightarrow ee$ control region for all electrons, for both electrons in the barrel (b), for one electron in the barrel, one in the endcaps (c) and for both electrons in the endcaps (d), for 2018 data. The results of the Crystall-ball fit are reported in the figures.

252 **4.1.5 Electron Efficiency Measurements**

253 The Tag-and-Probe study was performed on the EGM dataset using the golden JSON of 58.83
 254 fb^{-1} . More details on the Tag-and-Probe method can be found in Ref. [37].

255 Tag electrons need to satisfy the following quality requirements:

- 256 • trigger matched to single electron trigger (e.g HLT_Ele32_WPTight_Gsf_L1DoubleEG_v*
 257 for 2018 for instance)
- 258 • $p_T > 30 \text{ GeV}$ (tag), super cluster (SC) $\eta < 2.17$
- 259 • the tag and the probe need to have opposite charge.

260 For the bin between 7 and 20 GeV, additional criteria are required:

- 261 • the tag has to pass a cut on the MVA ID > 0.92 , $\sqrt{(2 * \text{PFMET} * p_T(\text{tag}) * (1 - \cos(\phi_{\text{MET}} - \phi_{\text{tag}})))} < 45 \text{ GeV}$.
- 263 • tag p_T increased to 50 GeV
- 264 • the charge is determined with the so-called selection method, using all three estimates of the electron charge to agree.

266 These additional requirements help cleaning the background and makes the fits more reliable
 267 (and thus, the measurement more precise).

268 Probe electrons only need to be reconstructed as GsfElectron while the FSR recovery algorithm
 269 is not applied in efficiency measurement.

270 The nominal MC efficiencies are evaluated from the LO MadGraph Drell-Yan, while the NLO
 271 systematics use the MadGraph_AMCatNLO sample (or POWHEG in 2018).

272 For the efficiency measurements a template fit is used. The m_{ee} signal shape of the passing and
 273 failing probes is taken from MC and convoluted with a Gaussian. The data is then fitted with
 274 the convoluted MC template and a CMSShape (an Error-function with a one-sided exponential
 275 tail). This change follows from the usage of the T&P tool developed by the EGM POG. For the
 276 low p_T bins, a gaussian is added to the signal model for the failing probes.

277 The electron selection efficiency is measured as a function of the probe electron p_T and its SC
 278 η , and separately for electrons falling in the ECAL gaps. Figure 12, 14, 16 and 13,15, 17 show
 279 the p_T and η turn-on curves measured in data, for 2016, 2017 and 2018.

280 The EGM recommendations on the evaluation of Tag-and-Probe uncertainties for efficiency
 281 measurements are followed. Specifically, we consider

- 282 • Variation of the signal shape from a MC shape to an analytic shape (Crystal Ball)
 283 fitted to the MC
- 284 • Variation of the background shape from a CMS-shape to a simple exponential in fits
 285 to data
- 286 • Using an NLO MC sample for the signal templates

287 The total uncertainty for the measurement of the scale factors is the quadratic sum of the sta-
 288 tistical uncertainties returned from the fit and the aforementioned systematic uncertainties.

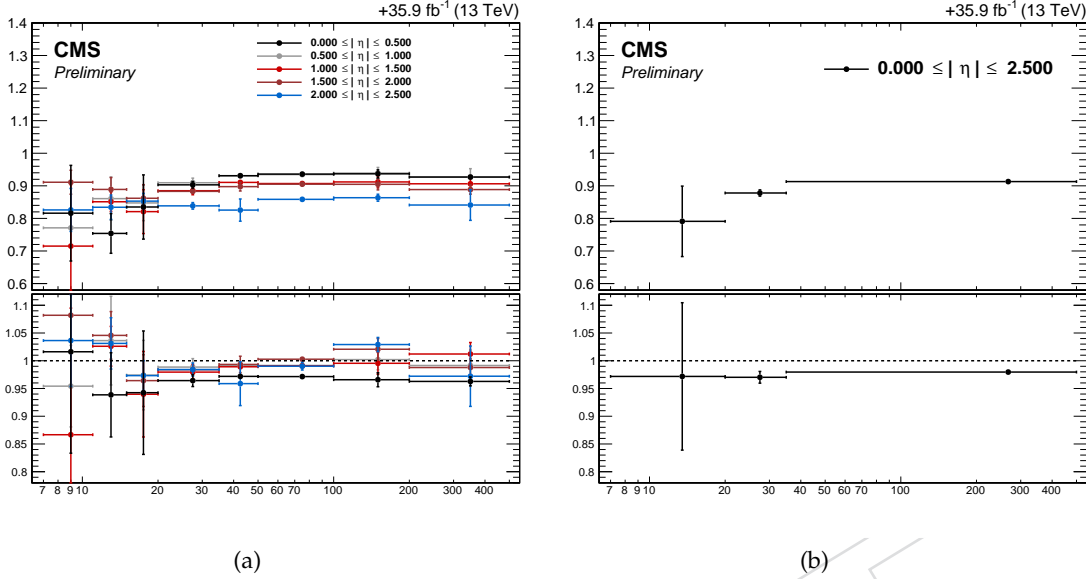


Figure 12: Electron selection efficiencies vs p_T measured using the Tag-and-Probe technique described in the text, non-gap electrons (left) and gap electrons (right), together with the corresponding data/MC ratio (bottom), for 2016 samples.

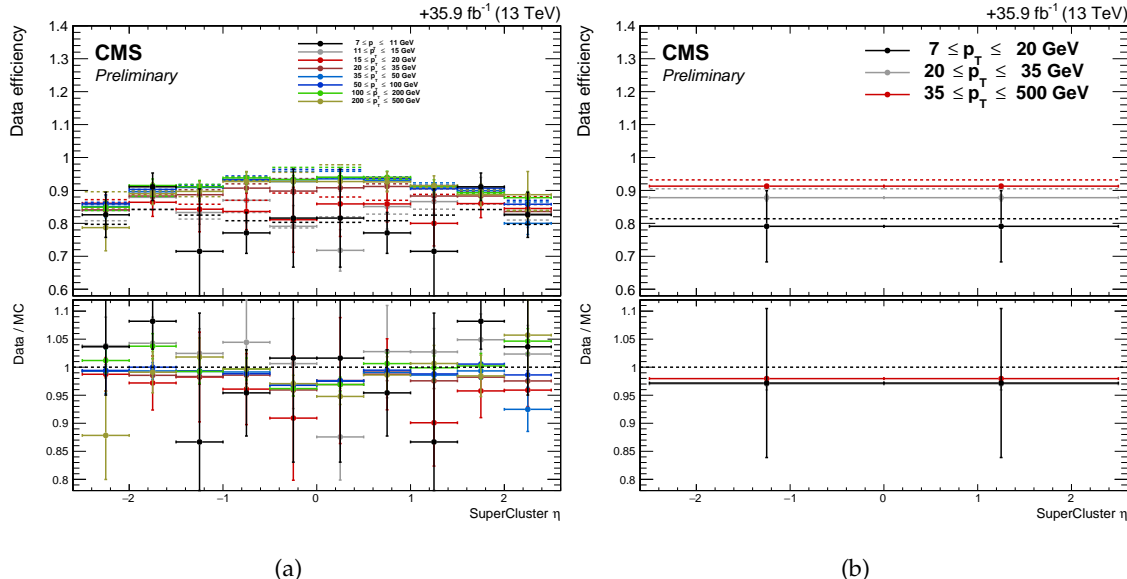


Figure 13: Electron selection efficiencies vs η measured using the Tag-and-Probe technique described in the text, non-gap electrons (left) and gap electrons (right), together with the corresponding data/MC ratio at the bottom of each plot, for 2016 samples. Dashed lines is MC, solid lines is DATA.

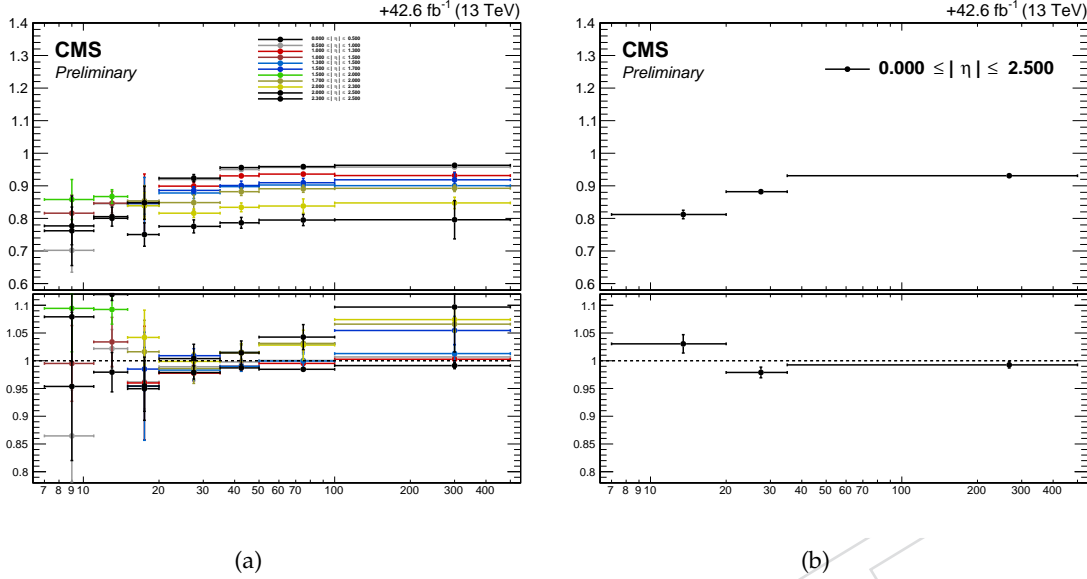


Figure 14: Electron selection efficiencies vs p_T measured using the Tag-and-Probe technique described in the text, non-gap electrons (left) and gap electrons (right), together with the corresponding data/MC ratio (bottom), for 2017 samples.

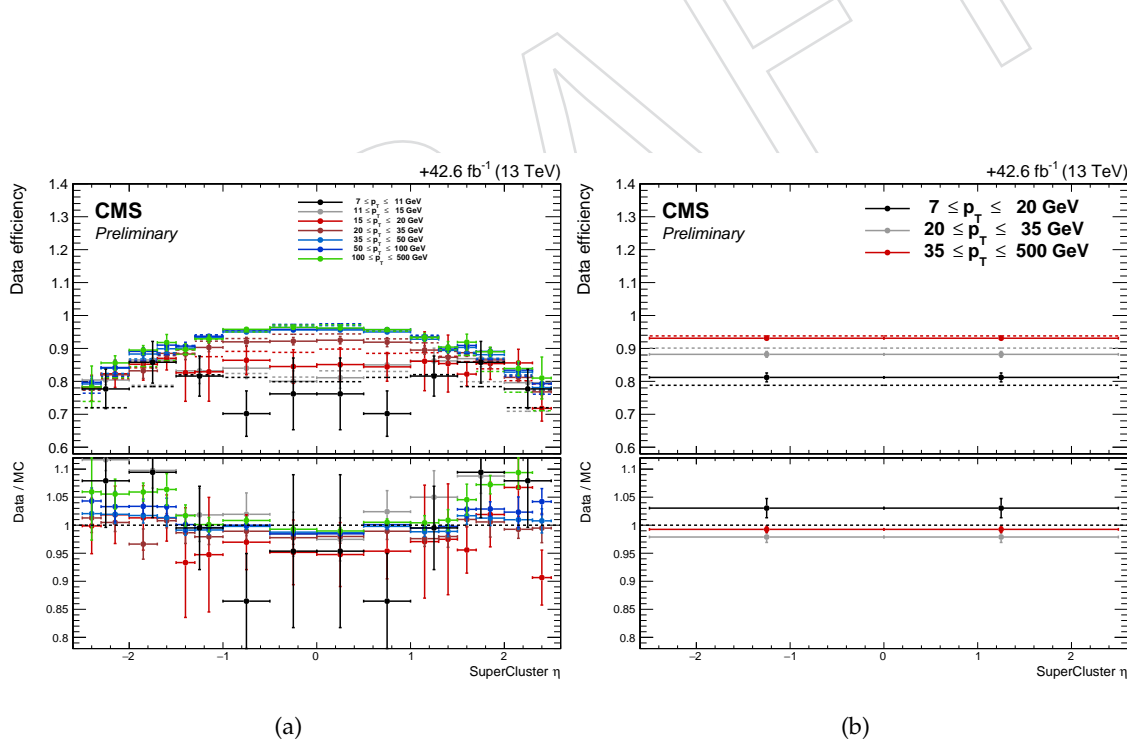


Figure 15: Electron selection efficiencies vs η measured using the Tag-and-Probe technique described in the text, non-gap electrons (left) and gap electrons (right), together with the corresponding data/MC ratio at the bottom of each plot, for 2017 samples. Dashed lines is MC, solid lines is DATA.

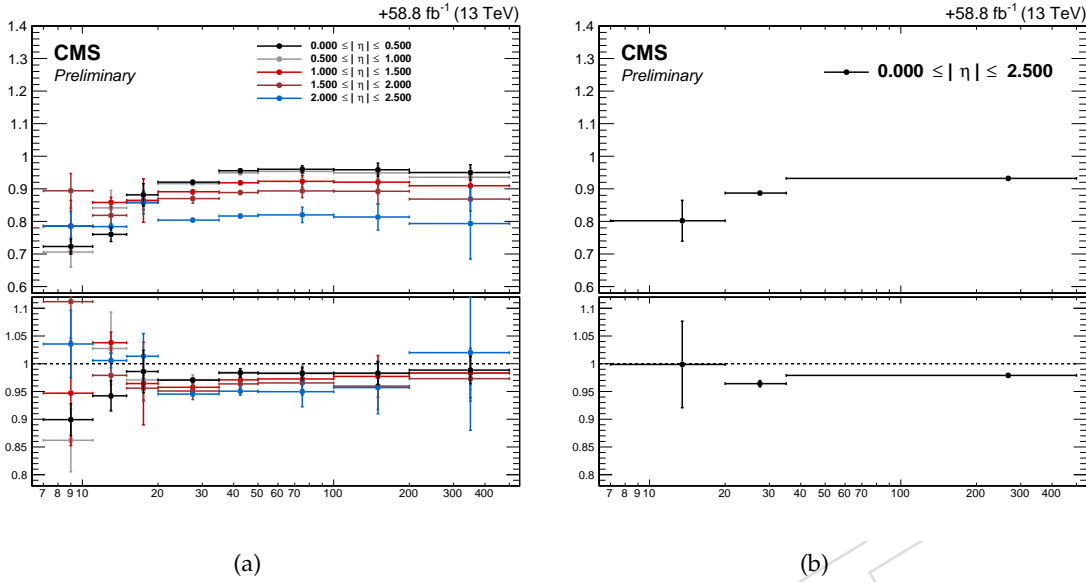


Figure 16: Electron selection efficiencies vs p_T measured using the Tag-and-Probe technique described in the text, non-gap electrons (left) and gap electrons (right), together with the corresponding data/MC ratio (bottom), for 2018 samples.

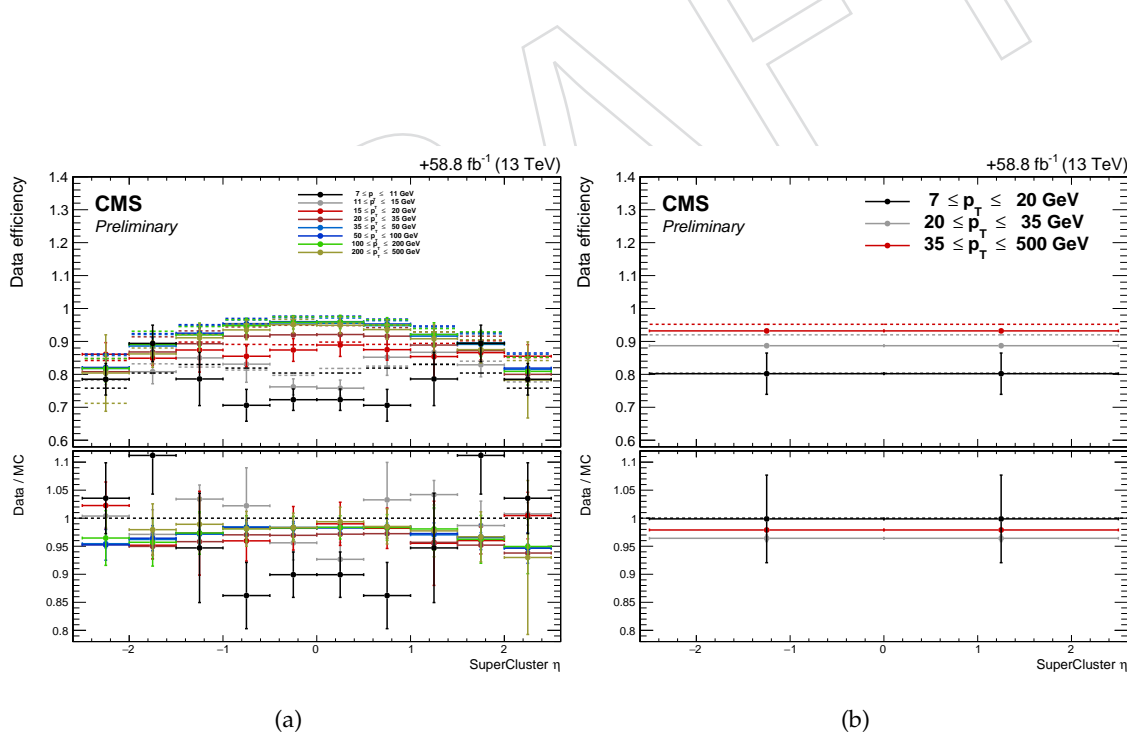


Figure 17: Electron selection efficiencies vs η measured using the Tag-and-Probe technique described in the text, non-gap electrons (left) and gap electrons (right), together with the corresponding data/MC ratio at the bottom of each plot, for 2018 samples. Dashed lines is MC, solid lines is DATA.

289 **4.2 Muons**290 **4.2.1 Muon Reconstruction**

291 More details on muon reconstruction can be found in Ref. [37]. We define **loose muons** as the
 292 muons that satisfy $p_T > 5$, $|\eta| < 2.4$, $d_{xy} < 0.5$ cm, $d_z < 1$ cm, where d_{xy} and d_z are defined
 293 w.r.t. the PV and using the ‘muonBestTrack’. Muons have to be reconstructed by either the
 294 Global Muon or Tracker Muon algorithm. Standalone Muon tracks that are only reconstructed
 295 in the muon system are rejected. Muons with muonBestTrackType==2 (standalone) are dis-
 296 carded even if they are marked as global or tracker muons.

297 Loose muons with p_T below 200 GeV are considered identified muons if they also pass the PF
 298 muon ID (note that the naming convention used for these IDs differs from the muon POG
 299 naming scheme, in which the “tight ID” used here is called the “loose ID”). Loose muons with
 300 p_T above 200 GeV are considered identified muons if they pass the PF ID or the Tracker High-
 301 p_T ID, the definition of which is shown in Table 14. This relaxed definition is used to increase
 302 signal efficiency for the high-mass search. When a very heavy resonance decays to two Z
 303 bosons, both bosons will be very boosted. In the lab frame, the leptons coming from the decay
 304 of a highly boosted Z will be nearly collinear, and the PF ID loses efficiency for muons separated
 305 by approximately $\Delta R < 0.4$, which roughly corresponds to muons originating from Z bosons
 306 with $p_T > 500$ GeV.

Table 14: The requirements for a muon to pass the Tracker High- p_T ID. Note that these are equivalent to the Muon POG High- p_T ID with the global track requirements removed.

Plain-text description	Technical description
Muon station matching	Muon is matched to segments in at least two muon stations NB: this implies the muon is an arbitrated tracker muon.
Good p_T measurement	$\frac{p_T}{\sigma_{p_T}} < 0.3$
Vertex compatibility ($x - y$)	$d_{xy} < 2$ mm
Vertex compatibility (z)	$d_z < 5$ mm
Pixel hits	At least one pixel hit
Tracker hits	Hits in at least six tracker layers

307 An additional “ghost-cleaning” step is performed to deal with situations when a single muon
 308 can be incorrectly reconstructed as two or more muons:

- 309 • Tracker Muons that are not Global Muons are required to be arbitrated.
- 310 • If two muons are sharing 50% or more of their segments then the muon with lower
 311 quality is removed.

312 **4.2.2 Muon Isolation**

Particle-Flow based isolation is used for the muons. The so-called $\Delta\beta$ correction is applied in order to subtract the pileup contribution for the muons, whereby $\Delta\beta = \frac{1}{2} \sum_{\text{PU}}^{\text{charged had.}} p_T$ gives an estimate of the energy deposit of neutral particles (hadrons and photons) from pile-up vertices. The relative isolation for muons is then defined as:

$$\text{RelPFiso} = \frac{\sum_{\text{lepton}}^{\text{charged had.}} p_T + \max(\sum_{\text{neutral had.}}^{} E_T + \sum_{\text{photon}}^{} E_T - \Delta\beta, 0)}{p_T} \quad (2)$$

313 The isolation working point for muons was optimized in Ref. [37] and the working point was
314 chosen to be the same as electrons, namely $\text{RelPFiso}(\Delta R = 0.3) < 0.35$.

315 **4.2.3 Muon Impact Parameter Selection**

316 In addition to a cut to the Muon BDT, we apply an additional cut to the muon significance of
317 impact parameter as for the electrons, as described in Sec. 4.1.3:

318 • $|\text{SIP}_{3D} - \frac{\text{IP}}{\sigma_{\text{IP}}} | < 4$

319 **4.2.4 Muon Energy Calibrations**

320 Similar to electrons the muon momentum scale is measured in data by fitting a Crystall-ball
321 function to the di-muon mass spectrum around the Z peak in the $Z \rightarrow \mu\mu$ control region.
322 Fig. 18, 19 and 20 shows a very good agreement between data and simulation, for 2016, 2017
323 and 2018 eras, respectively.

DRAFT

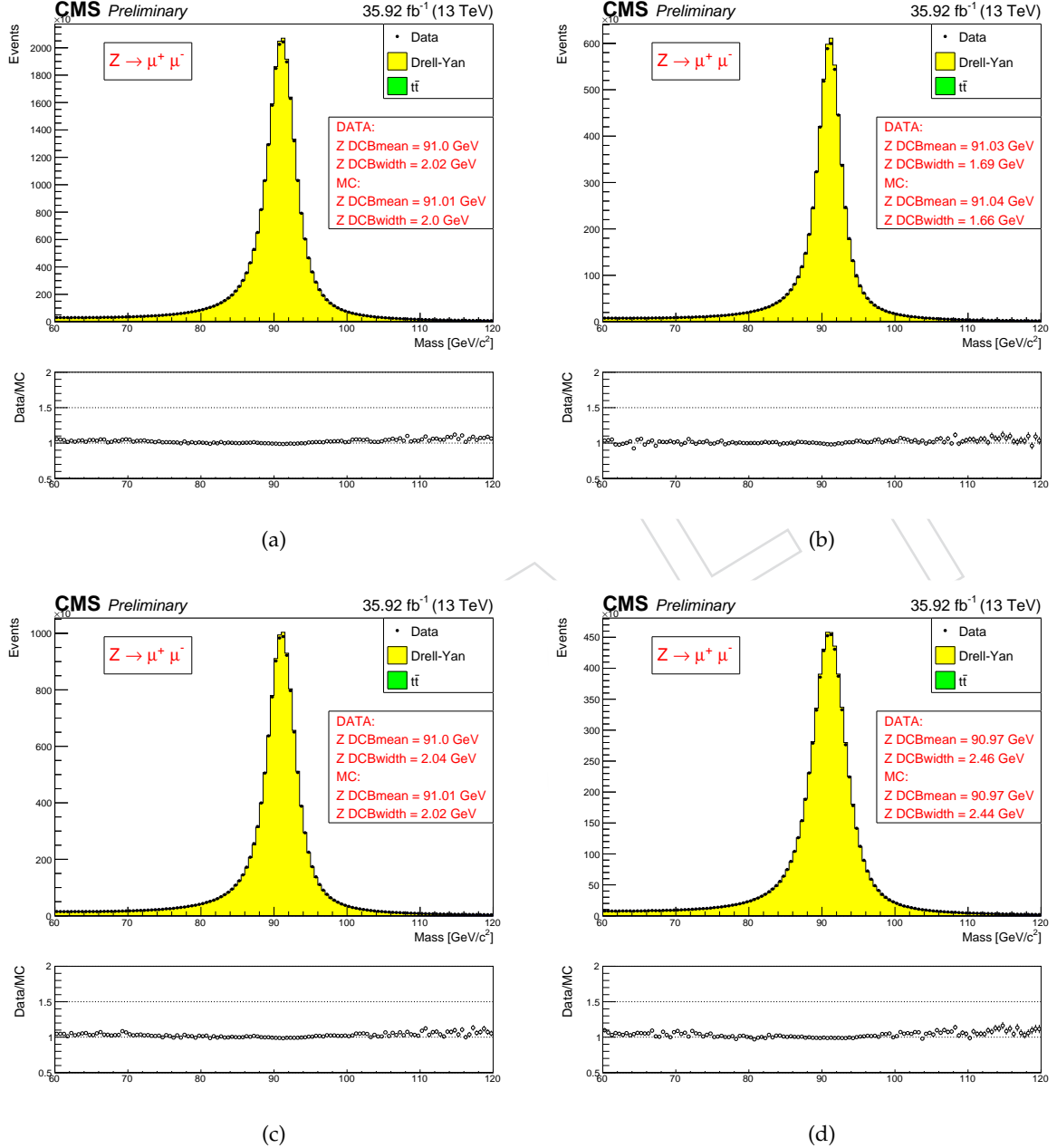


Figure 18: (a): muon energy scale measured in the $Z \rightarrow \mu\mu$ control region for all muons, for both muons in the barrel (b), for one muon in the barrel, one in the endcaps (c) and for both muons in the endcaps (d), for 2016. The results of the Crystall-ball fit are reported in the figures.

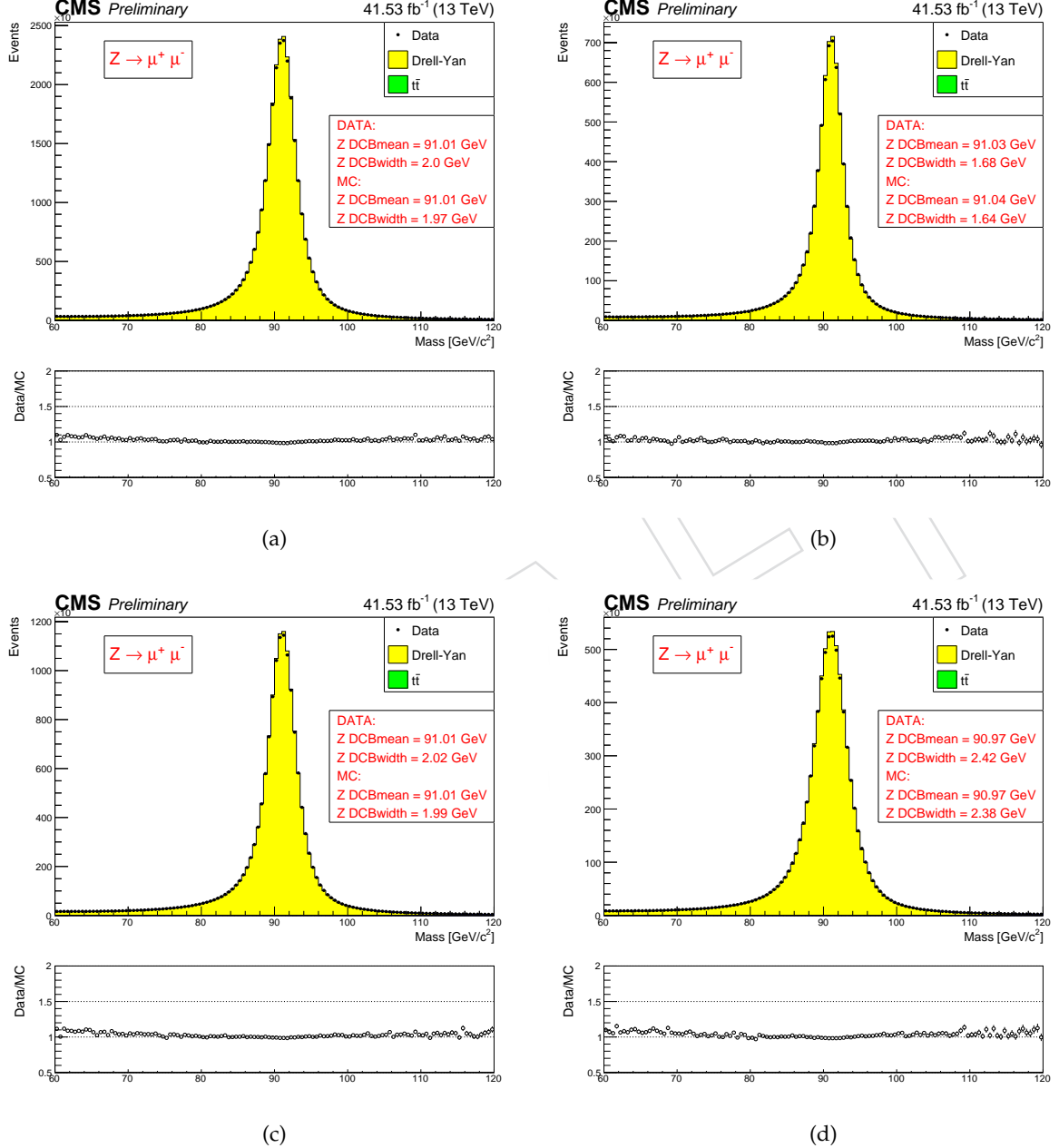


Figure 19: (a): muon energy scale measured in the $Z \rightarrow \mu\mu$ control region for all muons, for both muons in the barrel (b), for one muon in the barrel, one in the endcaps (c) and for both muons in the endcaps (d), for 2017. The results of the Crystall-ball fit are reported in the figures.

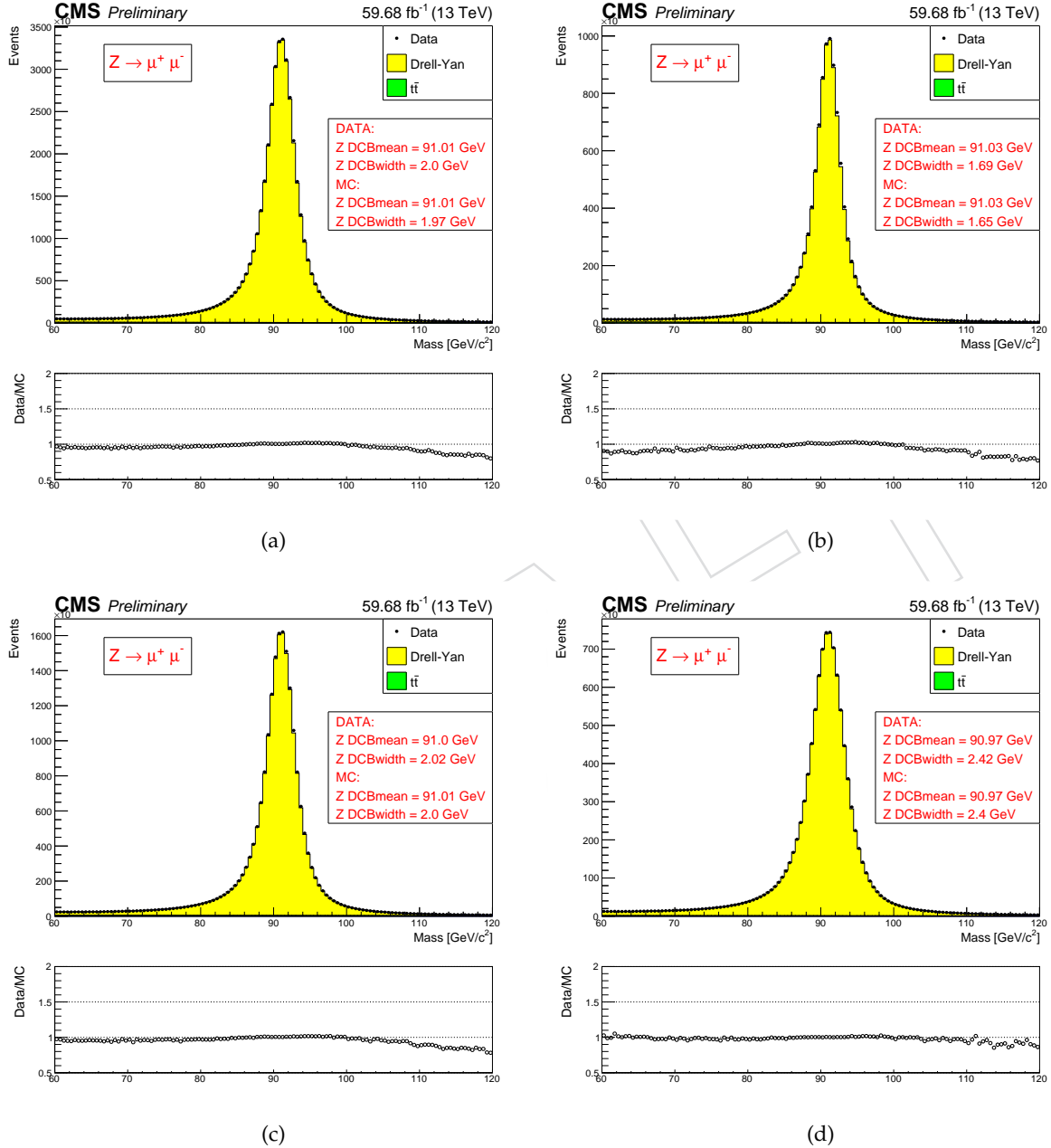


Figure 20: (a): muon energy scale measured in the $Z \rightarrow \mu\mu$ control region for all muons, for both muons in the barrel (b), for one muon in the barrel, one in the endcaps (c) and for both muons in the endcaps (d), for 2018. The results of the Crystall-ball fit are reported in the figures.

324 **4.2.5 Muon Efficiency Measurements**

325 Muon efficiencies are measured with the Tag and Probe (T&P) method performed on $Z \rightarrow \mu\mu$
 326 and $J/\psi \rightarrow \mu\mu$ events in bins of p_T and η . More details on the methodology can be found in
 327 Ref. [38]. Measurements are extracted using 2018 RunA,B,C,D data while the measurements
 328 corresponding to 2016 and 2017 datasets have already been reported in Ref. [39] and Ref. [40]
 329 respectively. The Z sample is used to measure the muon reconstruction and identification ef-
 330 ficiency at high p_T , and the efficiency of the isolation and impact parameter requirements at
 331 all p_T . The J/ψ sample is used to measure the reconstruction efficiency at low p_T , as it ben-
 332 efits from a better purity in that kinematic regime. In this case, events are collected using
 333 `HLT_Mu7p5_Track2_Jpsi_v*` when probing the reconstruction and identification efficiency
 334 in the muon system, and using the `HLT_Mu7p5_L2Mu2_Jpsi_v*` when probing the tracking
 335 efficiency.

336 **Reconstruction and identification** Results for the muon reconstruction and identification
 337 efficiency for $p_T > 20$ GeV have been derived by the Muon POG. The probe in this measure-
 338 ment are tracks reconstructed in the inner tracker, and the passing probes are those that are
 339 also reconstructed as a global or tracker muon and passing the Muon POG Loose muon identi-
 340 fication. Results for low p_T muons were derived using J/ψ events, with the same definitions of
 341 probe and passing probes. The systematic uncertainties are estimated by varying the analytical
 342 signal and background shape models used to fit the dimuon invariant mass. Details on the
 343 procedure can be found in Ref. [37]. The efficiency and scale factors used for low p_T muons are
 344 the ones derived using single muon prompt-reco dataset.

345 The efficiency in data and simulation is shown in Fig. 21.

346 **Impact parameter requirements** The measurement is performed using Z events. Events
 347 are selected with `HLT_IsoMu27_v*` or `HLT_Mu50_v*` triggers. For this measurement, the
 348 probe is a muon passing the POG Loose identification criteria, and it is considered a passing
 349 probe if satisfies the SIP3D, dxy , dz cuts of this analysis. The results are shown in Fig. 22.

350 **Isolation requirements** The isolation efficiency is measured using events from the Z decay
 351 for any p_T . The events are selected with either of `HLT_IsoMu27_v*` or `HLT_Mu50_v*` triggers.
 352 The isolation of the muons are calculated after recovery of the FSR photons and subtracting
 353 their contribution to the isolation cone of the muons. More detailed description of the method
 354 can be found in Ref. [41].

355 The results are shown in Fig. 23.

356 **Tracking** The efficiency to reconstruct a muon track in the inner detector is measured us-
 357 ing as probes tracks reconstructed in the muon system alone. The method for measuring the
 358 tracking efficiency is the same as in Ref. [42], and the results on 2018 data are briefly discussed
 359 here. The efficiency and data to mc scale factors are measured from Z events as a function of
 360 η for $p_T > 10$ GeV and $p_T < 10$ GeV. The values of data to mc scale factors used are from the
 361 ReReco version of the full dataset collected in 2018.

362 **Overall results** The product of all the data to simulation scale factors for muon tracking,
 363 reconstruction, identification, impact parameter and isolation requirements is shown in Fig. 24.

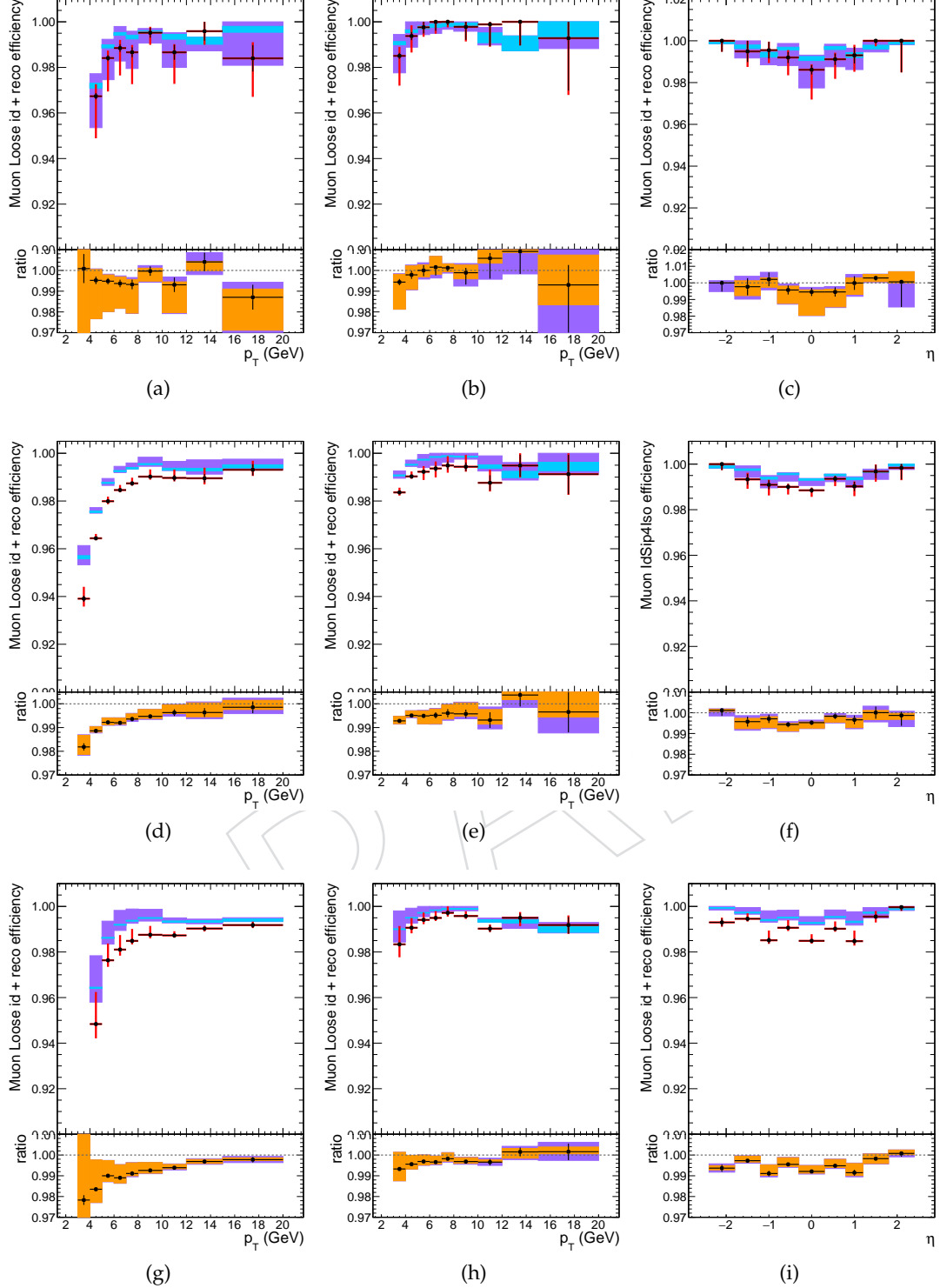


Figure 21: Muon reconstruction and identification efficiency at low p_T , measured with the tag&probe method on J/ψ events, as function of p_T in the barrel (left) and endcaps (center), and as function of η for $p_T > 7\text{ GeV}$ (right), for 2016 (top), 2017 (middle) and 2018 (bottom). In the upper panel, the larger error bars include also the systematical uncertainties, while the smaller ones are purely statistical. In the lower panel showing the ratio of the two efficiencies, the black error bars are for the statistical uncertainty, the orange rectangles for the systematical uncertainty and the violet rectangles include both uncertainties.

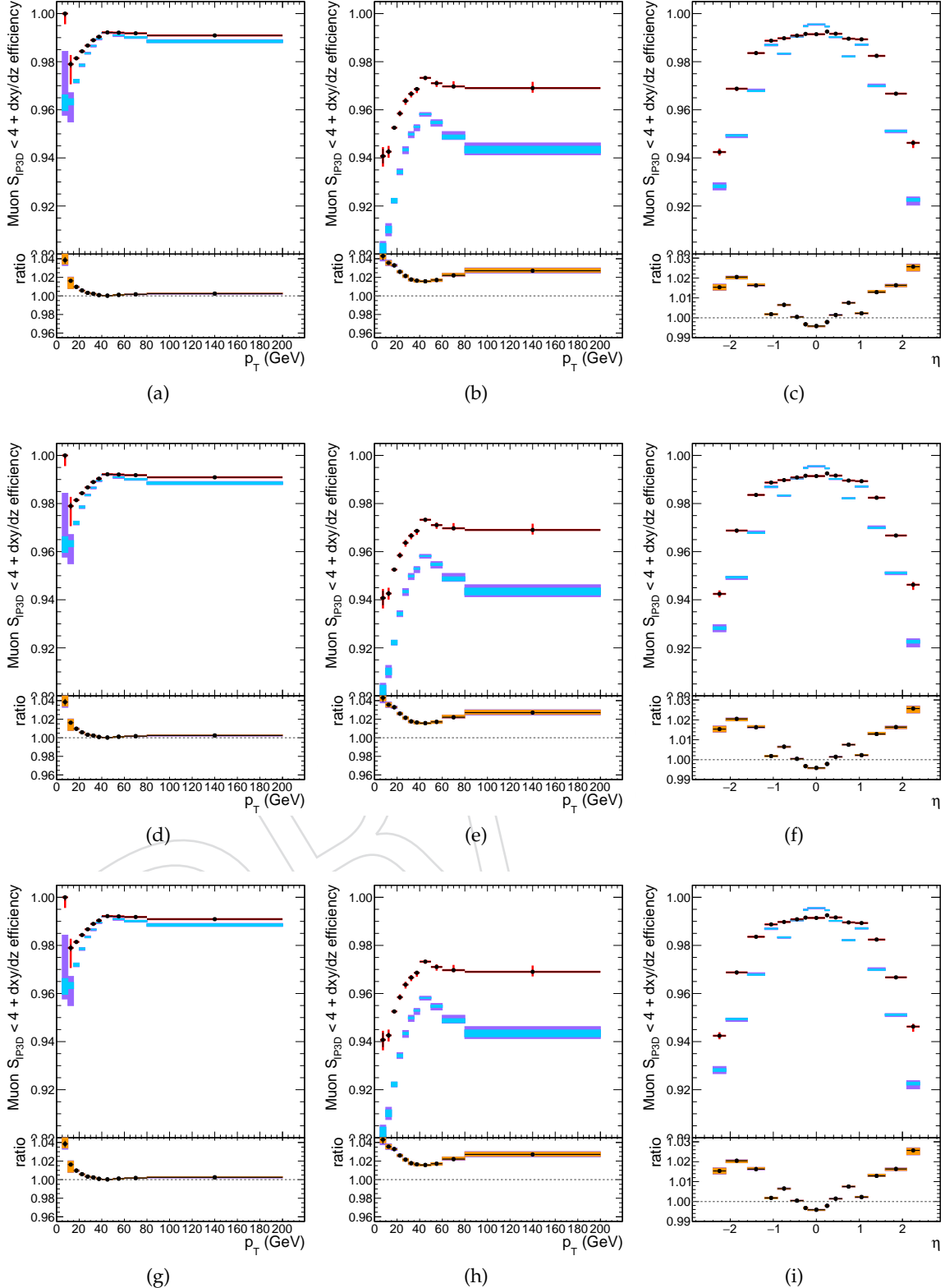


Figure 22: Efficiency of the muon impact parameter requirements, measured with the tag&probe method on Z events, as function of p_T in the barrel (left) and endcaps (center), and as function of η for $p_T > 20$ GeV (right), for 2016 (top), 2017 (middle) and 2018 (bottom). In the upper panel, the larger error bars include also the systematical uncertainties, while the smaller ones are purely statistical. In the lower panel showing the ratio of the two efficiencies, the black error bars are for the statistical uncertainty, the orange rectangles for the systematical uncertainty and the violet rectangles include both uncertainties.

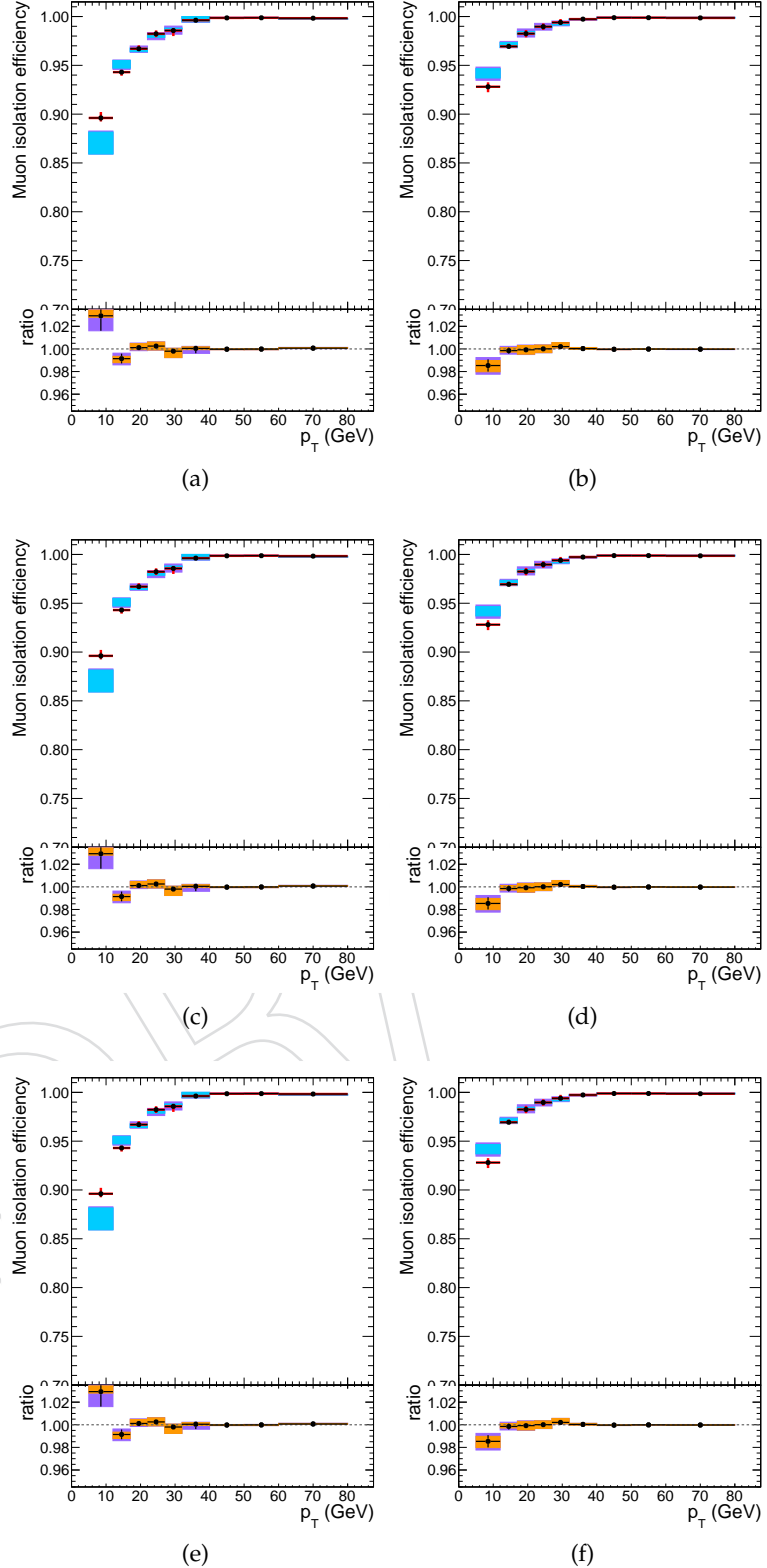


Figure 23: Efficiency of the muon isolation requirement, measured with the tag&probe method on Z events, as function of p_T in the barrel (left) and endcaps (right), for 2016 (top), 2017 (middle) and 2018 (bottom). In the upper panel, the larger error bars include also the systematical uncertainties, while the smaller ones are purely statistical. In the lower panel showing the ratio of the two efficiencies, the black error bars are for the statistical uncertainty, the orange rectangles for the systematical uncertainty and the violet rectangles include both uncertainties.

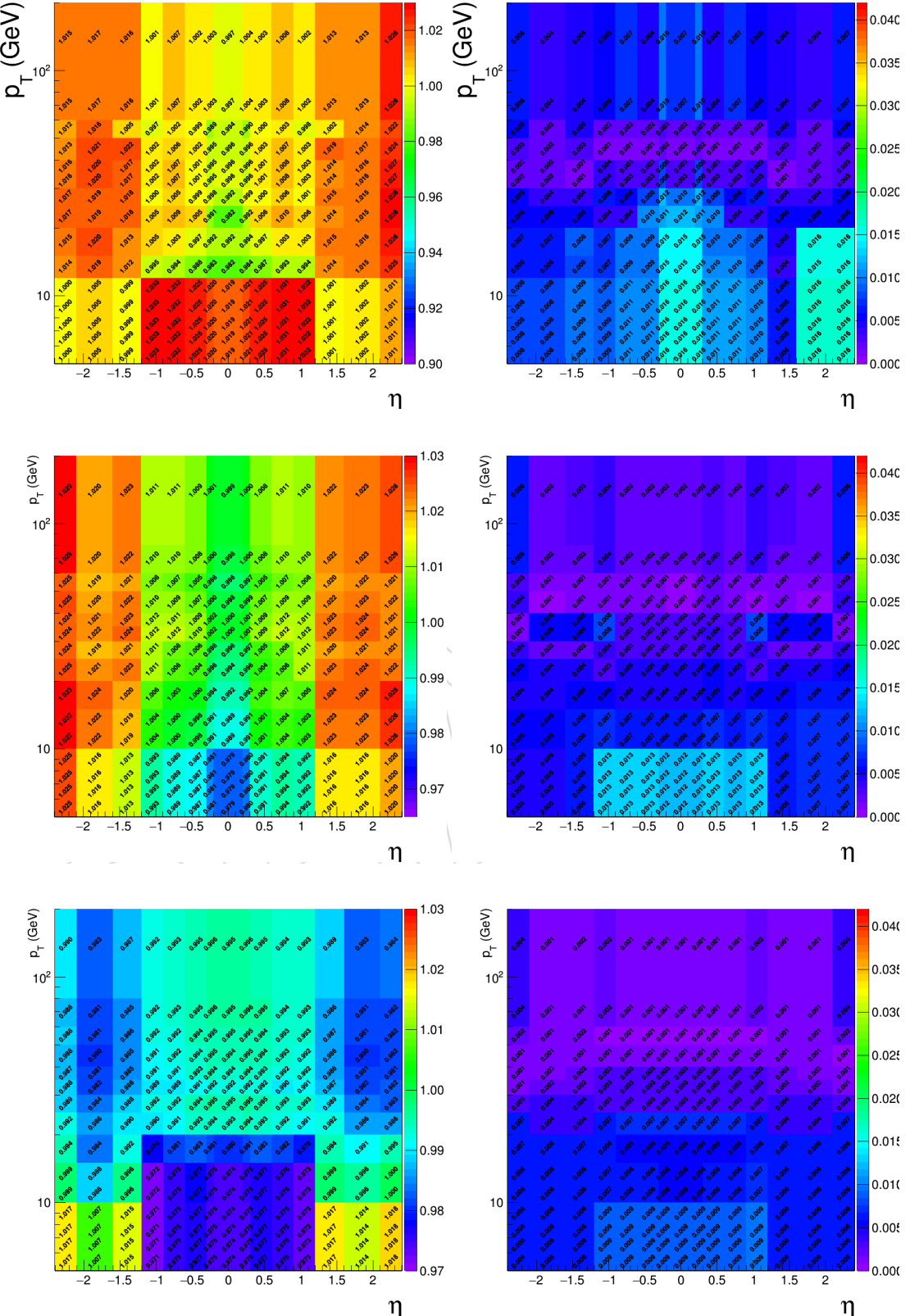


Figure 24: Left: Overall data to simulation scale factors for muons, as function of p_T and η . Right: Uncertainties on data to simulation scale factors for muons, as function of p_T and η . Results are shown for 2016 (top), 2017 (middle) and 2018 (bottom).

365 4.3 Photons for FSR recovery

366 The FSR recovery algorithm was considerably simplified with respect to what was done in Run
 367 I, while maintaining similar performance. The selection of FSR photons is now only done per-
 368 lepton and no longer depends on any Z mass criterion, thus much simplifying the subsequent
 369 ZZ candidate building and selection. As regards the association of photons with leptons, the
 370 rectangular cuts on $\Delta R(\gamma, l)$ and $E_{T,\gamma}$ have been replaced by a cut on $\Delta R(\gamma, l)/E_{T,\gamma}^2$.

371 Starting from the collection of ‘PF photons’ provided by the particle-flow algorithm, the selec-
 372 tion of photons and their association to a lepton proceeds as follows:

- 373 1. The preselection of PF photons is done by requiring $p_{T,\gamma} > 2$ GeV, $|\eta^\gamma| < 2.4$, and a
 374 relative Particle-flow isolation smaller than 1.8. The latter variable is computed using
 375 a cone of radius $R = 0.3$, a threshold of 0.2 GeV on charged hadrons with a veto cone
 376 of 0.0001, and 0.5 GeV on neutral hadrons and photons with a veto cone of 0.01, also
 377 including the contribution from pileup vertices (with the same radius and threshold as
 378 per charged isolation) .
- 379 2. Supercluster veto: we remove all PF photons that match with any electron passing both
 380 the loose ID and SIP cuts. The matching is performed by directly associating the two PF
 381 candidates.
- 382 3. Photons are associated to the closest lepton in the event among all those pass both the
 383 loose ID and SIP cuts.
- 384 4. We discard photons that do not satisfy the cuts $\Delta R(\gamma, l)/E_{T,\gamma}^2 < 0.012$, and $\Delta R(\gamma, l) < 0.5$.
- 385 5. If more than one photon is associated to the same lepton, the lowest- $\Delta R(\gamma, l)/E_{T,\gamma}^2$ is
 386 selected.
- 387 6. For each FSR photon that was selected, we exclude that photon from the isolation sum
 388 of all the leptons in the event that pass both the loose ID and SIP cuts. This concerns
 389 the photons that are in the isolation cone and outside the isolation veto of said leptons
 390 ($\Delta R < 0.4$ AND $\Delta R > 0.01$ for muons and $\Delta R < 0.4$ AND $(\eta^{\text{SC}} < 1.479 \text{ OR } \Delta R > 0.08)$
 391 for electrons).

392 More details on the optimization of the FSR photon selection can be found in Ref. [37, 41].

393 4.4 Jets

394 Vector Boson Fusion (VBF) and other production mechanisms of Higgs Boson normally differ
 395 as regards the jet kinematics. In this analysis, jets are thus used for the event categorization,
 396 which will be introduced in Section ??.

397 4.4.1 Jet Identification

398 Jets are reconstructed by using the anti- k_T clustering algorithm out of particle flow candidates,
 399 with a distance parameter $R = 0.4$, after rejecting the charged hadrons that are associated to a
 400 pileup primary vertex.

401 To reduce instrumental background, the tight working point jet ID suggested by the JetMET
 402 Physics Object Group is applied [43]. In addition, jets from Pile-Up are rejected using the
 403 PileUp jet ID criteria suggested by the JetMET POG [44]. It is to be noted that the PU JetID
 404 was only derived for 2016 conditions but is also applied to 2017 and 2018 samples.

405 In this analysis, the jets are required to be within $|\eta| < 4.7$ area and have a transverse momen-
 406 tum above 30 GeV. In addition, the jets are cleaned from any of the tight leptons (passing the
 407 SIP and isolation cut computed after FSR correction) and FSR photons by a separation criterion:
 408 $\Delta R(\text{jet}, \text{lepton}/\text{photon}) > 0.4$.

409 **4.4.2 Jet Energy Corrections**

410 The calorimeter response to particles is not linear and it is not straightforward to translate
 411 the measured jet energy to the true particle or parton energy, therefore we need Jet Energy
 412 Corrections. In this analysis, standard jet energy corrections are applied to the reconstructed
 413 jets, which consist of L1 Pileup, L2 Relative Jet Correction, L3 Absolute Jet Correction for both
 414 Monte Carlo samples and data, and also residual calibration for data [45].

415 The table 15 summarizes the various JEC and JER tags used in this analysis.

	JEC tag	JER tag
2016	Summer16_07Aug2017All_V11	Summer16_25nsV1_MC
2017	Fall17_17Nov2017_V32_94X	Fall17_V3_94X_MC
2018	Autumn18_RunABCD_V19	Autumn18_V7_MC

Table 15: Summary of all JEC and JER tags.

416 **4.4.3 Additional criteria on jets**

417 The three data taking periods analyzed in this note suffered from issues during the data taking
 418 which impact the quality of the jet reconstruction. Some of these issues would need a complete
 419 re-reconstruction of the data to be fully fixed (the so-called “Ultra Legacy ReReco”), which is
 420 beyond the scope of the paper. In the mean time, following the guidance from the JetMET POG,
 421 we studied the possibility of adding some criteria on the jet to cope with these issues.

422 **4.4.3.1 L1 pre-firing** In 2016 and 2017, the gradual timing shift of ECAL was not properly
 423 propagated to L1 trigger primitives (TP) resulting in a significant fraction of high eta TP being
 424 mistakenly associated to the previous bunch crossing. Since Level 1 rules forbid two consecu-
 425 tive bunch crossings to fire, an unpleasant consequence of this (in addition to not finding the
 426 TP in the bx 0) is that events can self veto if a significant amount of ECAL energy is found in
 427 the region of $2 < |\eta| < 3$. This effect is not described by the simulations [46]. A weight is thus
 428 calculating for each event, not to prefire, and apply to the simulation in 2016 and 2017 samples.
 429 The official tool is used for this purpose [46].

430 The Fig 25 shows the impact of the L1 pre-firing weights on the signal MC. As expected, the
 431 effect on ggH samples is minor but is at the leve of 2-3% in the endcaps for VBF production
 432 mode.

433 **4.4.3.2 removal of noisy jets** Increased jet multiplicity was reported for 2017 data, cre-
 434 ating “horns” in the jet η distribution for $2.5 < \eta_{jet} < 3$ (FIXME: add ref). The issue was linked
 435 to an increase of the ECAL noise, PU and bunch-crossing dependant, thus getting worse as
 436 luminosity increases. The problem can only be fixed in the UL ReReco. For now, we checked
 437 the impact of rejecting jets with raw $p_T < 50$ GeV in $2.65 < \eta < 3.139$. As we see no significant
 438 impact in the data/MC agreement, we decided not to use these cuts.

439 **4.4.3.3 HEM 15/16 failures** Following a CMS-wide power interlock, the power-on of
 440 CAEN A3100HBP modules that provide low-voltage power to the on-detector HE front-end
 441 electronics led to irreversible damage of two sectors on the HE minus side, HEM15 and HEM16

442 (FIXME: add ref). No significant impact was seen and nothing particular is done to cope with
 443 this.

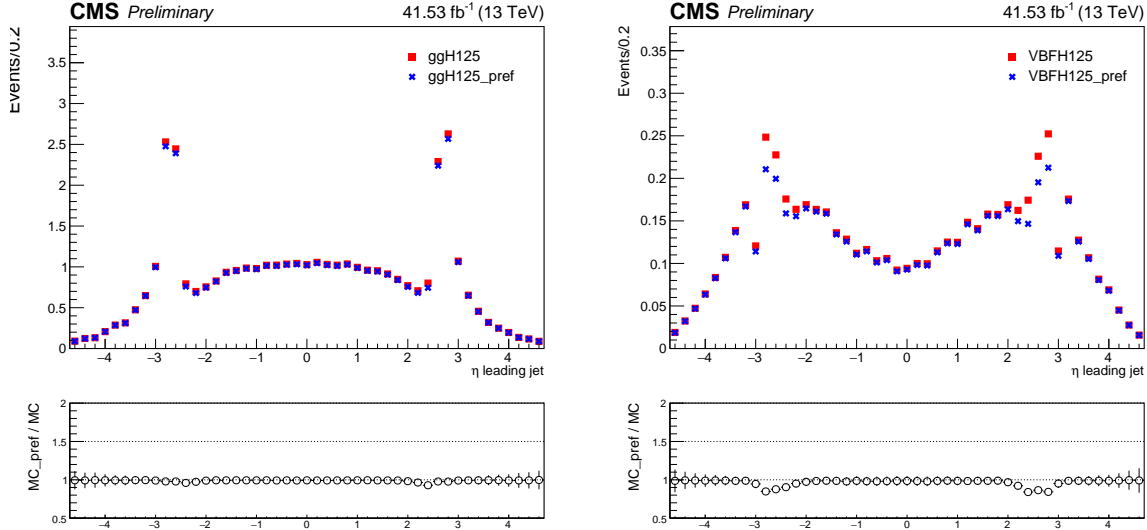


Figure 25: Comparison between 2017 MC samples with (blue) and without (red) L1 pre-firing weights for ggH (left) and VBFH signals. The ratio is shown at the bottom of each plot.

4.4.4 B-tagging

445 For categorization purpose, we need to distinguish whether a jet is b-jet or not. The *DeepCSV*
 446 algorithm is used as our b-tagging algorithm. It combines the same information as the previous
 447 tagger *CSVv2*, impact parameter significance, secondary vertex and jet kinematics but uses
 448 information of more tracks. Also, the b-tag output discriminator is computed with a Deep
 449 Neural Network. In this analysis, a jet is considered to be b-tagged if it passes the *medium*
 450 working point, i.e. if its $| \text{pfDeepCSVJetTags:prob} + \text{pfDeepCSVJetTags:prob}_{\text{bb}} |$ discriminator
 451 is greater than 0.4184 [47].

452 Data to simulation scale factors for b-tagging efficiency are provided for this working point
 453 for the full dataset as a function of jet p_T , η and flavour. They are applied to simulated jets by
 454 downgrading (upgrading) the b-tagging status of a fraction of the b-tagged (untagged) jets that
 455 have a scale factor smaller (larger) than one.

4.4.5 Missing Transverse Energy

457 MET is not used in this analysis to, for instance, categorize events.

4.4.6 Validation on data

459 Similarly to what was done with electrons and muons, we performed some validation studies
 460 to probe the agreement between data and simulated samples for jets. Events containing
 461 $Z \rightarrow e^+e^-$ or $Z \rightarrow \mu^+\mu^-$ were selected, following the same trigger and lepton selection crite-
 462 ria of the main analysis, but increasing the p_T threshold on leptons to 30 GeV and asking the
 463 invariant mass of the two leptons to be within the 70-110 GeV range.

464 Basic properties of additional jets in the event, with $p_T > 30$ GeV and $\eta < 4.7$, were then
 465 compared. Figure 26 shows the pseudo-rapidity and transverse momentum of the leading jet

466 in data and MC for the three data taking periods. Fig 27 shows the jet multiplicity. Uncertainties
 467 from the jet energy corrections are also displayed on the data/MC ratio plots.

468 The agreement between data and simulation is found to be good for the jet transverse momen-
 469 tumb or pseudo-rapidity, given the large uncertainties in the forward region.

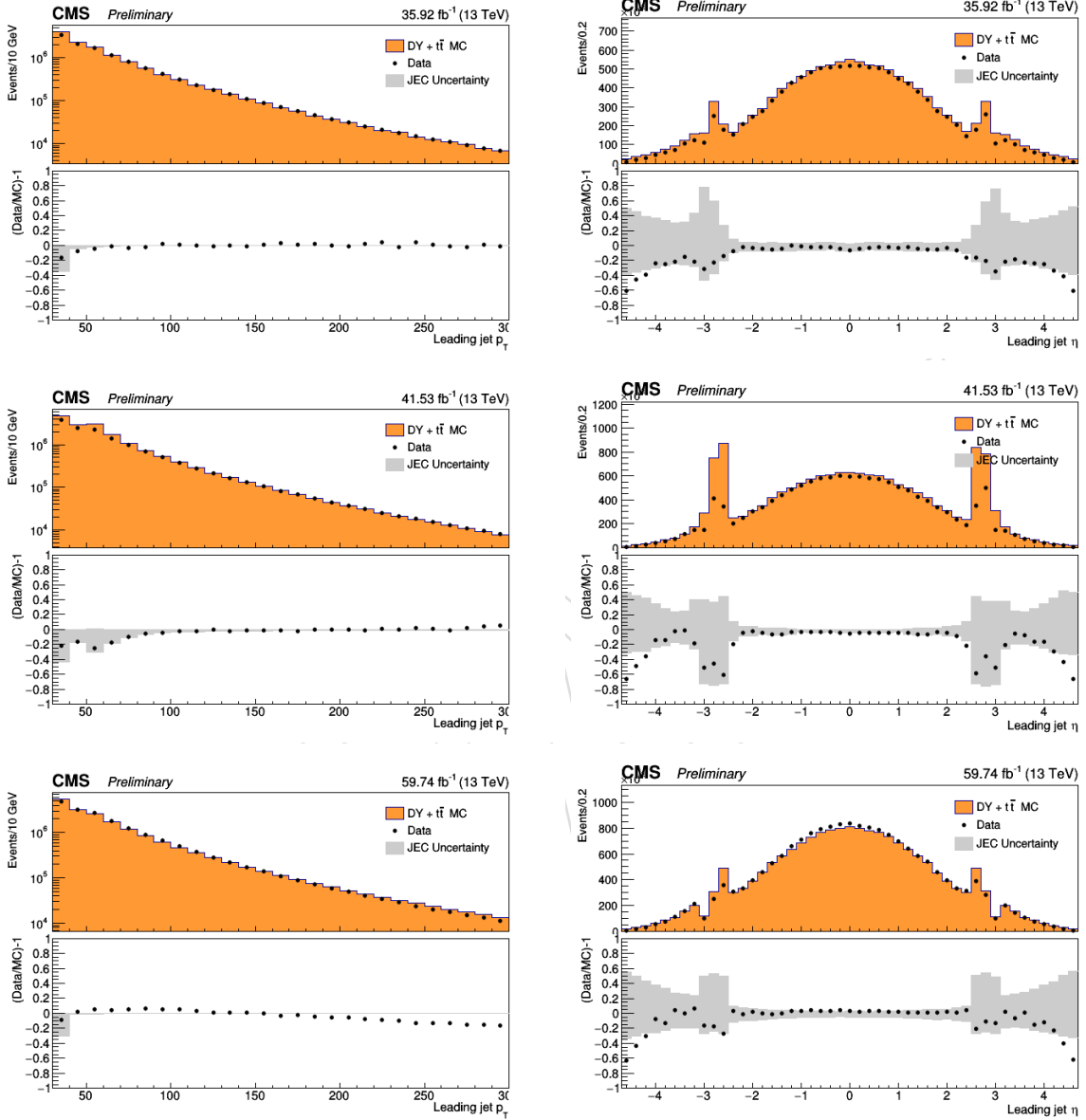


Figure 26: Comparison between data and MC for the leading jet p_T (left) and jet η (right) for 2016 (top), 2017 (middle) and 2018 (bottom). $Z \rightarrow \ell\ell + \text{jets}$ events are used. MC is normalized to data. Jet ID and Jet PUID are applied. MC samples include DY and $t\bar{t}$. Data/MC ratio plots are shown in the bottom of each plots, together with the uncertainties (shaded histograms) from Jet Energy Corrections.

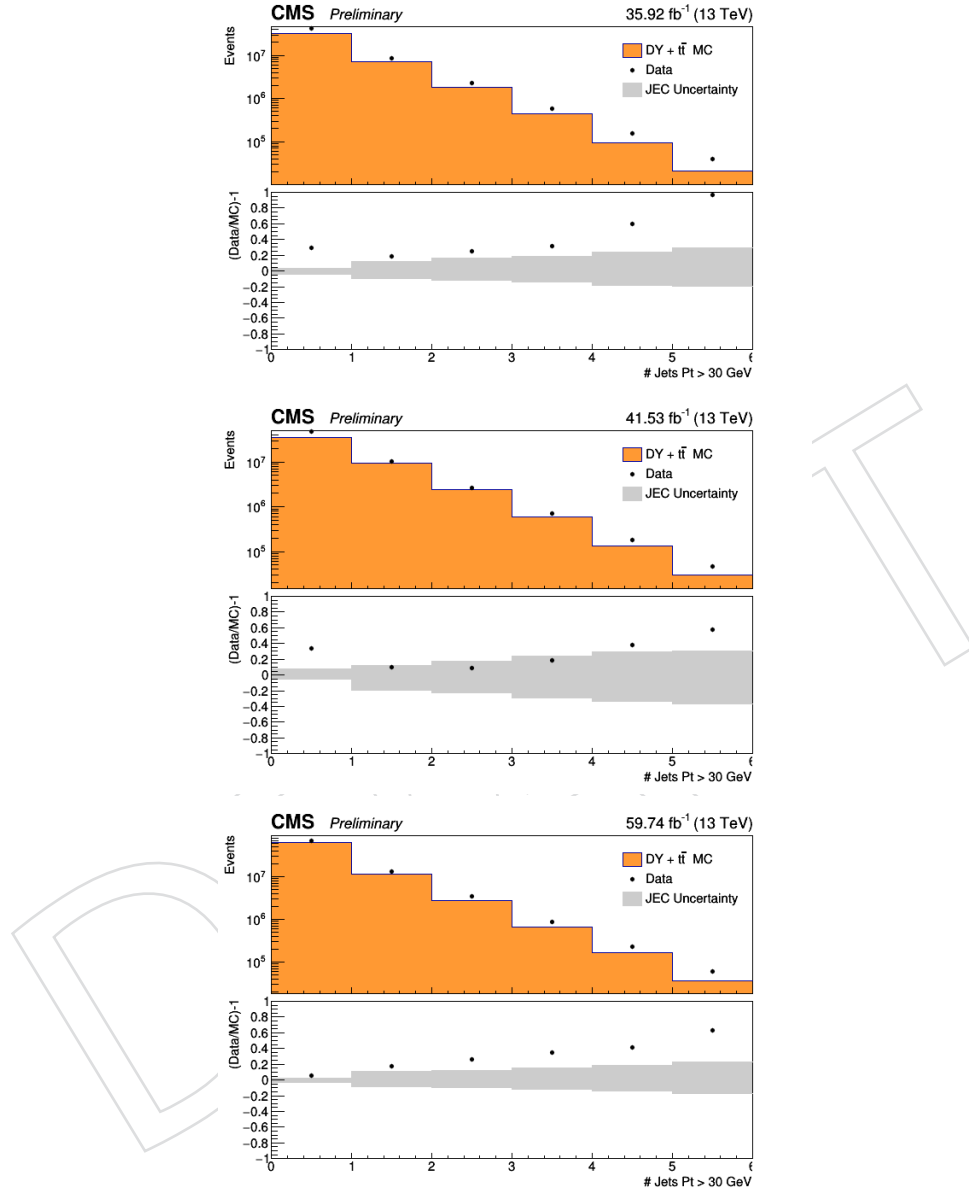


Figure 27: Comparison between data and MC for the jet multiplicity for 2016 (top), 2017 (middle) and 2018 (bottom). $Z \rightarrow ll + \text{jets}$ events are used. MC is normalized to data. Jet ID and Jet PUID are applied. MC samples include DY and $t\bar{t}$. Data/MC ratio plots are shown in the bottom of each plots, together with the uncertainties (shaded histograms) from Jet Energy Corrections.

⁴⁷⁰ **4.5 Object Summary**

- ⁴⁷¹ The requirements on all objects used for the analysis with 2016, 2017 or 2018 data are summarized in the Table 16. In addition, a “ghost-cleaning” procedure is applied to the muons, as
⁴⁷² described in Sec. 4.2.1.
- ⁴⁷⁴ A lepton is declared **loose** if it passes the reconstruction, kinematics and dxy/dz cuts and
⁴⁷⁵ declared **tight** if it passes in addition the identification, isolation and SIP3D requirements.

DRAFT

Table 16: Summary of physics object selection for the $H \rightarrow ZZ \rightarrow 4\ell$ analysis performed on the 2018 data.

Electrons
$p_T^e > 7 \text{ GeV}$ $ \eta^e < 2.5$
$d_{xy} < 0.5 \text{ cm}$ $d_z < 1 \text{ cm}$
$ SIP_{3D} < 4$
BDT ID with isolation with cuts from Tables 11, 12 and 13
Muons
Global or Tracker Muon
Discard Standalone Muon tracks if reconstructed in muon system only
Discard muons with muonBestTrackType==2 even if they are global or tracker muons
$p_T^- > 5 \text{ GeV}$ $ \eta^\mu < 2.4$
$d_{xy} < 0.5 \text{ cm}$ $d_z < 1 \text{ cm}$
$ SIP_{3D} < 4$
PF muon ID if $p_T < 200 \text{ GeV}$, PF muon ID or High- p_T muon ID (Table 14) if $p_T > 200 \text{ GeV}$
$\mathcal{I}_{\text{PF}}^\mu < 0.35$
FSR photons
$p_T^{\text{fl}} > 2 \text{ GeV}$ $ \eta^\gamma < 2.4$
$\mathcal{I}_{\text{PF}}^\gamma < 1.8$
$\Delta R(\ell, \gamma) < 0.5$ $\frac{\Delta R(\ell, \gamma)}{(p_T^\gamma)^2} < 0.012 \text{ GeV}^{-2}$
Jets
$p_T^{\text{jet}} > 30 \text{ GeV}$ $ \eta^{\text{jet}} < 4.7$
$\Delta R(\ell/\gamma, \text{jet}) > 0.4$
Cut-based jet ID (tight WP)
Jet pileup ID (tight WP)
Deep CSV b-tagging (medium WP)

476 5 Event Selection

477 5.1 Trigger Selection

478 The events are required to have fired the High-Level Trigger paths described in section 3.1.1.
 479 Unlike in the Run I analysis, the trigger requirement does not depend on the selected final state:
 480 it is always the OR of all HLT paths. The reason is in Run II we will be targeting associated
 481 production modes that can come with additional leptons, thus improving trigger efficiency
 482 further.

483 5.2 Vertex Selection

484 The events are required to have at least one good primary vertex (PV) fulfilling the following
 485 criteria: high number of degree of freedom ($N_{PV} > 4$), collisions restricted along the z -axis
 486 ($z_{PV} < 24$ cm) and small radius of the PV ($r_{PV} < 2$ cm).

487 5.3 ZZ Candidate Selection

488 The four-lepton candidates are built from what we call **selected leptons**, which are the tight
 489 leptons (defined in sections 4.1.2 and 4.2.1) that pass the $SIP_{3D} < 4$ vertex constraint and the
 490 isolation cuts (defined in sections 4.1.2 and 4.2.2), where FSR photons are subtracted as de-
 491 scribed in Section 4.3. A lepton cross cleaning is applied by discarding electrons which are
 492 within $\Delta R < 0.05$ of selected muons.

493 The construction and selection of four-lepton candidates proceeds according to the following
 494 sequence:

495 1. **Z candidates** are defined as pairs of selected leptons of opposite charge and matching
 496 flavour (e^+e^- , $\mu^+\mu^-$) that satisfy $12 < m_{\ell\ell(\gamma)} < 120$ GeV/ c^2 , where the Z candidate mass
 497 includes the selected FSR photons if any.

498 2. **ZZ candidates** are defined as pairs of non-overlapping Z candidates. The Z candidate
 499 with reconstructed mass $m_{\ell\ell}$ closest to the nominal Z boson mass is denoted as Z_1 , and
 500 the second one is denoted as Z_2 . ZZ candidates are required to satisfy the following list
 501 of requirements:

- 502 • **Ghost removal** : $\Delta R(\eta, \phi) > 0.02$ between each of the four leptons.
- 503 • **lepton p_T** : Two of the four selected leptons should pass $p_{T,i} > 20$ GeV/ c and
 504 $p_{T,j} > 10$ GeV/ c . FSR photons are used.
- 505 • **QCD suppression**: all four opposite-sign pairs that can be built with the four
 506 leptons (regardless of lepton flavor) must satisfy $m_{\ell\ell} > 4$ GeV/ c^2 . Here, se-
 507 lected FSR photons are not used in computing $m_{\ell\ell}$, since a QCD-induced low
 508 mass dilepton (eg. J/Ψ) may have photons nearby (e.g. from π_0).
- 509 • **Z_1 mass**: $m_{Z_1} > 40$ GeV/ c^2
- 510 • **'smart cut'**: defining Z_a and Z_b as the mass-sorted alternative pairing Z candi-
 511 dates (Z_a being the one closest to the nominal Z boson mass), require $\text{NOT}(|m_{Z_a} -$
 512 $m_Z| < |m_{Z_1} - m_Z| \text{ AND } m_{Z_b} < 12)$. Selected FSR photons are included in m_Z 's
 513 computations. This cut discards 4μ and $4e$ candidates where the alternative
 514 pairing looks like an on-shell Z + low-mass $\ell^+\ell^-$. (NB. In Run I, such a situa-
 515 tion was avoided by choosing the best ZZ candidate before applying kinematic
 516 cuts to it, most precisely before the $m_{Z_2} > 12$ GeV/ c^2 cut. The present smart
 517 cut allows to choose the best ZZ candidate after all kinematic cuts.)

- 518 • **four-lepton invariant mass:** $m_{4\ell} > 70 \text{ GeV}/c^2$ (selected FSR photons are in-
519 cluded).

520 3. Events containing at least one selected ZZ candidate form the **signal region**.

521 **5.4 Choice of the best ZZ Candidate**

522 Unlike in the Run I analysis, the best ZZ candidate is now chosen after all kinematic cuts, a
523 change that allows to test other selection strategies for this candidate choice. This is especially
524 relevant for events with more than four selected leptons, having in mind the search for the
525 Higgs boson production modes where associated particles can decay to leptons, such as VH
526 and ttH.

527 For the current analysis, we adopt a different approach compared to Run 1: if more than one
528 ZZ candidate survives the above selection, we choose the one with the highest value of $\mathcal{D}_{\text{bkg}}^{\text{kin}}$
529 (defined in Section ??, except when two candidates consist of the same four leptons in which
530 case the candidate with Z_1 closest in mass to nominal Z boson mass is retained).

DRAFT

531 6 Background Estimation

532 6.1 Irreducible Backgrounds

533 6.1.1 $q\bar{q} \rightarrow ZZ$ Modelling

534 The $q\bar{q} \rightarrow ZZ$ background is generated at NLO, while the fully differential cross section has
 535 been computed at NNLO [48], but are not yet available in a partonic level event generator.
 536 Therefore NNLO/NLO k -factors for the $q\bar{q} \rightarrow ZZ$ background process are applied to the
 537 POWHEG sample. The inclusive cross sections obtained using the same PDF and renormaliza-
 538 zation and factorization scales as the POWHEG sample at LO, NLO, and NNLO are shown in
 539 Table 17. The NNLO/NLO k -factors are applied in the analysis differentially as a function of
 540 $m(ZZ)$.

541 Additional NLO electroweak corrections which depend on the initial state quark flavor and
 542 kinematics are also applied to the $q\bar{q} \rightarrow ZZ$ background process in the region $m(ZZ) > 2m(Z)$
 543 where the corrections have been computed. The differential QCD and electroweak k -factors can
 544 be seen in Figure 28.

QCD Order	$\sigma_{2\ell 2\ell'} (\text{fb})$	$\sigma_{4\ell} (\text{fb})$
LO	$218.5^{+16\%}_{-15\%}$	$98.4^{+13\%}_{-13\%}$
NLO	$290.7^{+5\%}_{-8\%}$	$129.5^{+4\%}_{-6\%}$
NNLO	$324.0^{+2\%}_{-3\%}$	$141.2^{+2\%}_{-2\%}$

Table 17: Cross sections for $q\bar{q} \rightarrow ZZ$ production at 13 TeV

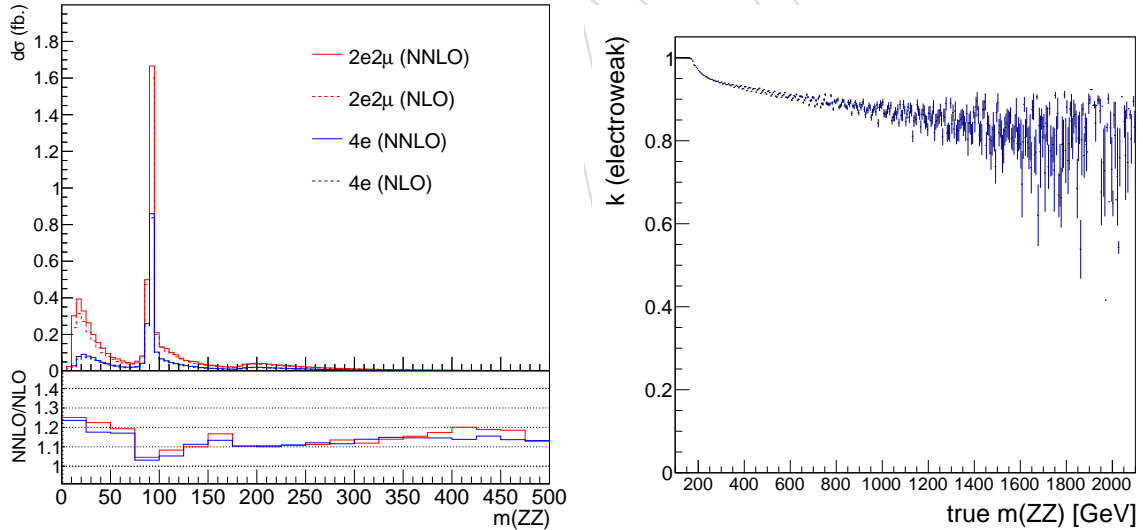


Figure 28: Left: NNLO/NLO QCD K factor for the $q\bar{q} \rightarrow ZZ$ background as a function of $m(ZZ)$ for the 4ℓ and $2\ell 2\ell'$ final states. Right: NLO/NLO electroweak K factor for the $q\bar{q} \rightarrow ZZ$ background as a function of $m(ZZ)$.

545 6.1.2 $gg \rightarrow ZZ$ Modelling

546 Event simulation for the $gg \rightarrow ZZ$ background is done at LO with the generator MCFM 7.0 [33,
 547 34, 49]. Although no exact calculation exists beyond the LO for the $gg \rightarrow ZZ$ background,
 548 it has been recently shown [50] that the soft collinear approximation is able to describe the

background cross section and the interference term at NNLO. Further calculations also show that the K factors are very similar at NLO for the signal and background [51] and at NNLO for the signal and interference terms [52]. Therefore, the same K factor is used for the signal and background [53]. The NNLO K factor for the signal is obtained as a function of $m_{4\ell}$ using the HNNLO v2 Monte Carlo program [54–56] by calculating the NNLO and LO $gg \rightarrow H \rightarrow 2\ell 2\ell'$ cross sections at the small H boson decay width of 4.07 MeV and taking their ratios. The NNLO as well as the NLO K factors and the cross sections from which they are derived are illustrated in Figure 29, along with the NNLO, NLO and LO cross sections at the SM H boson decay width [57].

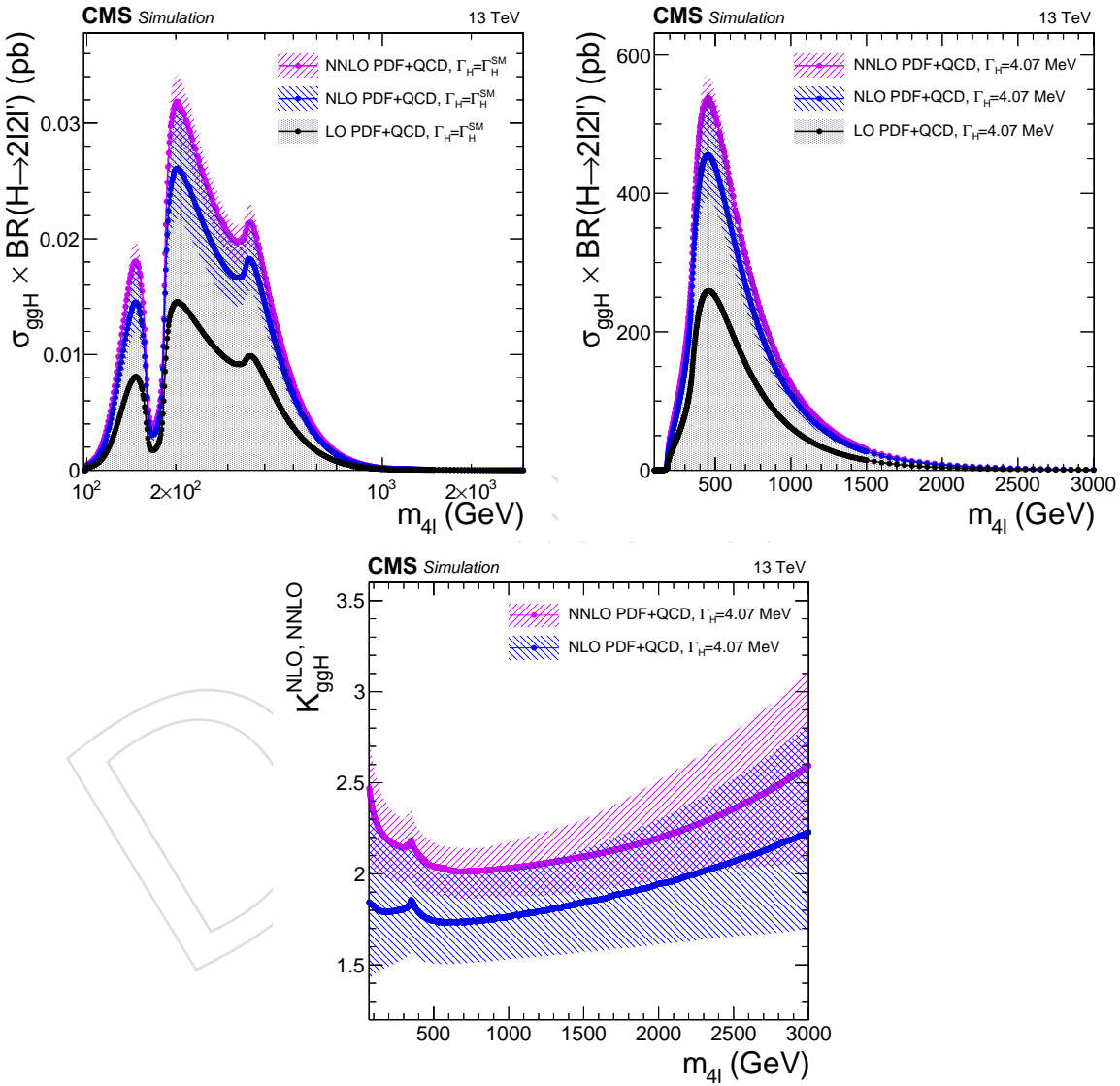


Figure 29: $gg \rightarrow H \rightarrow 2\ell 2\ell'$ cross sections at NNLO, NLO and LO at each H boson pole mass using the SM H boson decay width (top left) or at the fixed and small decay width of 4.07 MeV (top right). The cross sections using the fixed value are used to obtain the K factor for both the signal and the continuum background contributions as a function of $m_{4\ell}$ (bottom).

558 **6.2 Reducible Background**

559 The reducible background for the $H \rightarrow ZZ \rightarrow 4\ell$ analysis, hereafter called $Z + X$, originates
 560 from processes which contain one or more nonprompt leptons in the four lepton final state. The
 561 main sources of nonprompt leptons are non-isolated electrons and muons coming from decays
 562 of heavy flavour mesons, misreconstructed jets (usually originating from light flavour quarks)
 563 and electrons from γ conversions. In this discussion, we will consider a “fake lepton” any jet
 564 misreconstructed as a lepton and any lepton originating from a heavy meson decay. Similarly,
 565 any electron originating from a photon conversion will be considered a “fake electron”.

566 In the $H \rightarrow ZZ \rightarrow 4\ell$ analysis, the rate of these background processes is estimated by mea-
 567 suring the f_e and f_μ probabilities for fake electrons and fake muons which do pass the **loose**
 568 selection criteria (defined in Section 4.1.1 and 4.2.1) to also pass the final selection criteria (de-
 569 fined in Section 5.3). These probabilities, hereafter referred to as fake ratios or fake rates (FR),
 570 are applied in dedicated control samples in order to extract the expected background yield in
 571 the signal region.

572 In the following section, two independent methods are presented to measure both the yields
 573 and shapes of the reducible background, called Opposite-Sign (OS) method and Same-Sign (SS)
 574 method. The final result combines the outcome of the two approaches. The methods are the
 575 same as in the 2016 analysis, although additional cross checks have been performed.

576 **6.2.1 Reducible Background Estimate with Opposite-Sign Leptons**

577 **6.2.1.1 Fake Rate Determination (OS method)** In order to measure the lepton fake ra-
 578 tios f_e and f_μ , we select samples of $Z(\ell\ell) + e$ and $Z(\ell\ell) + \mu$ events that are expected to be
 579 completely dominated by final states which include a Z boson and a fake lepton. These events
 580 are required to have two same flavour, opposite charge leptons with $p_T > 20/10$ GeV passing
 581 the tight selection criteria, thus forming the Z candidate. In addition, there is exactly one lep-
 582 ton passing the loose selection criteria as defined above. This lepton is used as the probe lepton
 583 for the fake ratio measurement. The invariant mass of this lepton and the opposite sign lepton
 584 from the reconstructed Z candidate should satisfy $m_{2l} > 4$ GeV.

585 The fake ratios are evaluated using the tight requirement $|M_{inv}(\ell_1, \ell_2) - M_Z| < 7$ GeV, to re-
 586 duce the contribution from photon (asymmetric) conversions populating low masses. The fake
 587 ratios are measured in bins of the transverse momentum of the loose lepton in the barrel and
 588 endcap regions. The electron and muon fake rates are measured within $|M_{inv}(\ell_1, \ell_2) - M_Z| <$
 589 7 GeV and $E_T^{\text{miss}} < 25$ GeV, separately for the 2016, 2017 and 2018 data, and are shown in
 590 Figure 30.

591 **6.2.1.2 Fake Rate Application (OS method)** Two control samples are obtained as sub-
 592 sets of the four lepton events which pass the first step of the selection (*First Z step*, see sec-
 593 tion 5.3), requiring an additional pair of identified loose leptons of same flavour and opposite
 594 charge, that pass the SIP_{3D} , dxy and dz cuts. The events must satisfy all kinematic cuts applied
 595 for the *Higgs phase space* selection (see 5.3).

596 The first control sample is obtained by requiring that the two loose leptons, which do not make
 597 the Z_1 candidate, do not pass the final selection criteria, while the other two leptons pass the
 598 final selection criteria by definition of the Z_1 . This sample is denoted as “2 Prompt + 2 Fail”
 599 ($2P+2F$) sample. It is expected to be populated with events that intrinsically have only two
 600 prompt leptons (mostly DY , with a small fraction of $t\bar{t}$ and $Z\gamma$ events). The second control
 601 sample is obtained by requiring one of the four leptons not to pass the final identification crite-
 602 ria and selection cuts on SIP , dxy and dz and is denoted as “3 Prompt + 1 Fail” ($3P+1F$) sample.

- 603 The other three leptons should pass the final selection criteria.
- 604 It is expected to be populated with the type of events that populate the 2P+2F region, albeit with
605 different relative proportions, as well as with WZ events that intrinsically have three prompt
606 leptons.
- 607 The control samples obtained in this way, orthogonal by construction to the signal region, are
608 enriched with fake leptons and are used to estimate the reducible background in the signal
609 region. The invariant mass distribution of events selected in the 2P+2F control sample is shown
610 in Figures 31, 32 and 33.
- 611 The expected number of reducible background events in the 3P+1F region, N_{3P1F}^{bkg} , can be com-
612 puted from the number of events observed in the 2P+2F control region, N_{2P2F} , by weighting
613 each event in the region with the factor $(\frac{f_i}{1-f_i} + \frac{f_j}{1-f_j})$, where f_i and f_j correspond to the fake
614 ratios of the two loose leptons:

$$N_{3P1F}^{bkg} = \sum \left(\frac{f_i}{1-f_i} + \frac{f_j}{1-f_j} \right) N_{2P2F} \quad (3)$$

- 615 Figures 34, 35 and 36 shows the invariant mass distributions of the events selected in the 3P+1F
616 control sample, together with the expected reducible background estimated from Eq. 3, stacked
617 on the distribution of WZ and of irreducible background ($ZZ, Z\gamma^* \rightarrow 4\ell$) taken from the sim-
618 ulation.
- 619 Would the fake rates be measured in a sample that has exactly the same background compo-
620 sition as the 2P+2F sample, the difference between the observed number of events in the 3P+1F
621 sample and the expected background predicted from the 2P+2F sample would solely amount
622 to the (small) WZ and $Z\gamma_{conv}$ contribution. Large differences arise because the fake rates used
623 in Eq. 3 do not properly account for the background composition of the 2P+2F control sample.

- 624 In particular, the difference seen in Figure 36 between the observed 3P+1F distribution and the
625 expectation from 2P+2F, in the channels with loose electrons (4e and 2 μ 2e), and concentrated
626 at low masses, is due to photon conversions. This is confirmed explicitly by the simulation.
627 The difference between the 3P+1F observation and the prediction from 2P+2F to recover the
628 missing contribution from conversions - and more generally, in principle, to "correct" for the
629 fact that the fake rates do not properly account for the background composition of the 2P+2F
630 sample. More precisely, the expected reducible background in the signal region is given by the
631 sum of two terms :

- 632 • a "2P2F component", obtained from the number of events observed in the 2P+2F
633 control region, N_{2P2F} , by weighting each event in that region with the factor $\frac{f_i}{1-f_i} \frac{f_j}{1-f_j}$,
634 where f_i and f_j correspond to the fake ratios of the two loose leptons;
- 635 • a "3P1F component", obtained from the difference between the number of observed
636 events in the 3P+1F control region, N_{3P1F} , and the expected contribution from the
637 2P+2F region and ZZ processes in the signal region, $N_{3P1F}^{ZZ} + N_{3P1F}^{bkg}$. The N_{3P1F}^{bkg} is
638 given by Eq. 3 and N_{3P1F}^{ZZ} is the contribution from ZZ which is taken from the sim-
639 ulation. The difference $N_{3P1F} - N_{3P1F}^{bkg} - N_{3P1F}^{ZZ}$, which may be negative, is obtained
640 for each (p_T, η) bin of the "F" lepton, and is weighted by $\frac{f_i}{1-f_i}$, where f_i denotes the
641 fake rate of this lepton. This "3P1F component" accounts for the contribution of re-
642ducible background processes with only one fake lepton (like WZ events), and for

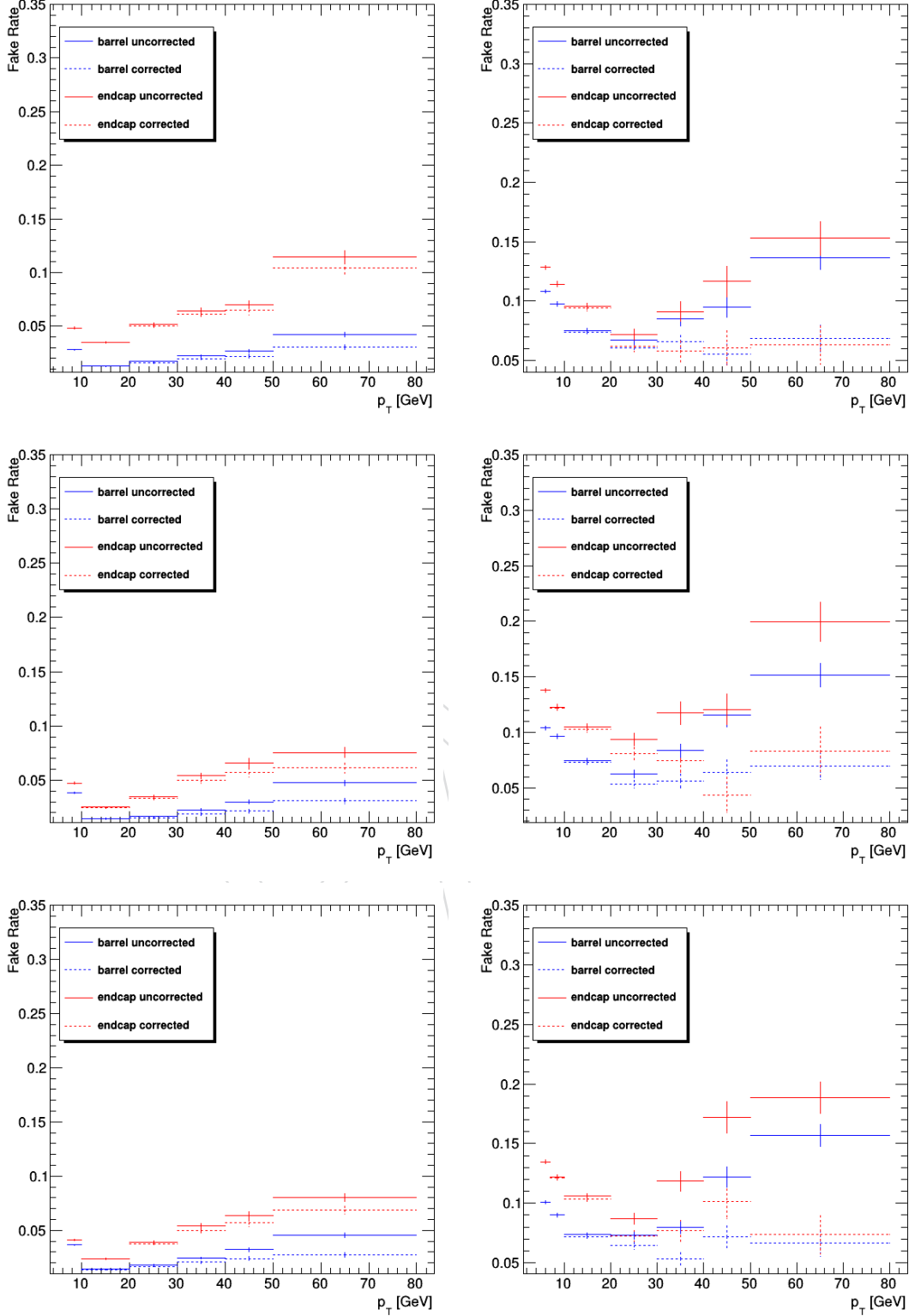


Figure 30: Fake rates as a function of the probe p_T for electrons (left) and muons (right) which satisfy the loose selection criteria, measured in a $Z(\ell\ell) + \ell$ sample in the 2016 (top), 2017 (middle) and 2018 (bottom) data at 13 TeV. The barrel selection includes electrons (muons) up to $|\eta| = 1.479$ (1.2). The fake rates are shown before (dotted lines) and after (plain line) removal of WZ contribution from MC.

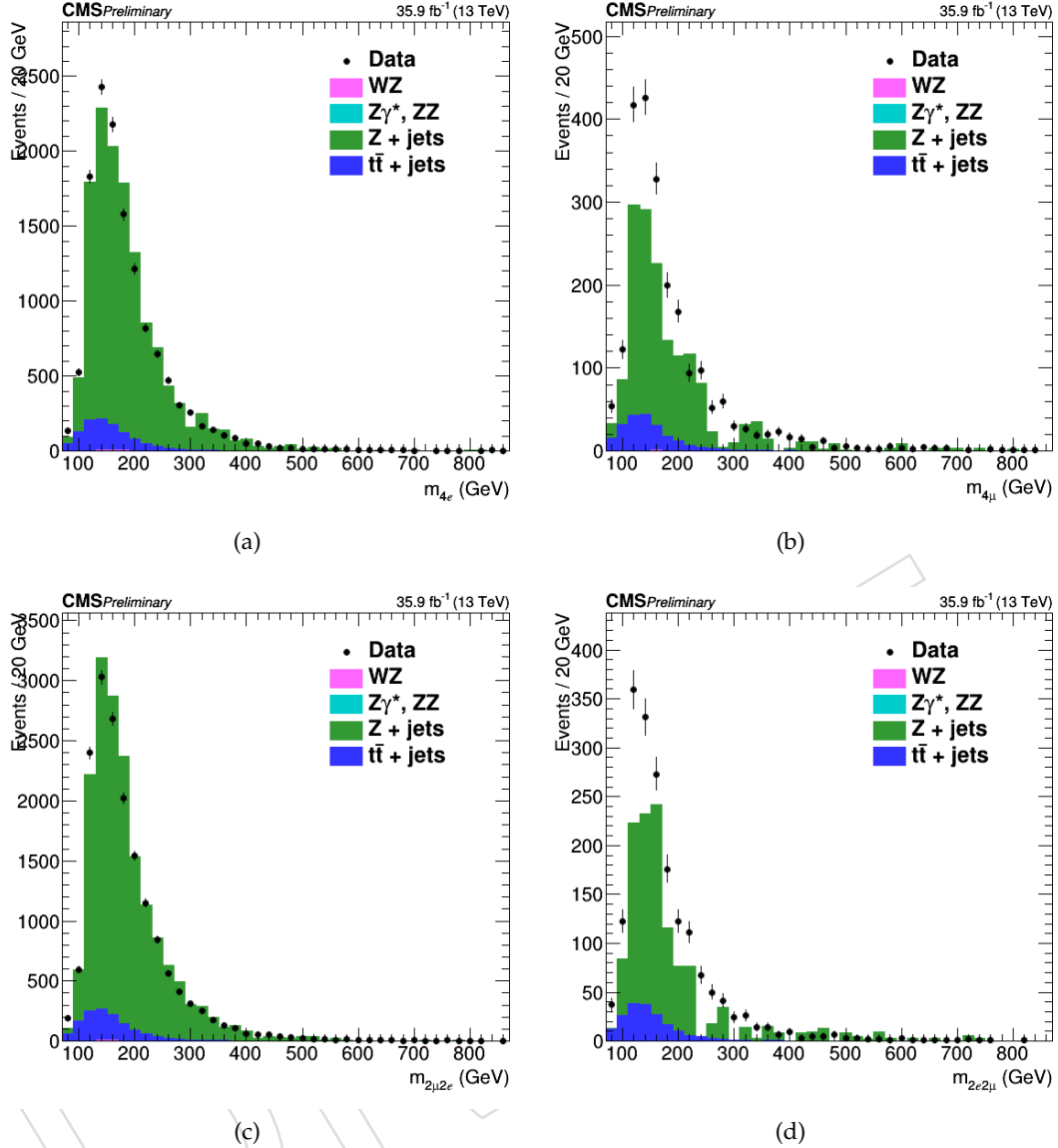


Figure 31: Invariant mass distribution of the events selected in the 2P+2F control sample in the 2016 dataset for all the considered channels: 4e (a), 4μ (b), 2μ2e (c) and 2e2μ (d).

the contribution of other processes (e.g. photon conversions) that are not properly estimated by the 2P2F component, because of the fake rates used.

Therefore, the full expression for the prediction can be symbolically written as:

$$N_{\text{SR}}^{\text{bkg}} = \sum_i \frac{f_i}{(1-f_i)} (N_{\text{3P1F}} - N_{\text{3P1F}}^{\text{bkg}} - N_{\text{3P1F}}^{\text{ZZ}}) + \sum_j \frac{f_i}{(1-f_i)} \frac{f_j}{(1-f_j)} N_{\text{2P2F}} \quad (4)$$

Previous equation is equivalent to the following:

$$N_{\text{SR}}^{\text{bkg}} = \left(1 - \frac{N_{\text{3P1F}}^{\text{ZZ}}}{N_{\text{3P1F}}}\right) \sum_j^{N_{\text{3P1F}}} \frac{f_a^j}{1-f_a^j} - \sum_i^{N_{\text{2P2F}}} \frac{f_3^i}{1-f_3^i} \frac{f_4^i}{1-f_4^i} \quad (5)$$

For channels where the Z_2 candidate is made from two electrons, the contribution of the 3P1F component is positive, and amounts to typically 30% of the total predicted background.

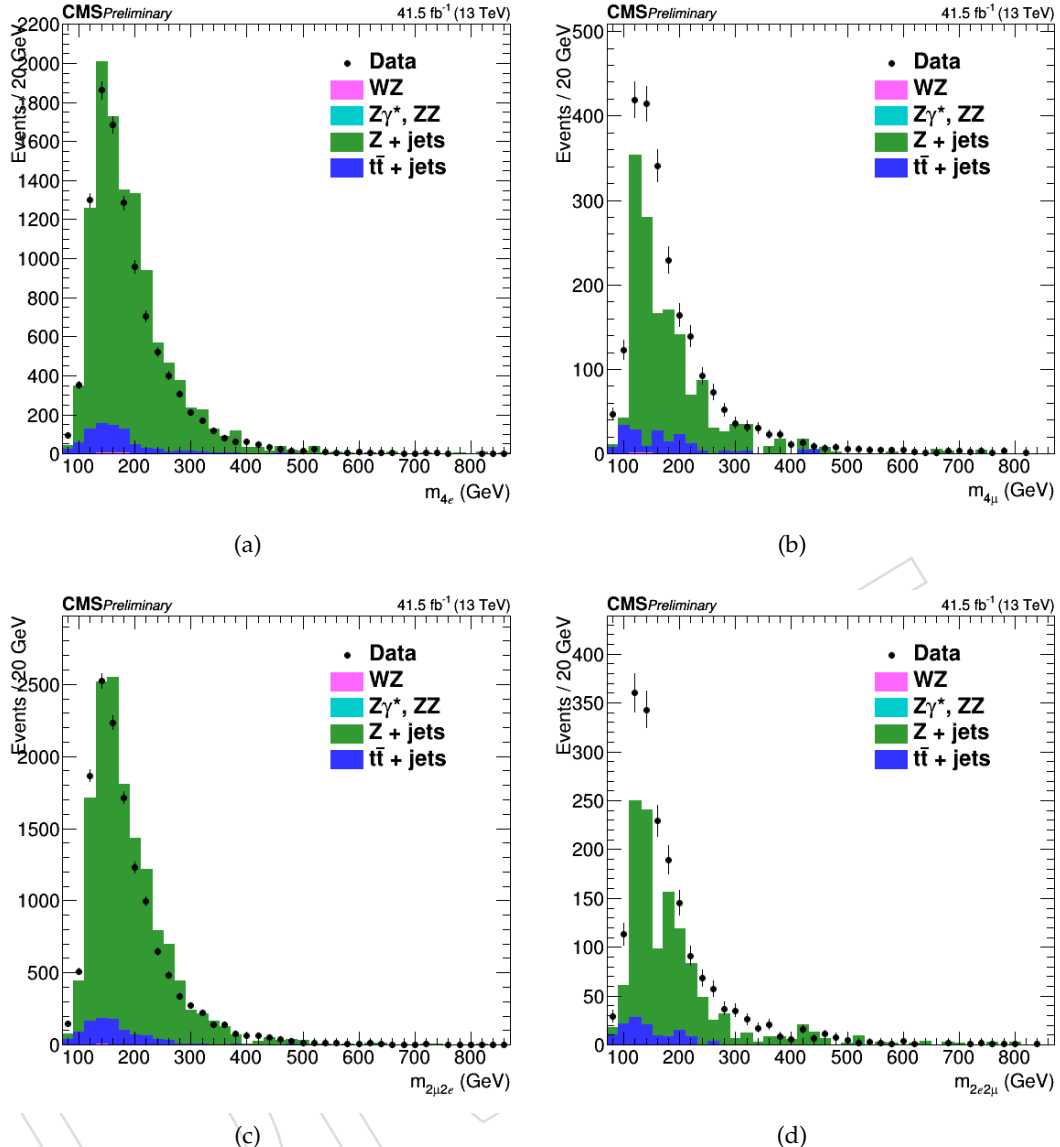


Figure 32: Invariant mass distribution of the events selected in the 2P+2F control sample in the 2017 dataset for all the considered channels: 4e (a), 4 μ (b), 2 μ 2e (c) and 2e2 μ (d).

- 647 For channels with loose muons (4 μ and 2e2 μ), the 3P+1F sample is rather well described by
 648 the prediction from 2P+2F, as seen in Figure 36, and the 3P1F component is mainly driven by
 649 statistical fluctuations in the 3P+1F sample, which are larger than the expectation from WZ
 650 production.
 651 Table 18 shows the expected number of events in the signal regions from the reducible back-
 652 ground processes at 13 TeV for each considered final state and for all three years using the OS
 653 method. The invariant mass distribution of the ZX events obtained from the combination of
 654 the results in the 2P+2F and 3P+1F control samples are shown in Figure 37, 38, 39.

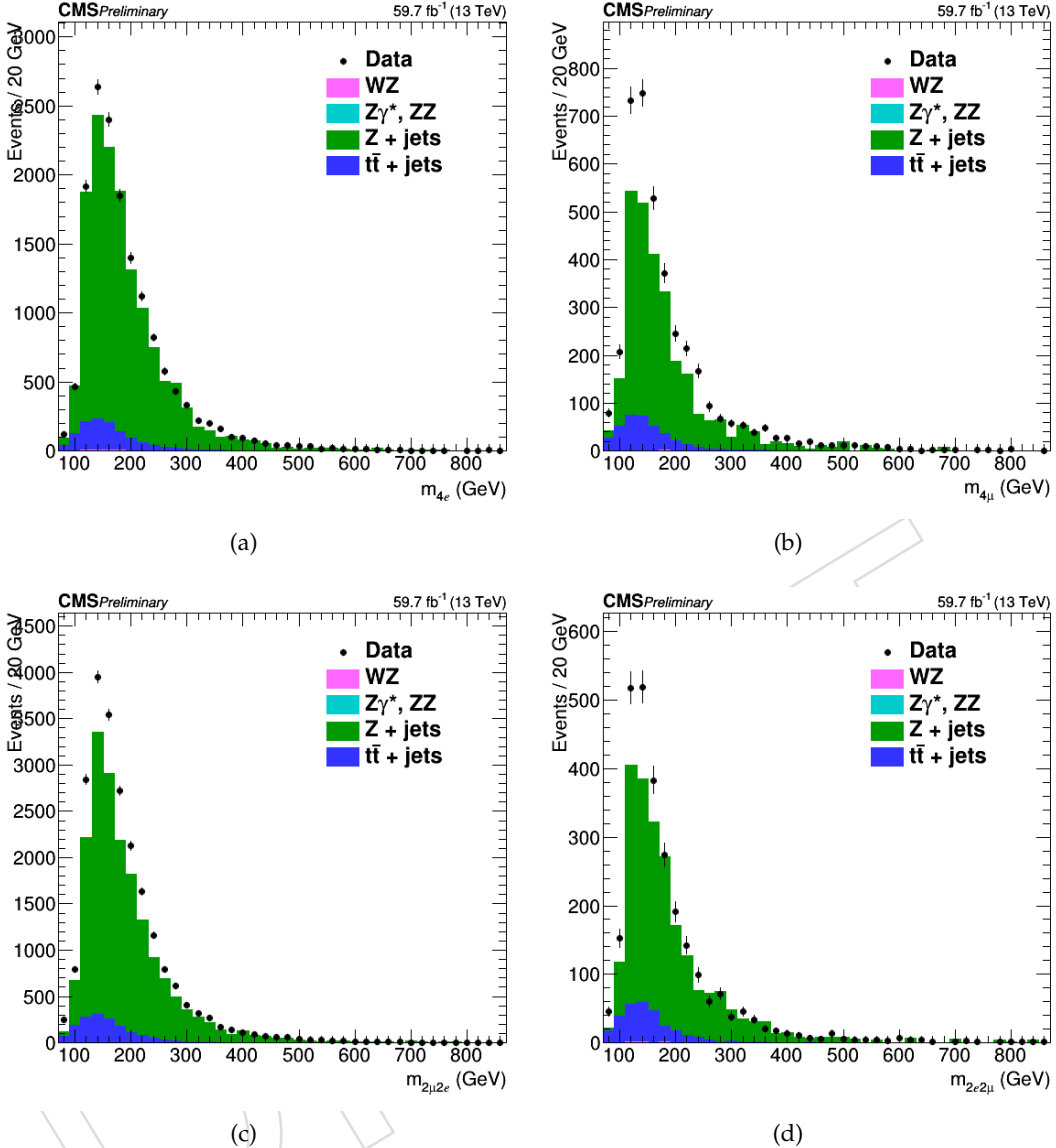


Figure 33: Invariant mass distribution of the events selected in the 2P+2F control sample in the 2018 dataset for all the considered channels: $4e$ (a), 4μ (b), $2\mu 2e$ (c) and $2e 2\mu$ (d).

Channel	$4e$	4μ	$2e 2\mu$	$2\mu 2e$
2016	20.1 ± 6.1	26.9 ± 8.6	25.2 ± 8.0	22.3 ± 6.8
2017	16.2 ± 5.0	32.7 ± 10.3	24.0 ± 7.7	21.3 ± 6.5
2018	25.4 ± 7.7	49.4 ± 15.4	34.2 ± 10.7	33.0 ± 10.0

Table 18: The contribution of reducible background processes in the signal region predicted from measurements in 2016, 2017 and 2018 data using the OS method. The predictions correspond to 35.9 , 41.5 and 59.7 fb^{-1} of data at 13 TeV, respectively.

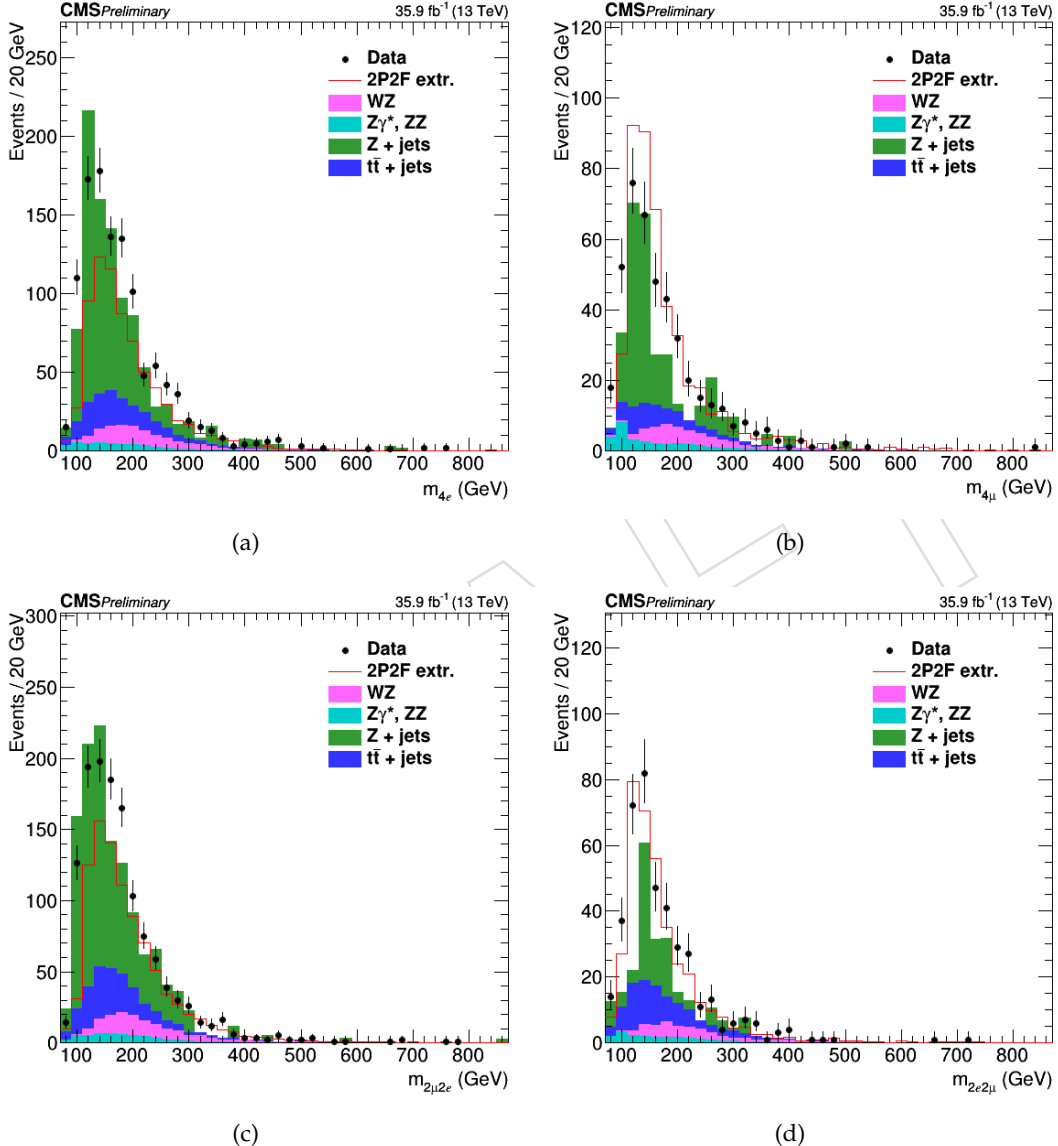


Figure 34: Invariant mass distribution of the events selected in the 3P+1F control sample in the 2016 dataset for all the considered channels: 4e (a), 4 μ (b), 2 μ 2e (c) and 2e2 μ (d).

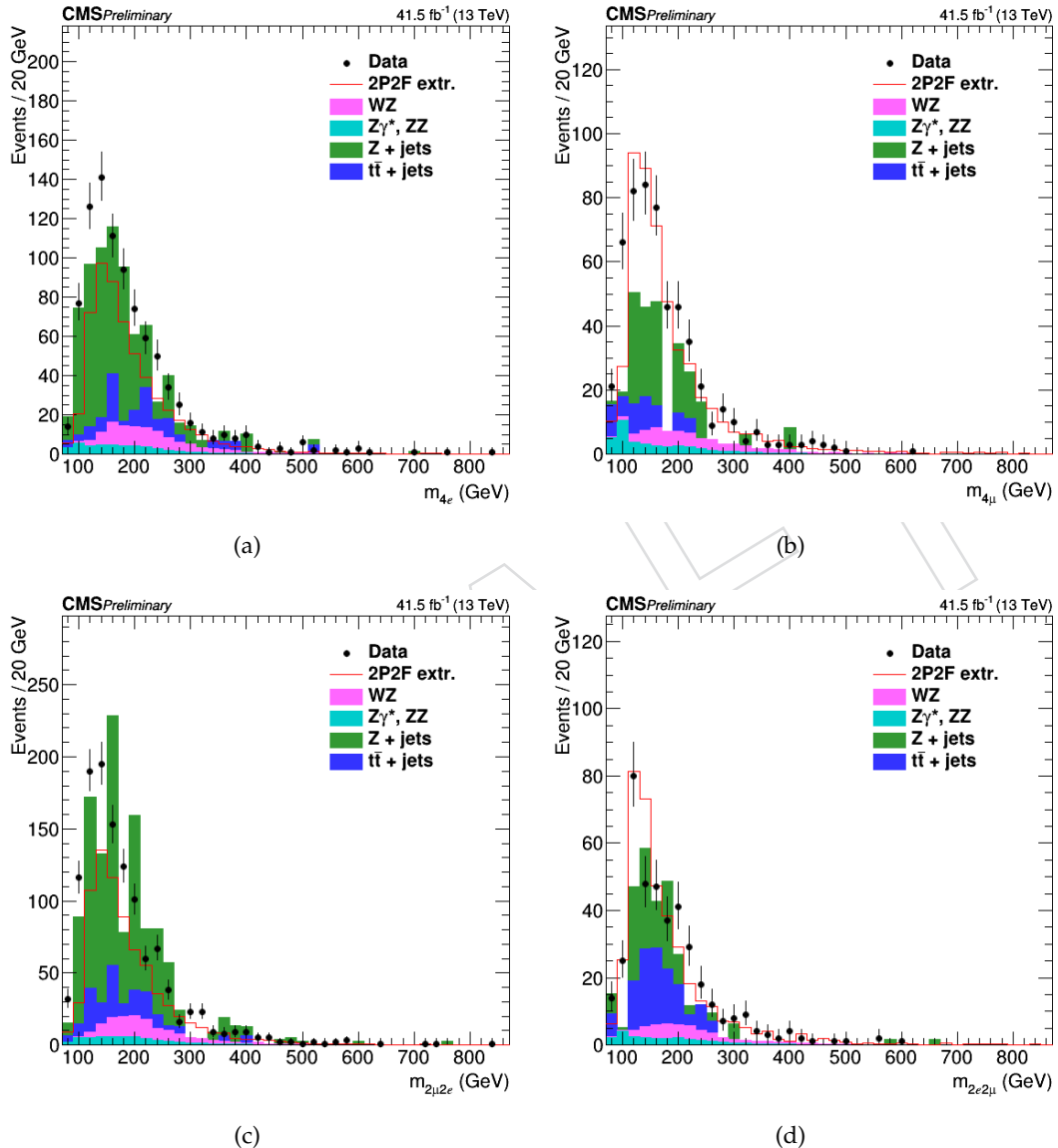


Figure 35: Invariant mass distribution of the events selected in the 3P+1F control sample in the 2017 dataset for all the considered channels: 4e (a), 4 μ (b), 2 μ 2e (c) and 2e2 μ (d).

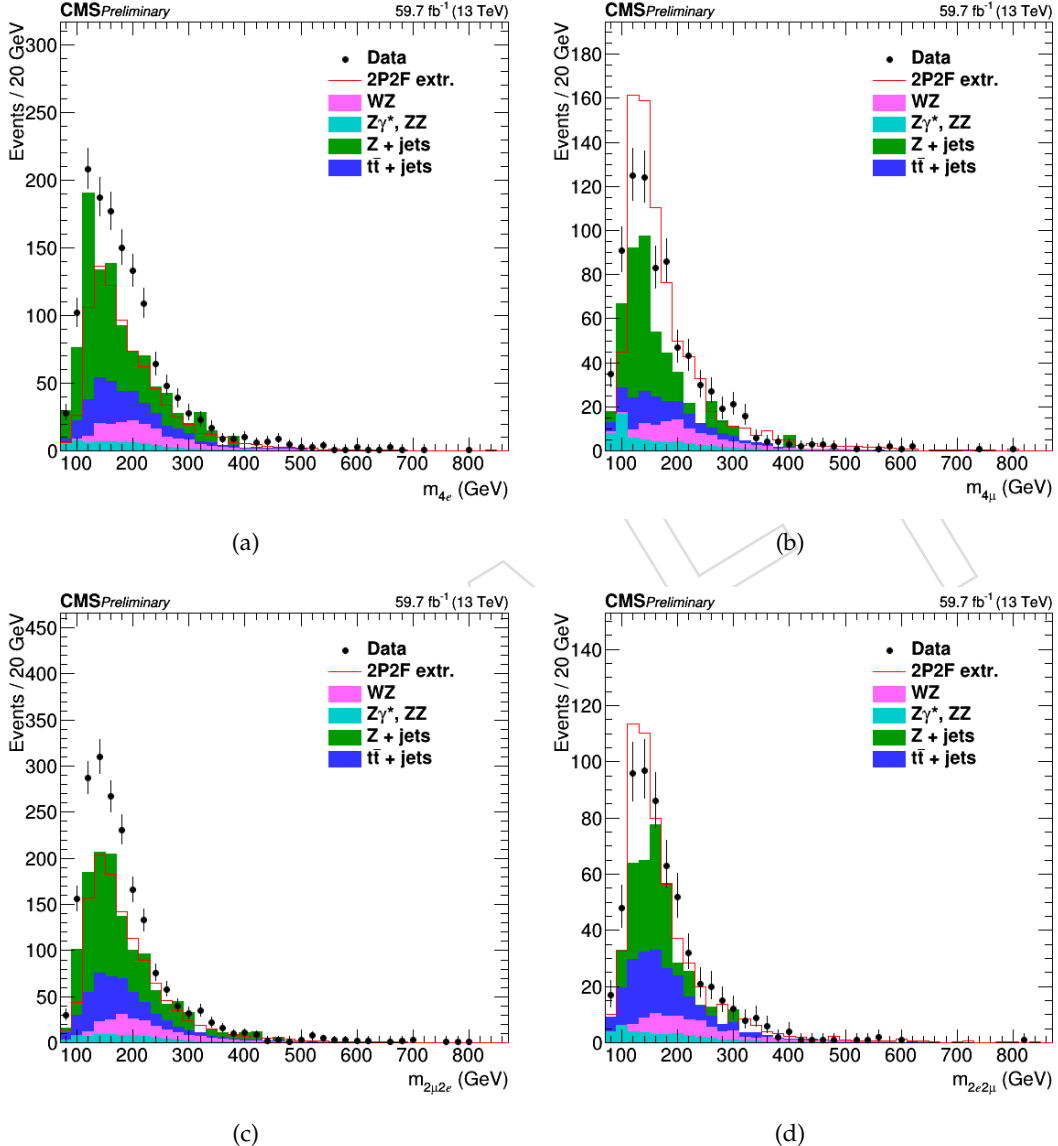


Figure 36: Invariant mass distribution of the events selected in the 3P+1F control sample in the 2018 dataset for all the considered channels: 4e (a), 4 μ (b), 2 μ 2e (c) and 2e2 μ (d).

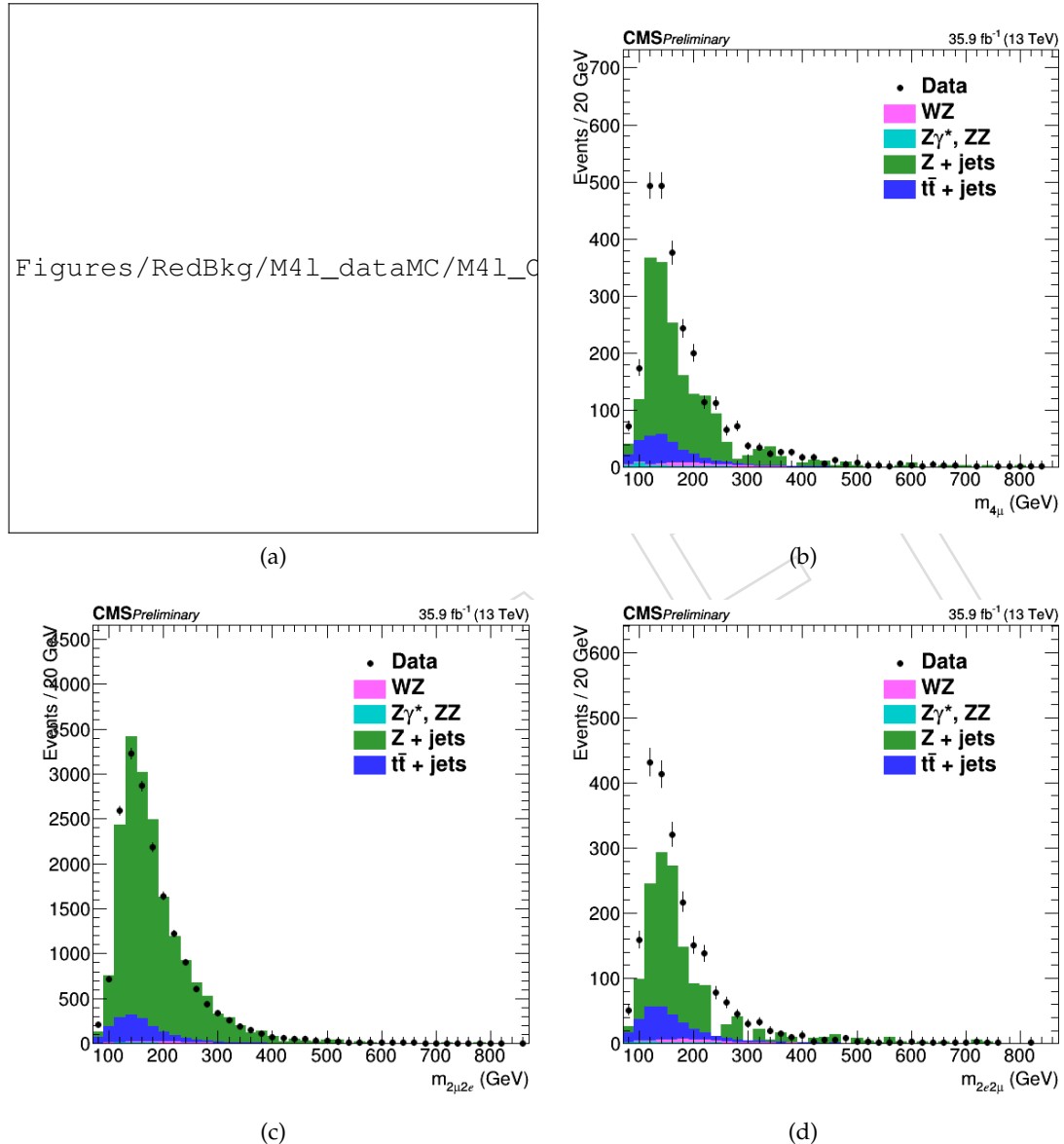


Figure 37: Invariant mass distribution of the events selected in the 2P+2F and 3P+1F control samples in the 2018 dataset for all the considered channels: 4e (a), 4μ (b), 2μ2e (c) and 2e2μ (d) for 2016 data.

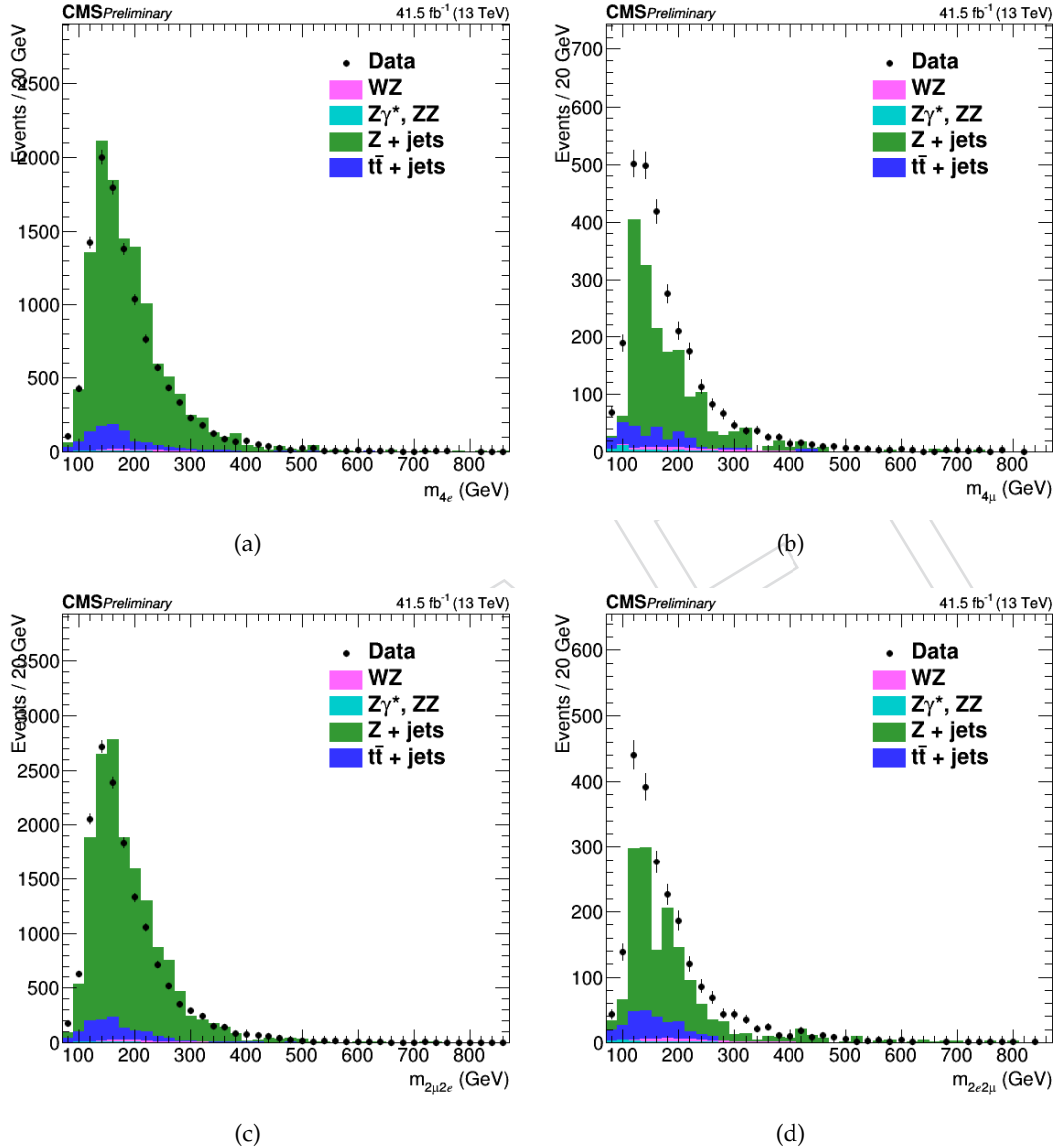


Figure 38: Invariant mass distribution of the events selected in the 2P+2F and 3P+1F control samples in the 2018 dataset for all the considered channels: 4e (a), 4μ (b), 2μ2e (c) and 2e2μ (d) for 2017 data.

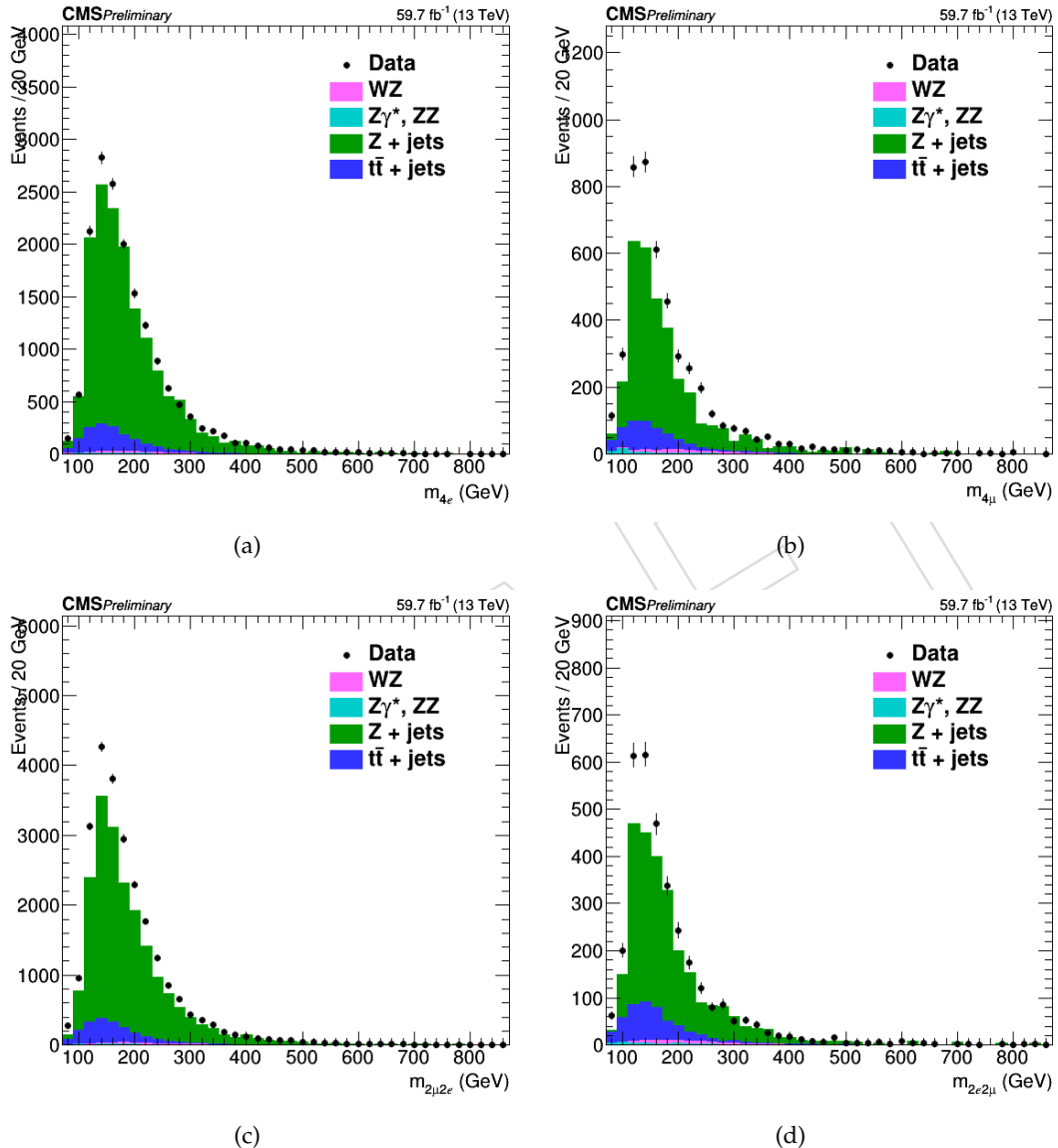


Figure 39: Invariant mass distribution of the events selected in the 2P+2F and 3P+1F control samples in the 2018 dataset for all the considered channels: 4 e (a), 4 μ (b), 2 μ 2 e (c) and 2 e 2 μ (d) for 2018 data.

655 6.2.2 Reducible Background Estimate with Same-Sign Leptons

656 This method used to predict the reducible background allows to have an inclusive measure-
 657 ment of the all the main reducible backgrounds at the same time.

658 The control sample is obtained as a subset of the events that satisfy the first step of the selection
 659 (*First Z step*, see section 5.3), requiring an additional pair of loose leptons of same sign (to avoid
 660 signal contamination) and same flavour (SS-SF: $e^\pm e^\pm, \mu^\pm \mu^\pm$). The SS-SF leptons are requested
 661 to pass the SIP_{3D} , dxy and dz cuts, while no identification requirements are imposed. The
 662 reconstructed invariant mass of the SS-SF leptons has to satisfy $m_{\ell\ell} > 12$ GeV, $m_{\ell\ell} < 120$ GeV,
 663 the reconstructed four-lepton invariant mass is required to satisfy $m_{4\ell} > 100$ GeV/ c^2 , and the
 664 QCD suppression cut (see 5.3) is applied. The inclusive number of reducible background events
 665 in the signal region is derived from this set of events and from the probability for the two
 666 additional leptons to pass the isolation and identification analysis cuts, obtained from the fake
 667 rate measurement presented in section 6.2.2.1.

Starting from the control sample previously described, the final reducible background prediction in the signal region is given by the following expression:

$$N_{\text{expect}}^{Z+X} = N^{\text{DATA}} \times \left(\frac{\text{OS}}{\text{SS}}\right)^{\text{MC}} \times f_1 \times f_2 \quad (6)$$

668 where:

- 669 • N^{DATA} is the number of events in the control region,
- 670 • $\left(\frac{\text{OS}}{\text{SS}}\right)^{\text{MC}}$ is a correction factor between opposite sign and same sign control samples,
- 671 • f_1 and f_2 are the fake rates of each additional loose lepton, parameterised as a func-
 672 tion of p_T and η .

673 **6.2.2.1 Fake Rate Determination (SS method)** The lepton fake rates are determined in
 674 the very similar way as it was described before for the OS method. Samples of $Z(\ell\ell) + e$ and
 675 $Z(\ell\ell) + \mu$ events are selected in the same way except that the mass window around the nominal
 676 Z mass is set to $40 \text{ GeV} < M_{\text{inv}}(\ell_1, \ell_2) < 120 \text{ GeV}$, as in the signal region ("SS phase space").
 677 Despite the cut on the missing transverse energy, a contamination of real leptons from WZ
 678 events is still visible at high p_T . This contribution is thus subtracted from the final fake rate,
 679 using the estimation given by the Monte Carlo. The fake rates for muon are shown in Figure 40
 680 for both muons in the barrel ($|\eta| < 1.2$) and in the endcaps ($|\eta| > 1.2$).

681 For electrons, events where a radiated photon makes an asymmetric conversion, where one
 682 low p_T leg is not identified, contribute to the $Z + e$ sample that is used to measure the electron
 683 fake rate. While the requirement $|M_{\text{inv}}(\ell_1, \ell_2) - M_Z| < 7 \text{ GeV}$ ("OS phase space") largely
 684 suppresses FSR of photons radiated off the lepton legs, these radiations occur at a much larger
 685 rate in the "SS phase space". As a result of this enhanced contribution from conversions, the
 686 electron fake rates measured within the SR phase space are larger than the "OS fake rates".

687 However, the relative fraction of FSR conversions is not the same in the "SS phase space"
 688 and in the control sample (defined below) where the fake rates will be applied. A correc-
 689 tion accounting for this difference must be applied to the fake rates measured within the SS
 690 phase space, in order to obtain average fake rates that are appropriate for the control sam-
 691 ple. To determine this correction, several fake rate samples of $Z(l\bar{l}) + e$ events are defined
 692 by applying different cuts on $M_{\text{inv}}(\ell_1, \ell_2)$ or on $M_{\text{inv}}(\ell_1, \ell_2, e)$. In addition to the "OS fake
 693 rate sample", where $|M_{\text{inv}}(\ell_1, \ell_2) - M_Z| < 7 \text{ GeV}$ ensures a minimal amount of conversions
 694 from FSR photons, one defines a sample that is maximally enriched in FSR conversions by
 695 $|M_{\text{inv}}(\ell_1, \ell_2, e) - M_Z| < 5 \text{ GeV}$, as well as samples with an intermediate contamination from

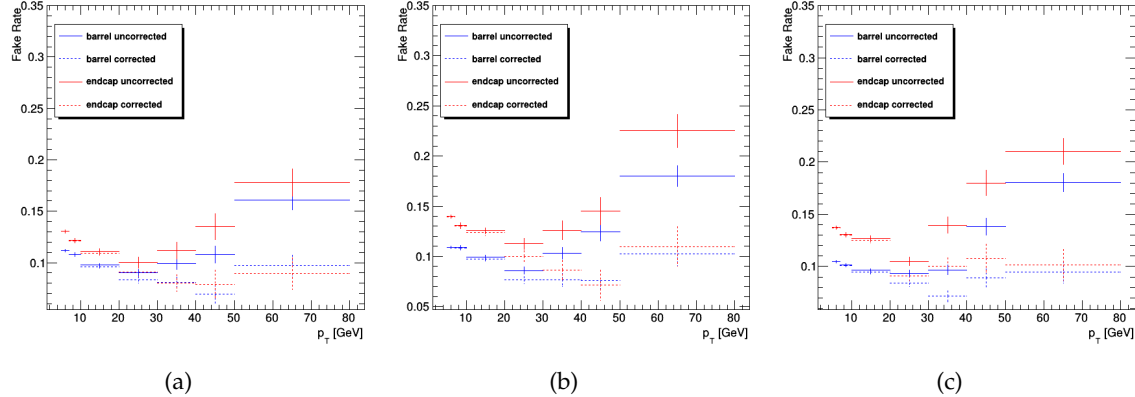


Figure 40: Fake rates as a function of the probe p_T for muons which satisfy the loose selection criteria, measured in a $Z(\ell\ell) + \ell$ sample in the 2016 (top), 2017 (middle) and 2018 (bottom) data at 13 TeV. The barrel selection includes electrons (muons) up to $|\eta| = 1.479$ (1.2). The fake rates are shown before (dotted lines) and after (plain line) the removal of the WZ contribution from the simulation.

696 FSR conversions ($60 \text{ GeV} < M_{\text{inv}}(\ell_1, \ell_2) < 120 \text{ GeV}$). In each sample, one determines in several
697 (p_T, η) bins for the loose electron:

- 698
 - the fake rate ratio;
699 - the average value of the expected inner missing hits ($N_{\text{miss.hits}}$ in the following), vari-
700 able useful to tag conversions.

701 In a given (p_T, η) bin, both the measured fake rate and the average $\langle N_{\text{miss.hits}} \rangle$ are expected
702 to grow linearly with the fraction of conversions. Hence, one expects a linear dependence of
703 the fake rate with respect to $\langle N_{\text{miss.hits}} \rangle$. This linear behaviour is demonstrated in Figure 41,
704 and linear fits are made in each (p_T, η) bin, which relate the fake rate to $\langle N_{\text{miss.hits}} \rangle$. Finally,
705 one looks at the loose electrons in the control sample where the fake rate will be applied, and
706 $\langle N_{\text{miss.hits}} \rangle$ is measured in each (p_T, η) bin. The proper average fake rate corresponding to
707 the control sample is then determined from the linear relation derived previously. Figure 42
708 shows examples of the resulting corrected fake rates, together with the fake rates measured
709 in the SS phase space. It can be seen that the correction for the actual fraction of conversions
710 that is present in the control sample lowers the fake rates considerably with respect to what is
711 measured in the SS phase space. The determination of these corrected fake rates mostly suffers
712 from the limited statistics of the control sample, which translates into a large uncertainty on
713 $\langle N_{\text{miss.hits}} \rangle$, the error on each dot being the fake rate obtained from the linear relations using
714 the error on the $\langle N_{\text{miss.hits}} \rangle$.

715 **6.2.2.2 Fake Rate Application (SS method)** Figure 43 shows the invariant mass distri-
716 bution of events in control samples with SS-SF loose leptons, for channels with loose electrons
717 ($4e$ and $2\mu 2e$) and channels with loose muons (4μ and $2e 2\mu$), for the 2018 dataset at 13 TeV. The
718 prediction from the Monte Carlo simulation is also shown.

719 A good agreement is achieved between data and MC for the channels with loose electrons. The
720 agreement is not as good for loose muons but this has no impact on the final result as only data
721 are used in the end.

722 The differences in rates between OS and SS samples are estimated using data and are used to

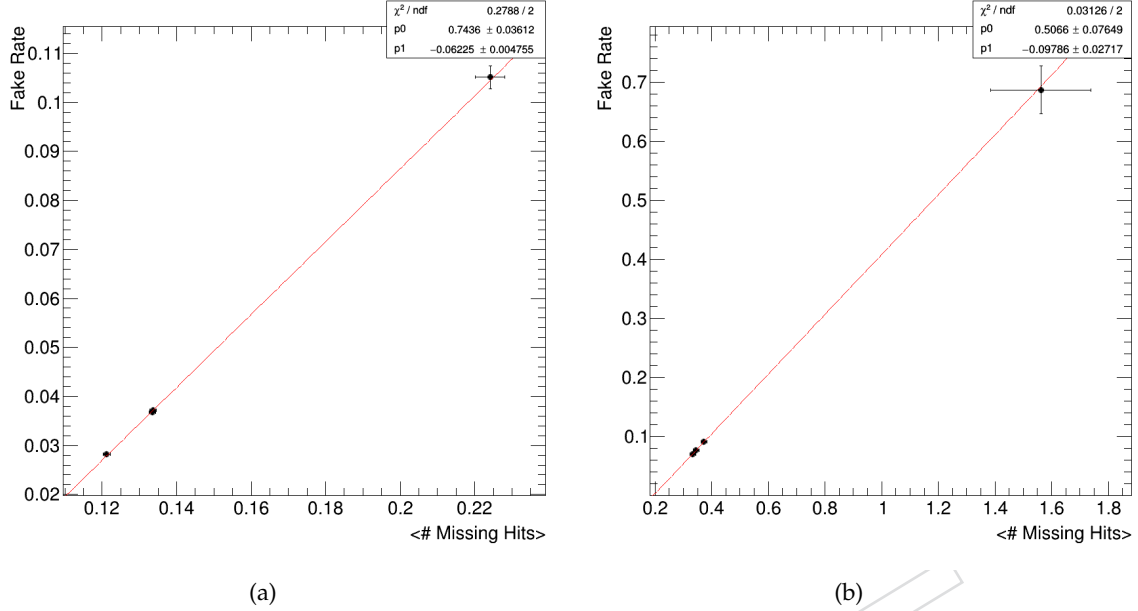


Figure 41: Examples of the correlation between the fake rate and the fraction of loose electrons for which the track has one missing hit in the pixel detector for $7 < p_T < 10$ GeV electrons in the barrel (left) and for $30 < p_T < 40$ GeV electrons in the endcaps (right). Each dot shows the measurements made in a given $Z + \text{loose } e$ sample. Results are produced at 13 TeV with 35.9 fb^{-1} data.

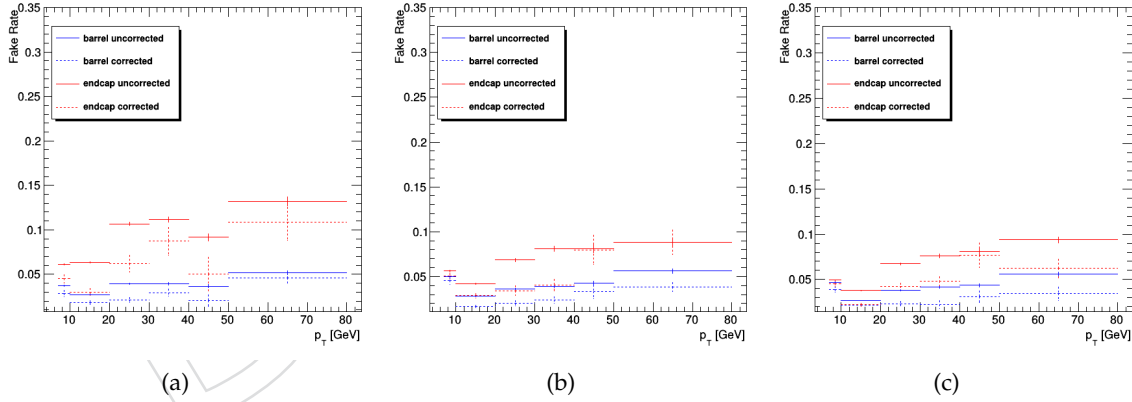


Figure 42: Average fake rates to be applied to the control sample of SS method (plain line), compared to the fake rates measured in the SS phase space (dotted line), for electrons in the barrel (blue) and in the endcaps (red). Results are produced at 13 TeV with 2016, 2017, and 2018 data.

723 compute the correction factor in Eq. 6 for the final data-driven estimation. They are given for
 724 each year in Table 19.

725 The event yields expected from the $Z+X$ in the signal region, in the mass range $m_{4\ell} > 70$ GeV/c^2 ,
 726 are calculated for each final state. The background is due to the systematic introduced when es-
 727 timating the background composition. The total error is obtained with a quadrature sum for the
 728 statistical, background composition and correction systematics. Table 20 shows the expected

Channel	4e	2 μ 2e	4 μ	2e2 μ
2016	1.00 ± 0.01	1.00 ± 0.01	1.00 ± 0.03	1.00 ± 0.03
2017	1.01 ± 0.01	1.00 ± 0.01	1.04 ± 0.03	1.01 ± 0.03
2018	1.01 ± 0.01	1.00 ± 0.01	1.03 ± 0.02	1.03 ± 0.02

Table 19: The OS/SS ratios used to estimate the number of ZX events with the SS method for each final state in all three years.

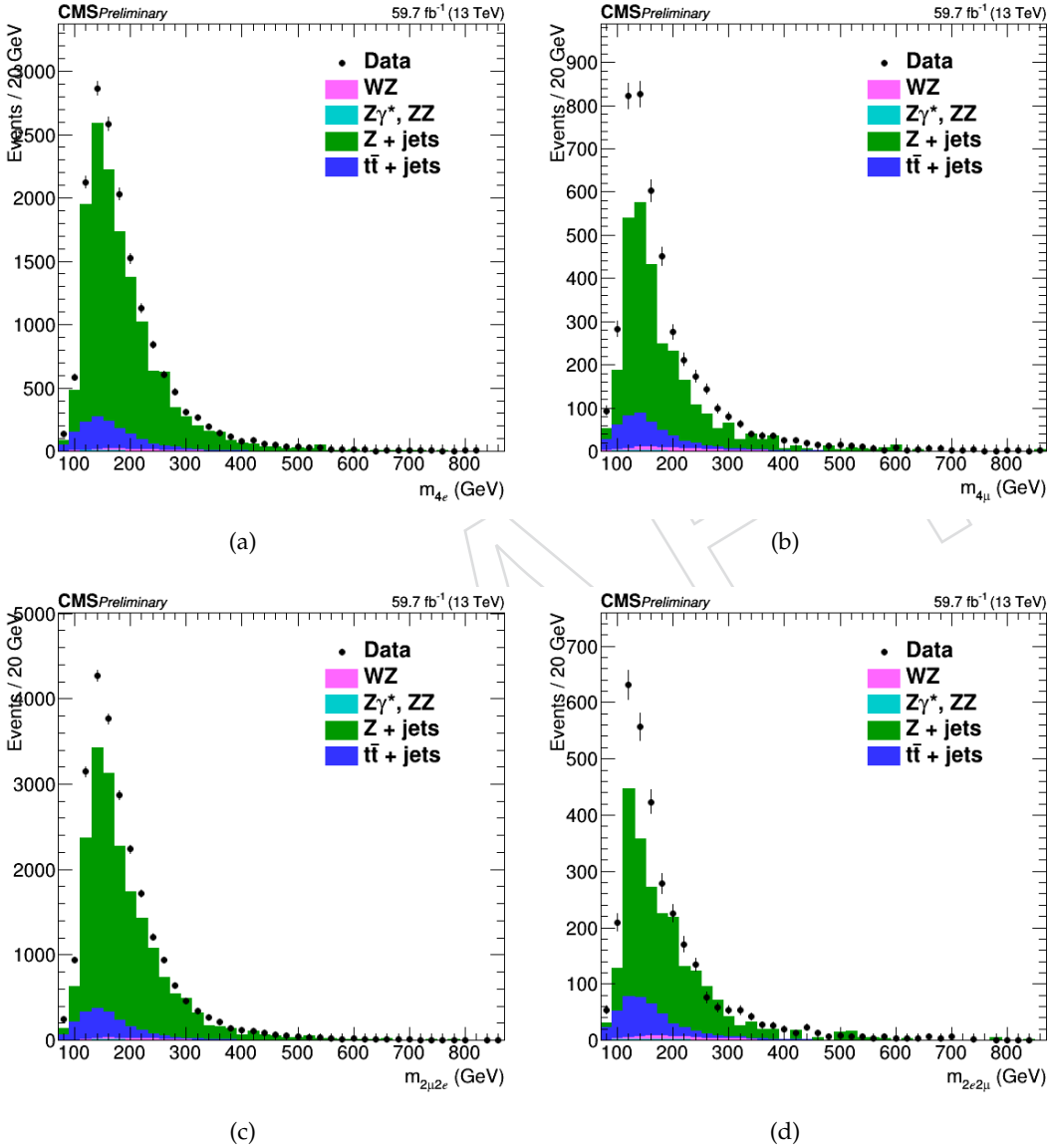


Figure 43: Invariant mass distribution of the events selected in the SS-SF control samples for all the considered final states in 2018 data: 4e (a), 4 μ (b), 2 μ 2e (c) and 2e2 μ (d).

729 number of events in the signal regions from the reducible background processes at 13 TeV for
 730 each considered final state and for all three years using the SS method.

Channel	4e	4 μ	2e2 μ	2 μ 2e
2016	13.0 ± 5.4	29.7 ± 9.1	24.8 ± 7.6	16.7 ± 7.0
2017	10.9 ± 4.0	33.6 ± 10.3	26.3 ± 8.1	14.7 ± 5.5
2018	16.0 ± 5.9	52.2 ± 15.8	37.4 ± 11.4	23.3 ± 8.5

Table 20: The contribution of reducible background processes in the signal region predicted from measurements in 2016, 2017 and 2018 data using the SS method. The predictions correspond to 35.9, 41.5 and 59.7 fb^{-1} of data at 13 TeV, respectively.

731 **6.2.2.3 Fake Rate in the VBF-tagged categories** The FR are currently evaluated inclu-
 732 sively in the analysis: in fact, an average fake rate is used to evaluate ZX yields in each STXS
 733 category instead of dedicated ones. Given that the VBF category can be particularly affected by
 734 this approach, a detailed study of the FR variation in different Z+L phase spaces designed to
 735 mimic VBF has been performed using 2018 data. However, a realistic design of the VBF phase
 736 space is not completely reproducible in the three leptons CR without exploiting the informa-
 737 tion given by the kinematic discriminants. In order to identify events targeting VBF-tagged
 738 categories, the following requirements on jets are applied:

- 739 • an angular separation between the additional lepton and each jet larger than 0.4,
 740 otherwise the jet is discarded;
- 741 • the presence of two or three jets and at most one b tagged jet OR at least four jets
 742 without b tagged jets;
- 743 • an angular separation between the pair of two leading jets larger than 0.5 and a dijet
 744 invariant mass greater than 450 GeV.

745 Furthermore, FR in the CR Z+L with 0/1/2 jets have been studied as well as the FR in the
 746 phase space complementary to the VBF-like one. Figure 45 shows the FR curves obtained
 747 in each category for both electrons and muons in the barrel and endcap region using the SS
 748 method and Figure ?? shows the same distributions using the OS method. While the curve
 749 in the "non VBF-tagged" region is perfectly in agreement with the inclusive one (as a result
 750 of the contribution of the 0/1/2 jet categories), the FR variation in the 0/1/2 jets and VBF-
 751 like categories is significant, especially for muons. As a consequence, large discrepancies are
 752 observed in the final estimated yields in VBF categories (Table 21).

753 In principle, the uncertainty on the background composition of the CR was designed to cover
 754 for this effect, but considering that the effect seems very large, the possible impact on the anal-
 755 ysis has been checked explicitly. An extreme situation has been studied by inflating the Z+X
 756 uncertainty by 100% in the datacards in VBF-tagged categories and comparing stage 0 signal
 757 strengths, both expected and observed, using the standard Z+X uncertainty and inflating it in
 758 VBF categories (Table 22). The results show that the expected uncertainty does not change and
 759 the observed signal strengths change only very slightly (2nd digit) within the uncertainties.

760 In conclusion, the current approach based on an inclusive FR assumed identical for all the
 761 production categories is not correct because FR is indeed different for VBF-tagged categories.
 762 Nevertheless, the final impact on the analysis is found to be not significant due to the kinematic
 763 discriminant used in the fit and the fact that Z+X yields are rather insignificant, so that the
 764 current strategy is kept for this analysis and more effort to have a category specific Z+X estimate
 765 in the future Run 3 analysis will be invested.

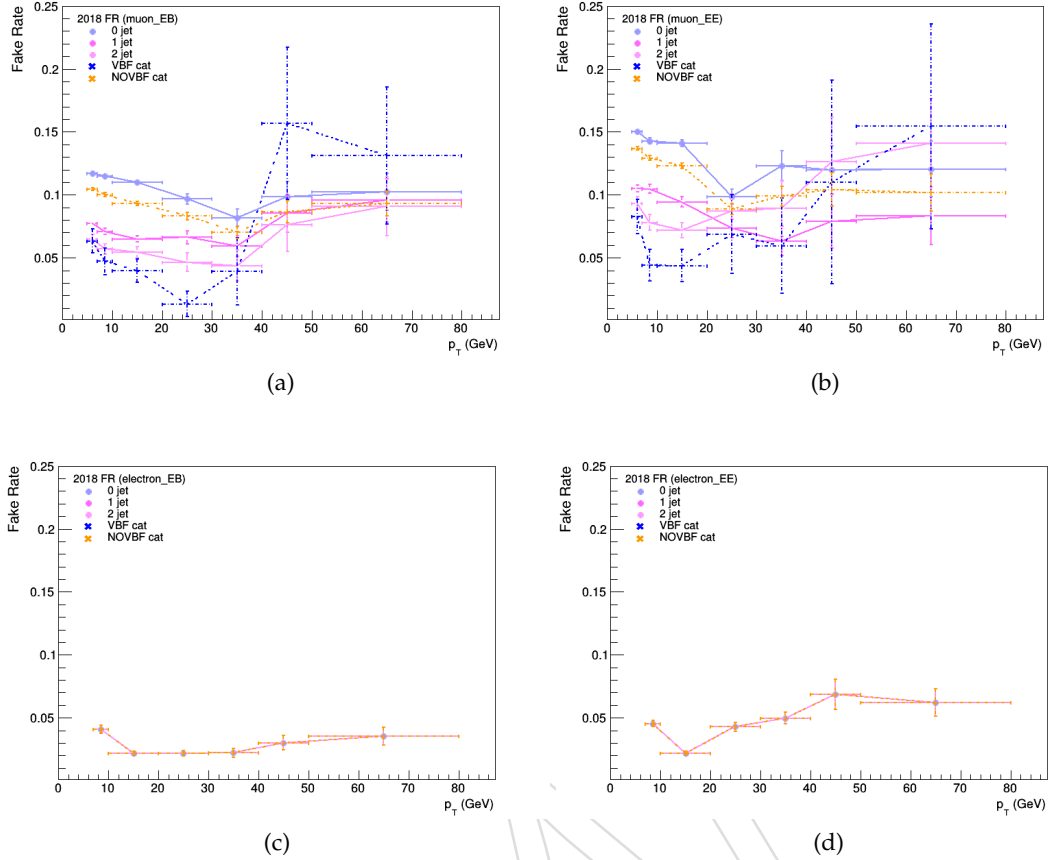


Figure 44: FR curves in the 0/1/2/VBF-tagged and non VBF-tagged categories for muons (top) and electrons (bottom) in the barrel (left) and endcap (right) region obtained using SS method.

Table 21: Comparison between combined ZX yields in the VBF-tagged categories using inclusive and dedicated FR.

CATEGORY	Inclusive FR				Dedicated FR			
	$4l$	4μ	$4e$	$2e2\mu$	$4l$	4μ	$4e$	$2e2\mu$
VBF_1j	1.047	0.391	0.147	0.509	0.663	0.185	0.113	0.365
VBF_2j	0.882	0.295	0.097	0.490	0.054	0.011	0.016	0.028
VBF_2j_mjj_350_700_2j	0.040	0.026	0.003	0.011	0.004	0.000	0.000	0.004
VBF_2j_mjj_GT700_2j	0.016	0.013	0.002	0.001	0.091	0.018	0.039	0.034
VBF_2j_mjj_GT350_3j	0.997	0.444	0.104	0.450	0.001	0.001	0.000	0.000
VBF_GT200_2J	0.021	0.019	0.001	0.001	0.015	0.001	0.001	0.014
Inclusive VBF	3.002	1.188	0.353	1.461	0.828	0.216	0.169	0.444

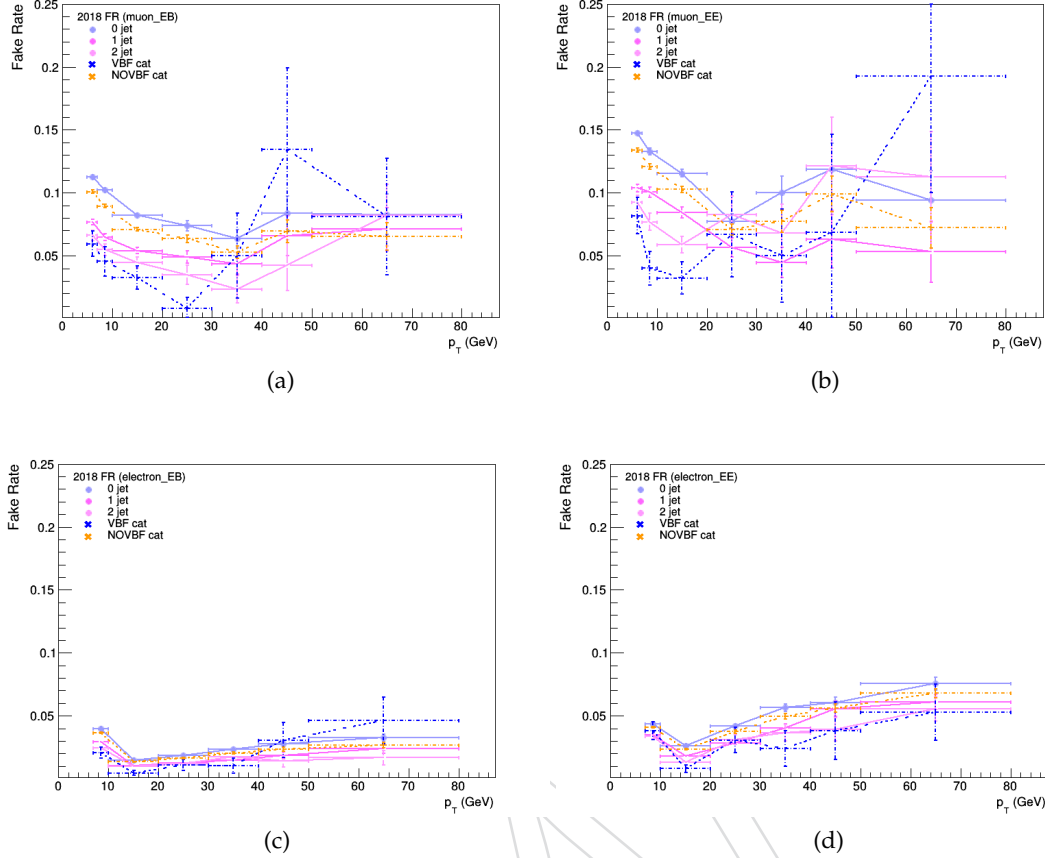


Figure 45: FR curves in the 0/1/2/VBF-tagged and non VBF-tagged categories for muons (top) and electrons (bottom) in the barrel (left) and endcap (right) region obtained using OS method.

Table 22: Comparison between the best-fit values and $\pm 1\sigma$ uncertainties for the expected and observed signal-strength modifiers, inflating ZX uncertainties in VBF categories by 100% and keeping nominal ZX uncertainties.

	Inflated ZX uncertainty		Nominal ZX uncertainty	
	Expected	Observed	Expected	Observed
$\mu_{t\bar{t}H,tH}$	$1.00^{+1.36}_{-0.78}$	$0.23^{+0.95}_{-0.23}$	$1.00^{+1.36}_{-0.78}$	$0.22^{+0.95}_{-0.22}$
μ_{WH}	$1.00^{+2.01}_{-1.00}$	$1.68^{+1.76}_{-1.44}$	$1.00^{+2.01}_{-1.00}$	$1.71^{+1.79}_{-1.71}$
μ_{ZH}	$1.00^{+8.33}_{-1.00}$	$0.00^{+5.24}_{-0.00}$	$1.00^{+8.33}_{-1.00}$	$0.00^{+5.44}_{-0.00}$
μ_{VBF}	$1.00^{+0.56}_{-0.46}$	$0.54^{+0.51}_{-0.41}$	$1.00^{+0.56}_{-0.46}$	$0.56^{+0.50}_{-0.41}$
$\mu_{ggH,b\bar{b}H}$	$1.00^{+0.16}_{-0.14}$	$1.02^{+0.15}_{-0.13}$	$1.00^{+0.16}_{-0.14}$	$1.03^{+0.15}_{-0.13}$

766 6.2.3 Shapes of the $m_{4\ell}$ distribution for the Reducible Background

767 In order to extract the shape of the $m_{4\ell}$ distribution for the reducible background used in the
 768 final analysis, shapes for each category and each final state are studied in the mass range [70,

300] GeV in both the SS and OS methods using 2016 dataset. Then the standard [105, 140] GeV window is used in the final analysis.

The study is focused on the SS method because of the better statistics available. A fit to Landau function is performed to provide the $m_{4\ell}$ shape in each category separately for the $4e$, 4μ , $2\mu 2e$ and $2e 2\mu$ final state, as shown in Figure ???. Since not all the categories are populated enough, the minimum number of events needed to extract the shape for a single category has been evaluated; therefore, in the very low populated categories (less than fifty events selected in the mass window) shapes obtained from the inclusive distributions in each final state are used. On one hand, the results from the two methods are found to be more or less identical in the 4μ and $2e 2\mu$ final states; on the other hand, there is some difference in the $4e$ and $2\mu 2e$ distributions but mainly due to a difference in the yields (Figure 46). Taking into account the merged $2e 2\mu$ and $2\mu 2e$ final state, a fit to Landau function is still performed to obtain the $m_{4\ell}$ shape: in fact, since the muon final state has a larger contribution, the addition of the $2\mu 2e$ component does not distort the single Landau shape.

Looking at the comparison between the $m_{4\ell}$ distribution for the $Z+X$ background obtained from the SS and OS methods in each category separately for all the final states, shape differences between the two methods are found to be not significant.

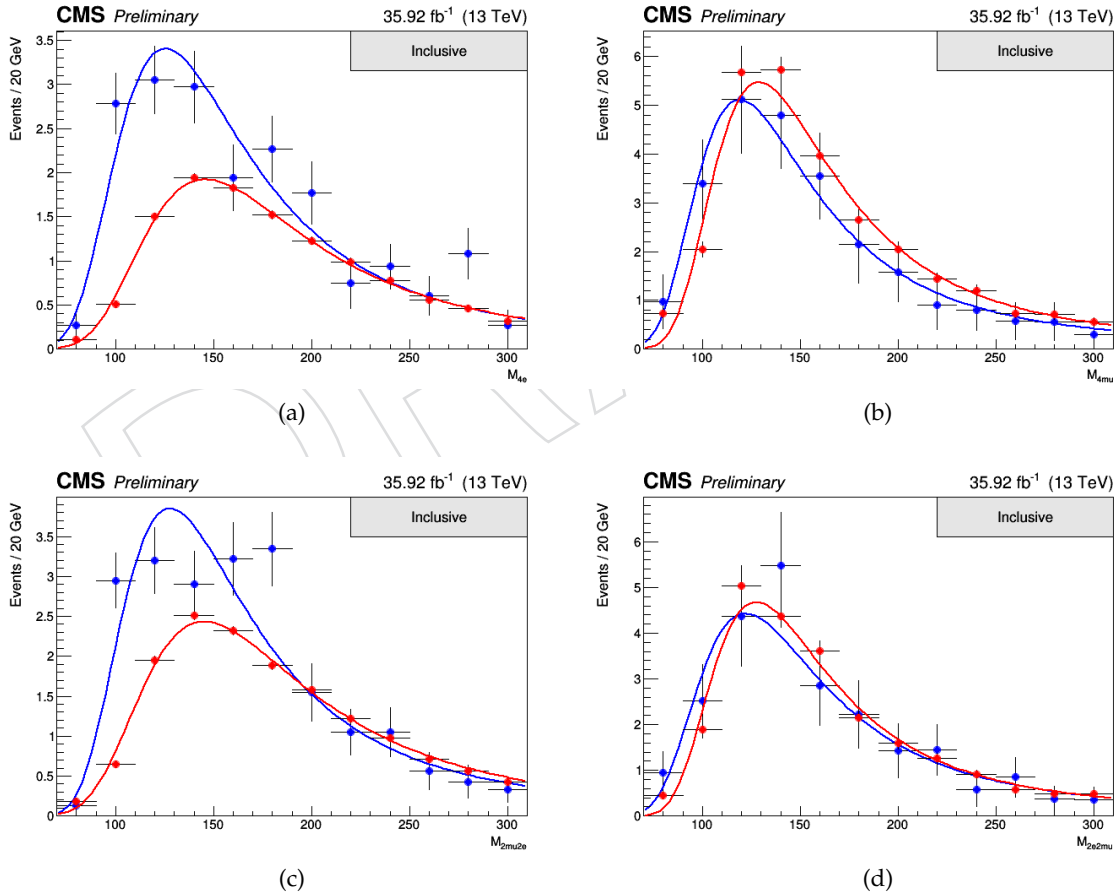


Figure 46: Comparison between the $m_{4\ell}$ distribution for the $Z+X$ reducible background obtained from the SS and OS methods (2016 dataset) in the inclusive category for each considered final state: $4e$ (a), 4μ (b), $2\mu 2e$ (c) and $2e 2\mu$ (d).

786 **6.2.4 Uncertainties on Reducible Background estimation methods**

787 One of the highest source of uncertainties in the analysis derives from the data-driven estimate
 788 of the reducible background. There are three different sources to be taken into account:

789 **Statistical uncertainty** The statistical uncertainty of the methods is driven by the limited
 790 size of the samples in the control regions where we measure ($Z + \ell$) and where we apply ($Z +$
 791 $\ell\ell$) the fake ratios and it is typically in the range of 1-10%.

792 **Systematic uncertainty due to fake rate variation** A systematic uncertainty given by the
 793 variation of the expected yield considering up and down variations in the fake rate measure-
 794 ment has to be taken into account.

795 **Systematic uncertainty due to background composition** The main source of the total
 796 uncertainty associated to the $Z+X$ estimate is due to the different composition of the reducible
 797 background processes ($DY, t\bar{t}, WZ, Z\gamma^{(*)}$) in the regions where we measure and where we
 798 apply the fake ratios. On one hand, the OS method corrects for the resulting bias via the “3P1F
 799 component” of its prediction. On the other had, the SS method corrects explicitly the electron
 800 fake rates by using the fraction of photon conversions, but no attempt is made to correct the
 801 muon fake rates. To evaluate the sensitivity of the estimate to background composition, the
 802 residual bias in the two methods can be estimated by measuring the fake ratios for individual
 803 background processes in the $Z + \ell$ region in simulated samples: the weighted average of these
 804 individual fake ratios is the fake rate that we measure in simulation. The exact composition of
 805 the background processes in the 2P+2F region where we plan to apply the fake ratios can be
 806 determined from simulation, thereby the individual fake ratios can be reweighted according to
 807 the 2P+2F composition. The difference between the reweighed fake ratio and the average value
 808 can be used as an estimate of the uncertainty on the measurement of the fake ratios. The effect
 809 of this systematic uncertainty is propagated to the final estimates, and it amounts to about 32%
 810 for $4e$, 33% for $2e2\mu$ and 35% for 4μ final state.

811 The final uncertainty associated to the combined $Z+X$ yield is given by the sum in quadrature
 812 of these three contributions considering the full mass range of the m_{4l} distribution in the SS
 813 method. Table 23 shows the $Z+X$ uncertainty for each final state in each year.

Channel	$4e$	4μ	$2e2\mu$
2016	41%	30%	35%
2017	38%	30%	33%
2018	37%	30%	33%

Table 23: Systematic uncertainty associated to the $Z+X$ estimate for each final state in all three years.

814 A shape uncertainty is not associated to the $Z+X$ estimate. In order to evaluate the uncertainty
 815 on the m_{4l} shape, we checked the difference between the shapes of predicted background dis-
 816 tributions for all three channels and between the shapes given by SS and OS methods. The
 817 uncertainty is estimated to be roughly in the range of 5% - 15%. Given that the difference of
 818 the shapes slowly varies with m_{4l} , it is taken as a constant versus m_{4l} and is absorbed into the
 819 much larger uncertainty on the predicted yield of background events.

6.2.5 Combination

Two methods for the reducible background estimation are presented with associated uncertainties in the previous sections. Table 24 shows the summary of the results given by the two methods combination for each year. The shape systematic uncertainty is absorbed in the statistical and systematic uncertainties on the estimated yields, and the total uncertainties are found to be of the order of 35–45%. Predictions of the two methods are combined assuming no correlation between the uncertainties (independent control regions, partially different sources systematics), and combined mean values are obtained by weighting the individual means according to the corresponding variances. For the final modelling of the background, the shape obtained from the SS method is taken in the mass range [105, 140] GeV: this is due to the better statistics available in the SS distributions; moreover, studies presented in the previous section 6.2.3 show no significant differences from the OS method. Figure 47 shows the shape obtained for one of the STXS categories as an example for each considered final state.

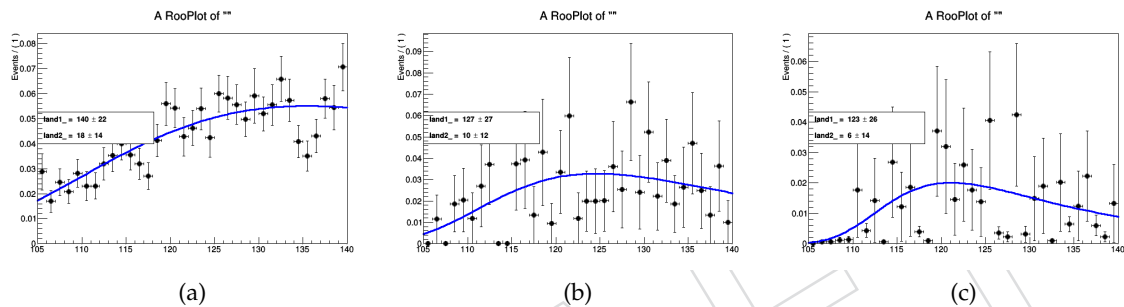


Figure 47: Shape of the $Z+X$ background events in the mass range [105, 140] GeV for the $ggH_0j_{10_200}$ category in the $4e$ final state (a), for the $ggH_1j_{60_120}$ category in the 4μ final state (b) and for the $VBF_2j_mjj_GT350_3j$ in the $2e2\mu$ final state (c).

If very low populated categories (less than fifty events selected in the mass window) are considered, shapes obtained from the inclusive distributions in the given final state are used. This shape is finally scaled to the yield obtained from the combination of the SS and OS method results. The yield uncertainty of 40% is able to cover all the discrepancies from the two methods, indeed shape uncertainty is not included.

6.3 Rare Backgrounds

The triboson backgrounds ZZZ , WZZ , and WWZ and $t\bar{t}Z$, $t\bar{t}WW$, and $t\bar{t}ZZ$ processes are also considered. These rare backgrounds are all estimated from simulation and are commonly referred to as the electroweak (EWK) backgrounds.

2016	4e	4μ	$2e2\mu$
Method OS	$20.2 \pm 6.2_{\text{tot.}}$	$27.0 \pm 8.6_{\text{tot.}}$	$47.7 \pm 10.5_{\text{tot.}}$
Method SS	$13.1 \pm 5.5_{\text{tot.}}$	$29.6 \pm 9.0_{\text{tot.}}$	$41.5 \pm 10.3_{\text{tot.}}$
Combined	16.1	28.2	44.4
2017	4e	4μ	$2e2\mu$
Method OS	$16.2 \pm 5.0_{\text{tot.}}$	$32.7 \pm 10.3_{\text{tot.}}$	$45.7 \pm 10.2_{\text{tot.}}$
Method SS	$10.9 \pm 4.1_{\text{tot.}}$	$33.4 \pm 10.3_{\text{tot.}}$	$40.8 \pm 9.7_{\text{tot.}}$
Combined	13.0	33.1	43.1
2018	4e	4μ	$2e2\mu$
Method OS	$25.4 \pm 7.7_{\text{tot.}}$	$50.1 \pm 15.5_{\text{tot.}}$	$67.7 \pm 14.8_{\text{tot.}}$
Method SS	$16.1 \pm 5.9_{\text{tot.}}$	$51.9 \pm 15.8_{\text{tot.}}$	$60.7 \pm 14.2_{\text{tot.}}$
Combined	19.4	50.7	63.9

Table 24: Summary of the results given by the two methods for the prediction of the contribution of reducible background processes in the signal region for all three years. The weighted mean value of the results of the two methods is taken as the final estimate of this contribution, while the uncertainty of the result covers the uncertainties of both methods. The table shows symmetric individual uncertainties for the two methods, while these are treated as asymmetric in the combination and statistical analysis. Results are given for an integrated luminosity of 35.9, 41.5 and 59.7 fb^{-1} in 2016, 2017 and 2018 data, respectively.

842 7 Signal Modelling

843 7.1 Signal modeling of the SM Higgs

844 7.1.1 Signal Corrections

845 For the dominant gluon fusion production mode for the signal, the p_T spectrum has been tuned
 846 using the “hfact” parameter of POWHEG to match closely the Higgs boson p_T spectrum in the
 847 full phase space as predicted by the HRES generator at $\sqrt{s} = 13$ TeV [58]. The agreement can
 848 be seen in Fig. 48. For other mass points, the “hfact” parameter is parametrized as a function
 849 of $m(H)$ as $\text{hfact} = 0.1 \cdot m(H) + 37.5$.

850 We use weights defined in bins of generated Higgs pT and number of generated jets to reweight
 851 our POWHEG signal sample to the NNLOPS one.

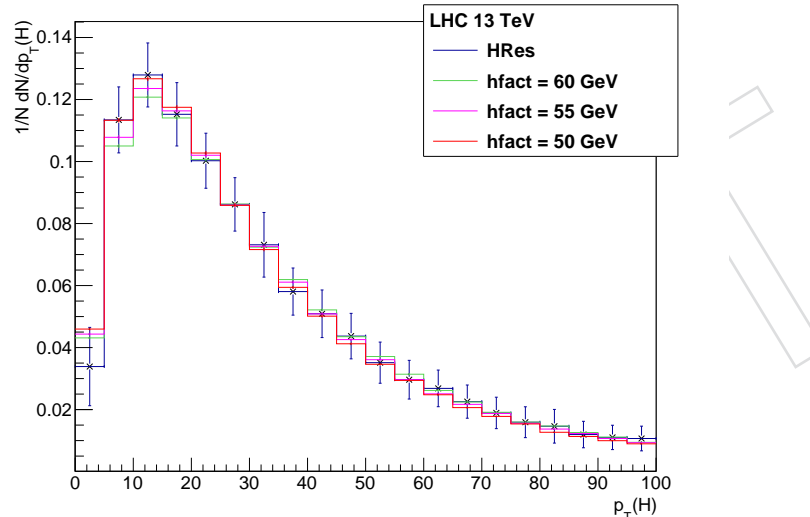


Figure 48: Comparison of POWHEG and HRES p_T spectrum at 13 TeV for different hfact.

852 7.1.2 Signal Normalization

853 The normalization of the Higgs boson signal in the peak region is directly taken from simula-
 854 tion. Using simulated samples for five m_H points (120, 124, 125, 126 and 130 GeV), polynomial
 855 fits of the expected signal yields in a [105, 140] GeV $m_{4\ell}$ window around the Higgs boson peak
 856 are performed.

857 **7.1.3 Signal Lineshape**

In this section we describe the PDF used to describe the signal shapes for different masses in different Event Categories as explained before. The resolution function model depends only on the leptons quality, while the exact shape depends on the lepton kinematics, and so depend also on the Higgs mass. A Double Crystal-Ball function $f_{dCB}(m_{4\ell} | m_H)$:

$$dCB(\xi) = N \cdot \begin{cases} A \cdot (B + |\xi|)^{-n_L}, & \text{for } \xi < \alpha_L \\ A \cdot (B + |\xi|)^{-n_R}, & \text{for } \xi > \alpha_R \\ \exp(-\xi^2/2), & \text{for } \alpha_L \leq \xi \leq \alpha_R \end{cases} \quad (7)$$

858 where $\xi = (m_{4\ell} - m_H - \Delta m_H)/\sigma_m$. This function has six independent parameters, and is in
 859 intended to capture the Gaussian core (σ_m) of the four-lepton mass resolution function, systematic
 860 mass shift Δm_H of the peak, and the left- and right-hand tail originating from leptons emitting
 861 bremsstrahlung in the tracker material, present for both electrons and muons, and from the non-Gaussian
 862 mis-measurements specific to interactions of electrons with the detector material (two parame-
 863 ters, n and α , for each side of the mean): The prominence of the left-,right-hand tail is defined
 864 by the power n_L, n_R , respectively. The parameters α_L, α_R define where the splicing of the tails and
 865 the core are made, in units of σ_m . Parameters A and B are not independent; they are defined
 866 by requiring the continuity of the function itself and its first derivatives. N is the normalizing
 867 constant.

868 The fitting strategy used to deal with this situation is to use the linear approximation of all the
 869 Double Crystal Ball parameters varying with m_H .

$$params = params_{CB0} + params_{CB1} \times (m_H - 125\text{GeV}) + params_{CB2} \times (m_H - 125\text{GeV})^2 \quad (8)$$

870 Simultaneous fits are performed using 5 mass samples to extract the $params_{CB0}$, $params_{CB1}$ and
 871 $params_{CB2}$. The initial value for the $params_{CB0}$ is obtained by fitting 125 GeV mass sample alone,
 and refitted in the simultaneous fits.

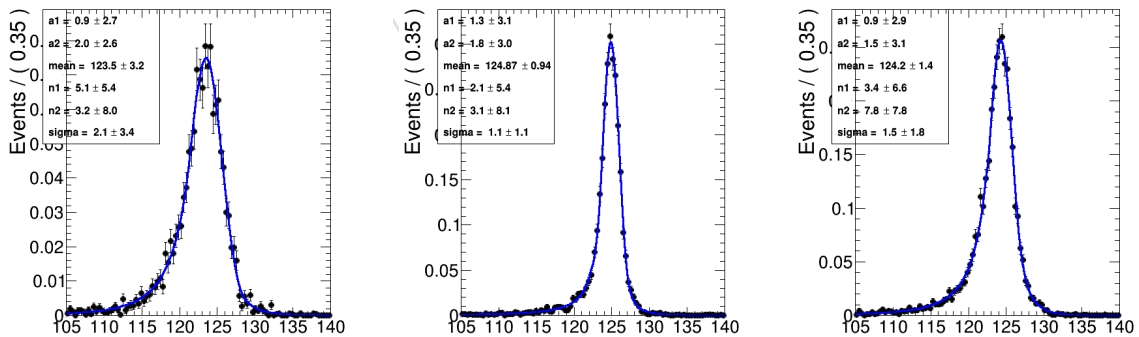


Figure 49: Probability density functions $f(m_{4l}|m_H)$ for signal with $m_H=125$ GeV at the re-
 construction level after the full lepton and event selections are applied. The distributions ob-
 tained from 13 TeV ggH MC samples are fitted with the model described in the text for 4 μ
 (left), 4e (center) and 2e2 μ (right) events. The distribution show the events in the stage 1.1 bin
 ggH_0j_0..10.

8 Systematic uncertainties

The main experimental uncertainties which affect both signal and background are the uncertainty on the integrated luminosity (from 2.3% to 2.6%, depending on the data taking period) and the uncertainty on the lepton identification and reconstruction efficiency (ranging from 1 to 2.5% and from 11 to 15.5% on the overall yields, in the 4μ and $4e$ channels, respectively). Experimental uncertainties for the reducible background estimation, described in Section 6.1.1, vary between 6% to 32% from the variation of the fake rates. The mismatch in the composition of backgrounds between the samples where the fake rate is derived and where it is applied accounts for about 30%.

The uncertainty of the lepton energy scale is assessed by propagating down to the four-leptons invariant mass the uncertainty associated the lepton momentum corrections on each individual lepton. The uncertainty is treated as uncorrelated (all up or all down). The new four-leptons invariant mass obtained this way is then fitted with only the mean value floating. The difference between the new mean value and the default one gives an estimation of the impact of the lepton energy scale. The values are reported in the Table 25, together with the estimation of the impact of lepton momentum resolution, following a similar procedure.

Table 25: Difference (in %) between the nominal mean and width of the four-leptons Higgs mass distribution and those where the lepton momentum scale and resolution uncertainties have been propagated.

	4e	4μ	$2e2\mu$
Scale Difference (%)	0.087	0.049	0.069
Resolution Difference (%)	17	12	17

The results obtained this way suggest that the uncertainties from 2016 (20% on the resolution, 0.3% for the $4e$ channel for scale) are still valid.

Theoretical uncertainties which affect both the signal and background estimation include uncertainties from the renormalization and factorization scale and choice of PDF set. The uncertainty from the renormalization and factorization scale is determined by varying these scales between 0.5 and 2 times their nominal value while keeping their ratio between 0.5 and 2. In the case of ggF production mode, the QCD scale uncertainty is broken down to 9 different sources. The renormalization and factorization scale affect the overall cross section, the migration of the stage1.1 bins in different Higgs pT and number of jets, top loop effects are treated as independent uncertainties, and correlated among different stage 1.1 bins. The numbers are shown in Fig ???. The uncertainty from the PDF set is determined by taking the root mean square of the variation when using different replicas of the default NNPDF set. PDF uncertainty arises from uncertainty is also taken into account. On the background, an additional uncertainty of 10% on the K factor used for the $gg \rightarrow ZZ$ prediction is applied as described in Section 6.1. A systematic uncertainty of 2% on the branching ratio of $H \rightarrow ZZ \rightarrow 4\ell$ only affects the signal yield. In the case of event categorization, experimental and theoretical uncertainties which account for possible migration of signal and background events between categories are included. The main sources of uncertainty on the event categorization include the QCD scale, PDF set, and the modeling of hadronization and the underlying event. These uncertainties amount to between 4–20% for the signal and 3–20% for the background depending on the category. The lower range corresponds to the VBF and VH processes and the upper range corresponds to the $gg \rightarrow H$ process yield in the VBF-2jet-tagged category. Additional uncertainties come from the imprecise knowledge of the jet energy scale (from 2% for the $gg \rightarrow H$ yield in the untagged category to 22% for $gg \rightarrow H$ yield in the VBF-2jet-tagged category) and b-tagging efficiency

913 and mistag rate (up to 10% in the $t\bar{t}H$ -tagged category). In the cross section measurement, the
 914 signal cross section uncertainties arise from theoretical sources are removed.

Table 26: Summary of the experimental systematic uncertainties in the $H \rightarrow 4\ell$ measurements of 2016, 2017 and 2018 data.

Summary of relative systematic uncertainties			
Common experimental uncertainties			
	2016	2017	2018
Luminosity	2.6 %	2.3 %	2.5 %
Lepton identification/reconstruction efficiencies	1.2 – 15.5 %	1.1 – 12 %	0.7 – 11 %
Background related uncertainties			
Reducible background ($Z+X$)	31 – 42 %	31 – 38 %	31 – 37 %
Signal related uncertainties			
Lepton energy scale	0.04 – 0.3 %	0 %	0 %
Lepton energy resolution	20 %	20 %	20 %

Table 27: Summary of the theory systematic uncertainties in the $H \rightarrow 4\ell$ measurements for the inclusive analysis

Summary of inclusive theory uncertainties	
QCD scale (gg)	± 3.9 %
PDF set (gg)	± 3.2 %
Bkg K factor (gg)	± 10 %
QCD scale (VBF)	+0.4/-0.3 %
PDF set (VBF)	± 2.1 %
QCD scale (WH)	+0.5/-0.7 %
PDF set (WH)	± 1.9 %
QCD scale (ZH)	+3.8/-3.1 %
PDF set (ZH)	± 1.6 %
QCD scale ($t\bar{t}H$)	+5.8/-9.2 %
PDF set ($t\bar{t}H$)	± 3.6 %
BR($H \rightarrow ZZ \rightarrow 4\ell$)	2 %
QCD scale ($q\bar{q} \rightarrow ZZ$)	+3.2/-4.2 % %
PDF set ($q\bar{q} \rightarrow ZZ$)	+3.1/-3.4 %
Electroweak corrections ($q\bar{q} \rightarrow ZZ$)	± 0.1 %

915 8.1 Systematic uncertainties treatment when combining the data sets

916 In this Section we describe how different systematic uncertainties are treated when combining
 917 the data sets. The theoretical uncertainties are correlated. All the experimental systematics are
 918 treated independently.

9 Yields and distributions

In this section we summarize the status of the analysis after selection, showing the inputs to the final results, namely the event yields and errors in the full signal region and in a restricted $m_{4\ell}$ range, and the distributions of the main kinematic variables in data and MC.

9.1 Signal Region Yields

The number of candidates observed in data and the expected yields for the backgrounds and Higgs boson signal after the full event selection are reported in Table 28 for the full range of $m_{4\ell}$. Table ?? shows the expected and observed yields for each of the 22 event categories, for a $118 < m_{4\ell} < 130$ GeV mass window around the Higgs boson peak.

Table 28: The number of expected background and signal events and number observed candidates after full analysis selection, for each final state, for the full mass range $m_{4\ell} > 70$ GeV, for an integrated luminosity of 137 fb^{-1} . Signal and ZZ backgrounds are estimated from Monte Carlo simulation, Z+X is estimated from data.

Channel	4μ	$4e$	$2e2\mu$	$4l$
qqZZ	1414.85	748.64	1835.05	3998.54
ggZZ	268.48	163.45	399.78	831.70
ZX	112.84	48.62	151.71	313.18
EW bkg	15.13	12.73	27.83	55.69
Sum of backgrounds	1811.30	973.45	2414.36	5199.11
Signal ($m_H = 125$ GeV)	95.27	46.01	118.53	259.82
Total expected	1906.57	1019.46	2532.90	5458.93
Data	1970	1032	2646	5648

9.2 Signal Region Distributions

The reconstructed four-lepton invariant mass distribution is shown in Figure 50 for the full dataset, and compared to expectations from the SM backgrounds, first for the full mass range, and then zooming on the low-mass range and high-mass range. In Figure 51, the same distributions are shown split by final state ($4e$, 4μ , and $2e2\mu$), for the two same mass ranges. In Figure ??, they are split by event category, for the low-mass range. The SM background distributions are obtained combining the rate normalization from data-driven methods and knowledge on shapes taken from the MC samples.

The reconstructed dilepton invariant masses selected as Z_1 and Z_2 are shown in Figures ?? together with their correlation, both full range of $m_{4\ell}$ and focusing on a $118 < m_{4\ell} < 130$ GeV mass window around the Higgs boson peak. Similarly, the decay discriminant $\mathcal{D}_{\text{bkg}}^{\text{kin}}$, $\mathcal{D}_{\text{bkg}}^{\text{VBF+dec}}$ and $\mathcal{D}_{\text{bkg}}^{\text{VH+dec}}$ are shown in Fig. ??, ?? and ?? in this window. The four production mechanism discriminant $\mathcal{D}_{2\text{jet}}$, $\mathcal{D}_{1\text{jet}}$, \mathcal{D}_{WH} , and \mathcal{D}_{ZH} are shown in Fig. ?? in the $118 < m_{4\ell} < 130$ GeV mass window, for events with at least two selected jets (except $\mathcal{D}_{1\text{jet}}$ which is for events with exactly one selected jet). Their correlations with $m_{4\ell}$ are shown in Fig. ??.

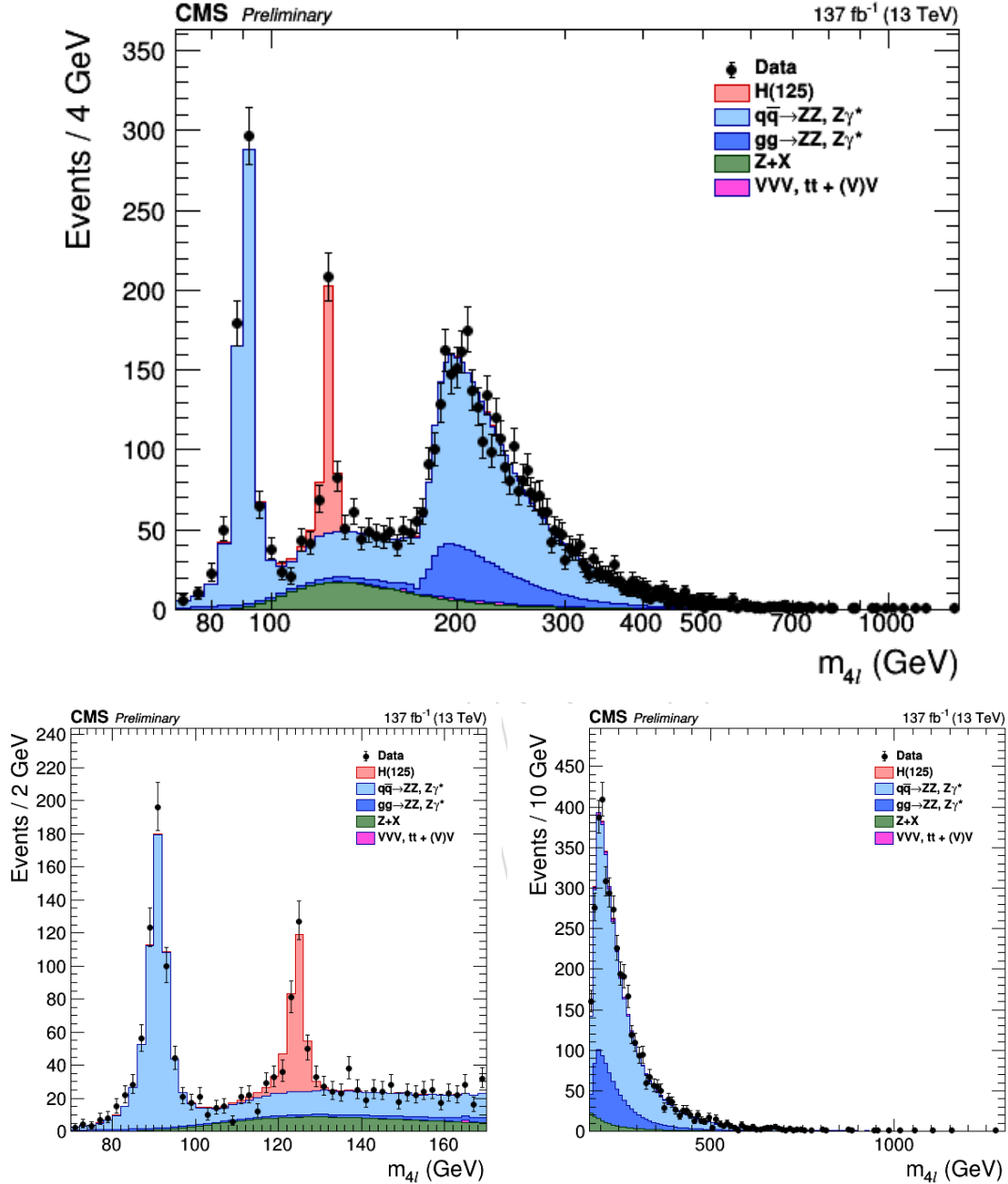


Figure 50: Distribution of the four-lepton reconstructed invariant mass m_{4l} in the full mass range (top) and the low-mass range (bottom left) and high-mass range (bottom right). Points with error bars represent the data and stacked histograms represent expected distributions. The 125 GeV Higgs boson signal and the ZZ backgrounds are normalized to the SM expectation, the $Z + X$ background to the estimation from data.

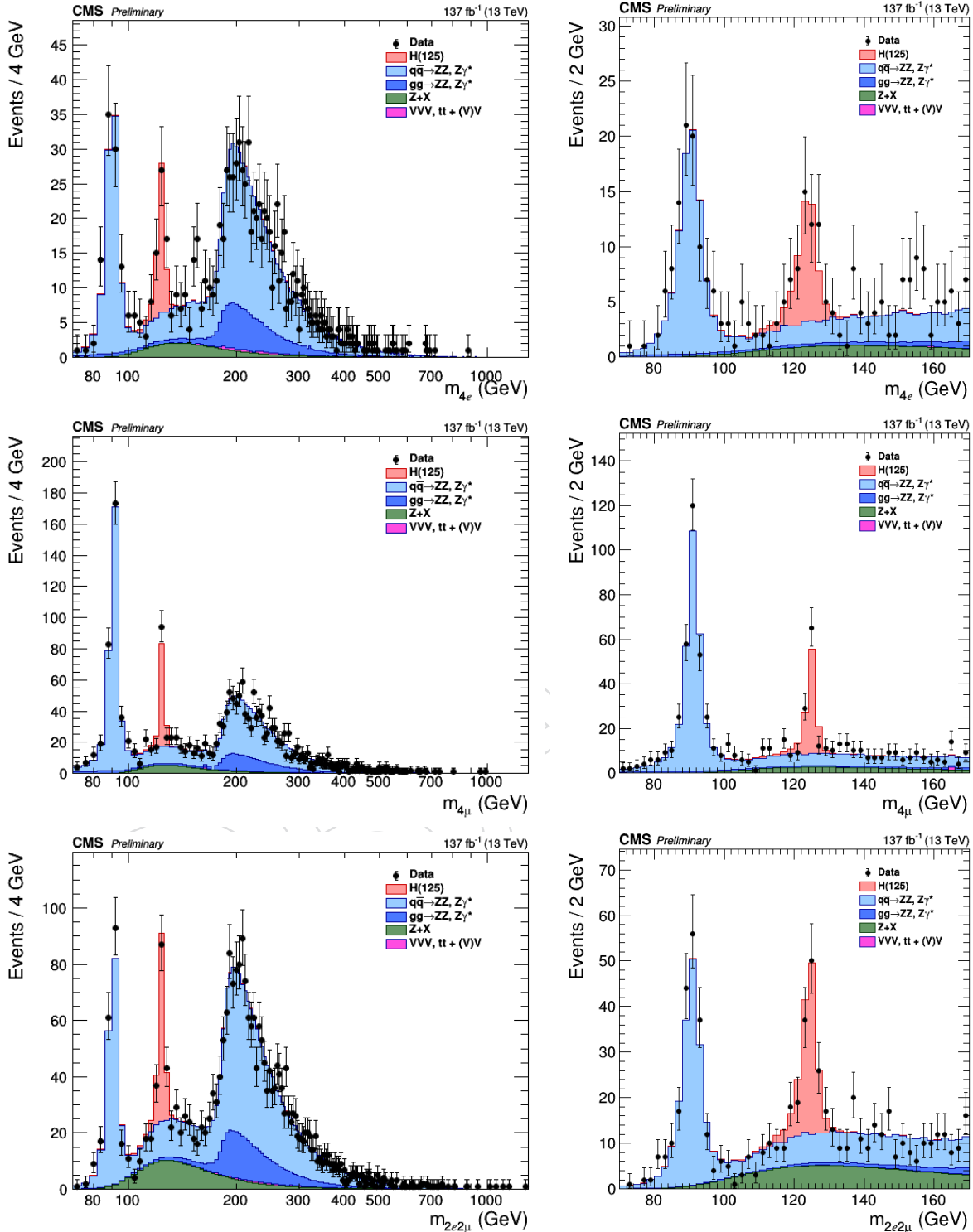
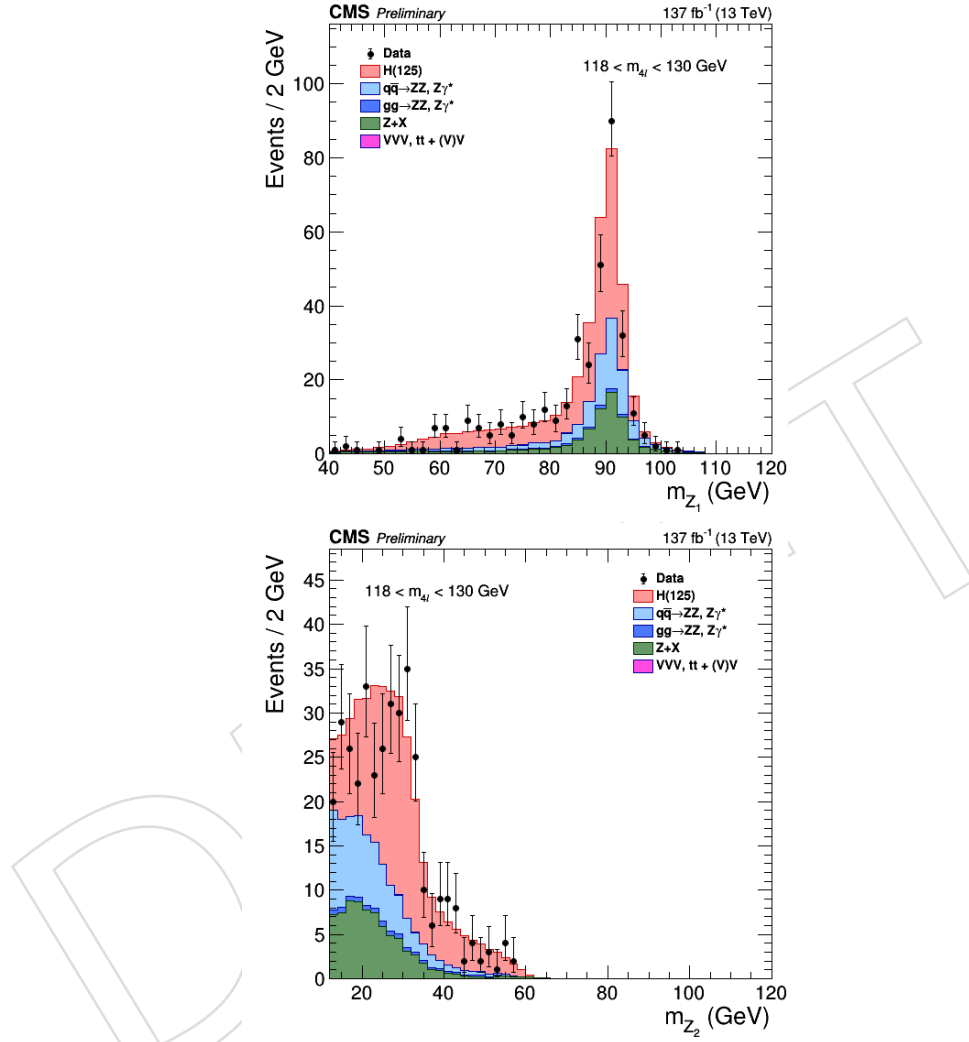


Figure 51: Distribution of the four-lepton reconstructed mass in several sub-channels: $4e$ (top), 4μ (middle), $2e2\mu$ for the low-mass range (bottom) for the full mass range (left) and the low-mass range (right).



Distribution of the Z_1 (left) and Z_2 (right) reconstructed invariant masses for the full mass range (left) and the low mass ($118 < m_{4\ell} < 130$ GeV) range (right). The stacked histograms and the gray scale represent expected distributions, and points represent the data. The 125 GeV Higgs boson signal and the ZZ backgrounds are normalized to the SM expectation, the $Z+X$ background to the estimation from data.

944 10 Results

945 In this section, we describe the methods used for the estimation of the significance of the ex-
946 cess of events above the SM backgrounds observed in the low-mass region, and of the signal
947 strength, i.e. its cross section normalized to the one expected for a SM Higgs.

948 To exploit all the properties of the resonance under study or search, a multi-dimensional fit is
949 implemented. For each of the categories defined in Section ??, the variable used in the maxi-
950 mum likelihood fit is:

- 951 1. The four-lepton mass without kinematic refitting $m_{4\ell}$,

DRAFT

952 10.1 Differential Cross Sections and EFT interpretations

953 **FIXME: Results to be updated with final processing**

954 **10.1.1 Fiducial Volume Definition**

955 The fiducial volume is defined to match closely the reconstruction level selection and is very
 956 similar to the definition used in Refs. [18]. With respect to the Run 1 analysis, the leptons are
 957 defined as “dressed” leptons rather than Born level leptons. Leptons are dressed by adding the
 958 four-momenta of leptons within $\Delta R < 0.3$ to the bare leptons. The fiducial lepton isolation cri-
 959 teria is also updated to match the Run 2 reconstruction level isolation. Leptons are considered
 960 isolated at generator level if the sum p_T of particles within a cone $\Delta R < 0.3$ is less than 0.35. The
 961 fiducial volume definition can be seen in Table 29. The fiducial volume acceptance for various
 962 SM production modes can be seen in Table 32.

Table 29: Summary of requirements and selections used in the definition of the fiducial phase space for the $H \rightarrow 4\ell$ cross section measurements.

Requirements for the $H \rightarrow 4\ell$ fiducial phase space	
Lepton kinematics and isolation	
leading lepton p_T	$p_T > 20 \text{ GeV}$
next-to-leading lepton p_T	$p_T > 10 \text{ GeV}$
additional electrons (muons) p_T	$p_T > 7(5) \text{ GeV}$
pseudorapidity of electrons (muons)	$ \eta < 2.5(2.4)$
p_T sum of all stable particles within $\Delta R < 0.3$ from lepton	less than $0.35 \cdot p_T$
Event topology	
existence of at least two SFOS lepton pairs, where leptons satisfy criteria above	
inv. mass of the Z_1 candidate	$40 \text{ GeV} < m(Z_1) < 120 \text{ GeV}$
inv. mass of the Z_2 candidate	$12 \text{ GeV} < m(Z_2) < 120 \text{ GeV}$
distance between selected four leptons	$\Delta R(\ell_i \ell_j) > 0.02$ for any $i \neq j$
inv. mass of any opposite sign lepton pair	$m(\ell^+ \ell^-) > 4 \text{ GeV}$
inv. mass of the selected four leptons	$105 \text{ GeV} < m_{4\ell} < 140 \text{ GeV}$
the selected four leptons must originate from the $H \rightarrow 4\ell$ decay	

963 **10.1.2 Measurement Strategy**

964 We measure the integrated and differential fiducial cross section for $pp \rightarrow H \rightarrow 4\ell$ by performing
 965 a maximum likelihood fit of the signal and background parameterisations to the observed
 966 4ℓ mass distribution, $N_{\text{obs}}(m_{4\ell})$, and the fiducial cross section (σ_{fid}) is directly extracted from
 967 the fit. The systematic uncertainties are included in the form of nuisance parameters and are
 968 effectively integrated out in the fit procedure. The results are obtained using an asymptotic
 969 approach [59] with a test statistic based on the profile likelihood ratio [60]. This procedure
 970 for the unfolding of the detector effects from the observed distributions is the same as in
 971 Refs. [18] and [61]. In the case of the differential cross section measurements, the finite effi-
 972 ciencies and resolution effects are encoded in a detector response matrix which describes how
 973 events migrate from a given observable bin at the fiducial level to a given bin at the recon-
 974 struction level. This matrix is diagonally dominant, with sizeable off-diagonal elements for
 975 observables involving jets.

976 Following the models for signal and background contributions described above, the number of
 977 expected events in each final state f and in each bin i of a considered observable is expressed as

978 a function of $m_{4\ell}$ given by:

$$\begin{aligned} N_{\text{obs}}^{\text{f},i}(m_{4\ell}) &= N_{\text{fid}}^{\text{f},i}(m_{4\ell}) + N_{\text{nonfid}}^{\text{f},i}(m_{4\ell}) + N_{\text{nonres}}^{\text{f},i}(m_{4\ell}) + N_{\text{bkg}}^{\text{f},i}(m_{4\ell}) \\ &= \epsilon_{i,j}^{\text{f}} \cdot \left(1 + f_{\text{nonfid}}^{\text{f},i}\right) \cdot \sigma_{\text{fid}}^{\text{f},j} \cdot \mathcal{L} \cdot \mathcal{P}_{\text{res}}(m_{4\ell}) \\ &\quad + N_{\text{nonres}}^{\text{f},i} \cdot \mathcal{P}_{\text{nonres}}(m_{4\ell}) + N_{\text{bkg}}^{\text{f},i} \cdot \mathcal{P}_{\text{bkg}}(m_{4\ell}), \end{aligned} \quad (9)$$

979 The parameter $\sigma_{\text{fid}}^{\text{f},j}$ is the signal cross section in bin j of the fiducial phase space, and it is the
980 parameter extracted from the measurement.

981 The shape of the resonant signal contribution, $\mathcal{P}_{\text{res}}(m_{4\ell})$, is described by a double-sided Crystal
982 Ball function as described in Section 7.1.3 whose normalisation is proportional to the fiducial
983 cross section. The shape of the non-resonant signal contribution, $\mathcal{P}_{\text{nonres}}(m_{4\ell})$, which arises
984 from WH, ZH, and $t\bar{t}H$ production where one of the leptons from the Higgs boson decay is
985 lost or not selected, is empirically modelled by a Landau distribution whose shape parameters
986 are constrained in the fit to be within a range determined from simulation. This contribution
987 is treated as a background and hereafter we will refer to this contribution as the “non-resonant
988 signal” contribution.

989 The $\epsilon_{i,j}^{\text{f}}$ represents the detector response matrix that maps the number of expected events in
990 a given observable bin j at the fiducial level to the number of expected events in the bin i at
991 the reconstruction level. The f_{nonfid}^i fraction describes the ratio of the non-fiducial and fiducial
992 signal contribution in bin i at the reconstruction level. The efficiency is measured using signal
993 simulation samples and corrected for residual differences between data and simulation. In
994 the case of the integrated fiducial cross section measurement the efficiencies reduce to a single
995 values.

996 An additional resonant contribution arises from events which are reconstructed but which do
997 not originate from the fiducial phase space. These events are due to detector effects which
998 cause differences between the quantities used for the fiducial phase space definition and the
999 analogous quantities at the reconstruction level. This contribution is treated as background
1000 and is referred to as the “non-fiducial signal” contribution. The shape of these events is verified
1001 using simulation to be identical to the shape of the fiducial signal and its normalisation is fixed
1002 to be a fraction of the fiducial signal component. The value of this fraction, which we denote
1003 by f_{nonfid} , which has been determined from simulation for each of the studied signal models.

1004 The variation between different models of the factor in the final column of Table 32, $(1 +$
1005 $f_{\text{nonfid}})\epsilon$, is directly related to the model dependence of the measurement. The model de-
1006 pendence is defined as the variation of the factor $(1 + f_{\text{nonfid}})\epsilon$ when the relative fraction of
1007 each the production modes are varied within their experimental constraints. An increase in
1008 model dependence compared to Run 1 is observed when using the ZZ candidate selection at
1009 reconstruction level where the the candidate with the best $D_{\text{bkg}}^{\text{kin}}$ discriminant value is chosen.
1010 Therefore the fiducial cross section measurement is performed with a different event selection
1011 algorithm than the other measurements, namely that the ZZ candidate selection is made using
1012 the same algorithm as in Run 1.

1013 Examples of the efficiency matrices for gluon fusion and VBF production can be seen in Fig. 52.
1014 The matrices for the p_{TH} and $N(\text{jets})$ observables are shown.

Table 30: Summary of different Standard Model signal models. The MC samples are from 2016 production.

Signal process	\mathcal{A}_{fid}	ϵ	f_{nonfid}	$(1 + f_{\text{nonfid}})\epsilon$
Individual Higgs boson production modes				
gg \rightarrow H (POWHEG)	0.398	0.592 ± 0.001	0.049 ± 0.001	0.621 ± 0.001
VBF (POWHEG)	0.445	0.601 ± 0.002	0.038 ± 0.001	0.624 ± 0.002
WH (POWHEG+MINLO)	0.314	0.577 ± 0.002	0.068 ± 0.001	0.616 ± 0.002
ZH (POWHEG+MINLO)	0.342	0.592 ± 0.003	0.071 ± 0.002	0.634 ± 0.003
ttH (POWHEG)	0.311	0.572 ± 0.003	0.136 ± 0.003	0.650 ± 0.004

Table 31: Summary of different Standard Model signal models. The MC samples are from 2017 production.

Signal process	\mathcal{A}_{fid}	ϵ	f_{nonfid}	$(1 + f_{\text{nonfid}})\epsilon$
Individual Higgs boson production modes				
gg \rightarrow H (POWHEG)	0.404 ± 0.001	0.593 ± 0.001	0.054 ± 0.001	0.625 ± 0.001
VBF (POWHEG)	0.443 ± 0.001	0.605 ± 0.002	0.045 ± 0.001	0.632 ± 0.002
WH (POWHEG+MINLO)	0.329 ± 0.001	0.589 ± 0.002	0.080 ± 0.001	0.637 ± 0.002
ZH (POWHEG+MINLO)	0.341 ± 0.002	0.593 ± 0.003	0.083 ± 0.002	0.643 ± 0.004
ttH (POWHEG)	0.316 ± 0.002	0.597 ± 0.003	0.172 ± 0.004	0.700 ± 0.004

Table 32: Summary of different Standard Model signal models. The MC samples are from 2018 production. **FIXME: Scale factors not yet applied**

Signal process	\mathcal{A}_{fid}	ϵ	f_{nonfid}	$(1 + f_{\text{nonfid}})\epsilon$
Individual Higgs boson production modes				
gg \rightarrow H (POWHEG)	0.403 ± 0.001	0.630 ± 0.001	0.055 ± 0.001	0.664 ± 0.001
VBF (POWHEG)	0.443 ± 0.001	0.645 ± 0.002	0.043 ± 0.001	0.673 ± 0.002
WH (POWHEG+MINLO)	0.330 ± 0.001	0.632 ± 0.002	0.075 ± 0.001	0.679 ± 0.002
ZH (POWHEG+MINLO)	0.338 ± 0.002	0.638 ± 0.003	0.086 ± 0.003	0.693 ± 0.004
ttH (POWHEG)	0.314 ± 0.002	0.620 ± 0.003	0.184 ± 0.004	0.733 ± 0.004

10.1.3 Measurement results

- 1015 1016 The result of the simultaneous fit to to the $m_{4\ell}$ spectrum is shown for each final state in Fig. 53.
1017 The fiducial cross section using this defintion is measured to be:

$$2.85^{+0.24}_{-0.23}(\text{stat.})^{+0.15}_{-0.14}(\text{sys.}) \text{ fb} \quad (10)$$

- 1018 This can be compared to the SM expectation of $\sigma_{\text{fid.}}^{\text{SM}} = 2.72 \pm 0.14 \text{ fb}$.
1019 The expected differential cross section results can be seen in Fig. 57.

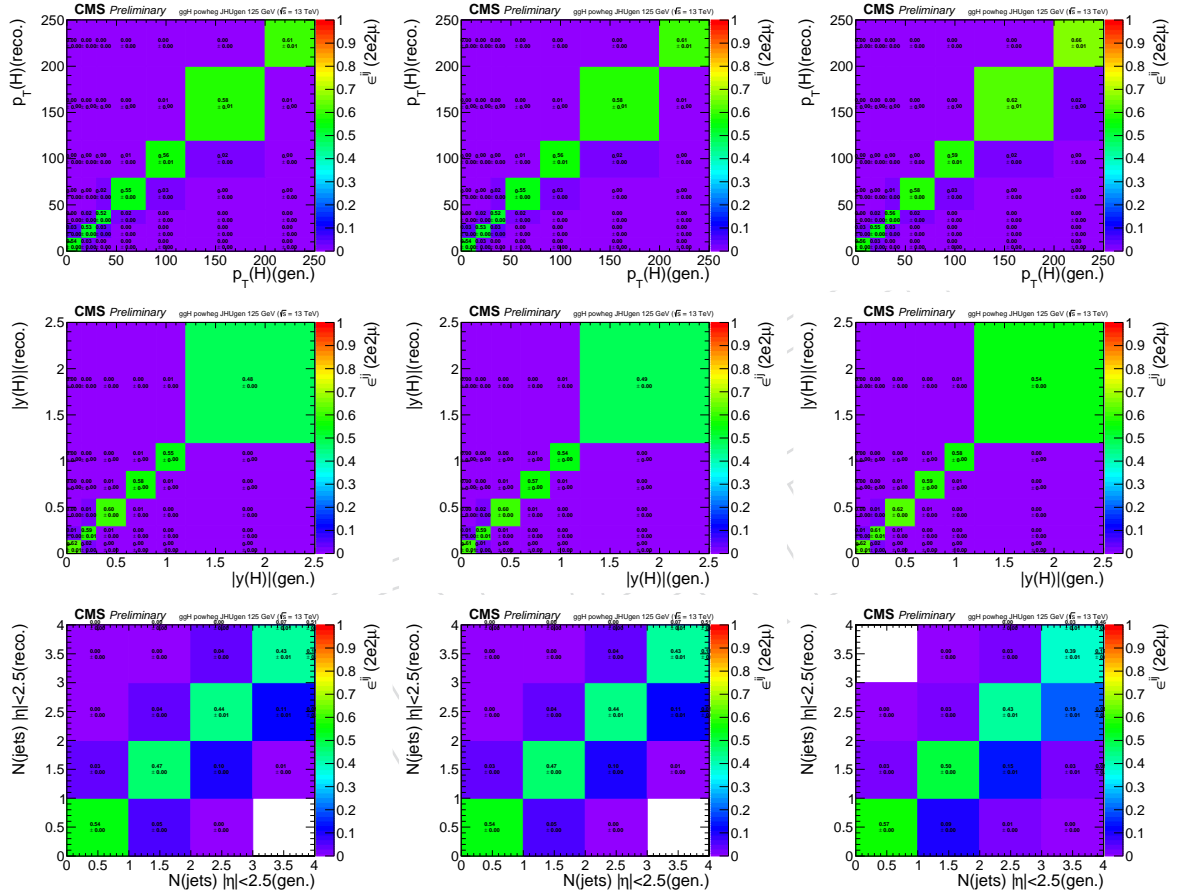


Figure 52: Efficiency matrices for the p_{TH} (top) and yH (middle) and $N(\text{jets})$ (bottom) observables for gluon fusion production modes in the $2e2\mu$ final state in 2016 (left) 2017 (middle) and 2018 (right).

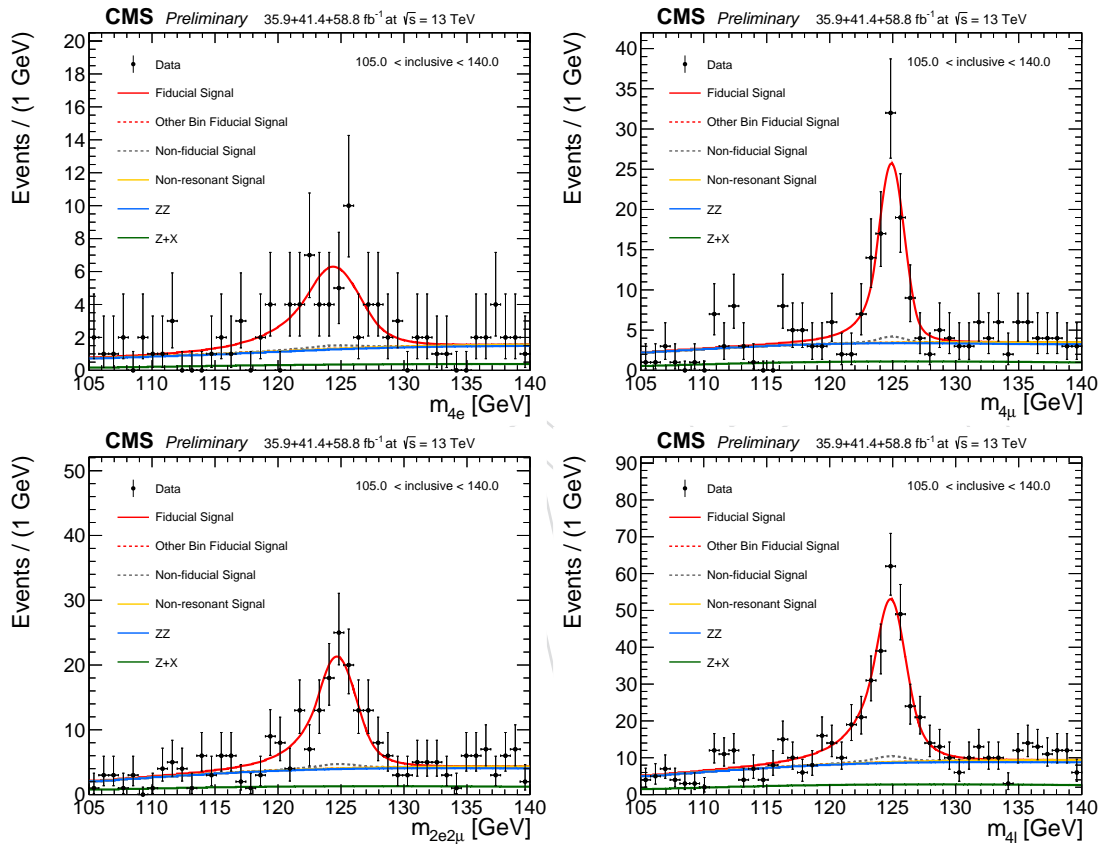


Figure 53: Result of simultaneous fit for the integrated fiducial cross section measurement in each final state. The results are shown for 2018 only.

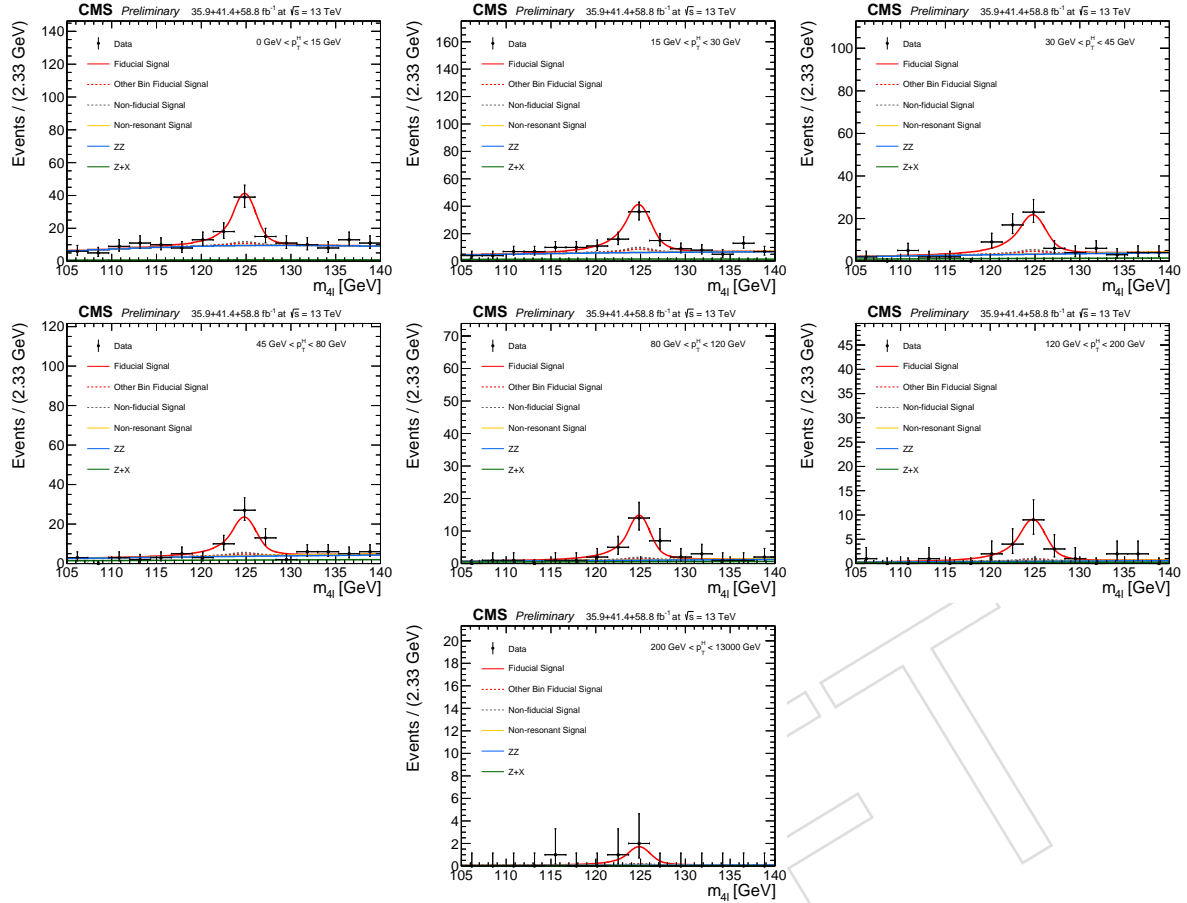


Figure 54: Result of simultaneous fit for the differential fiducial cross section measurement for $p_T(H)$ in each differential bin. The combined 4ℓ final state is shown. The results are shown for 2018 only.

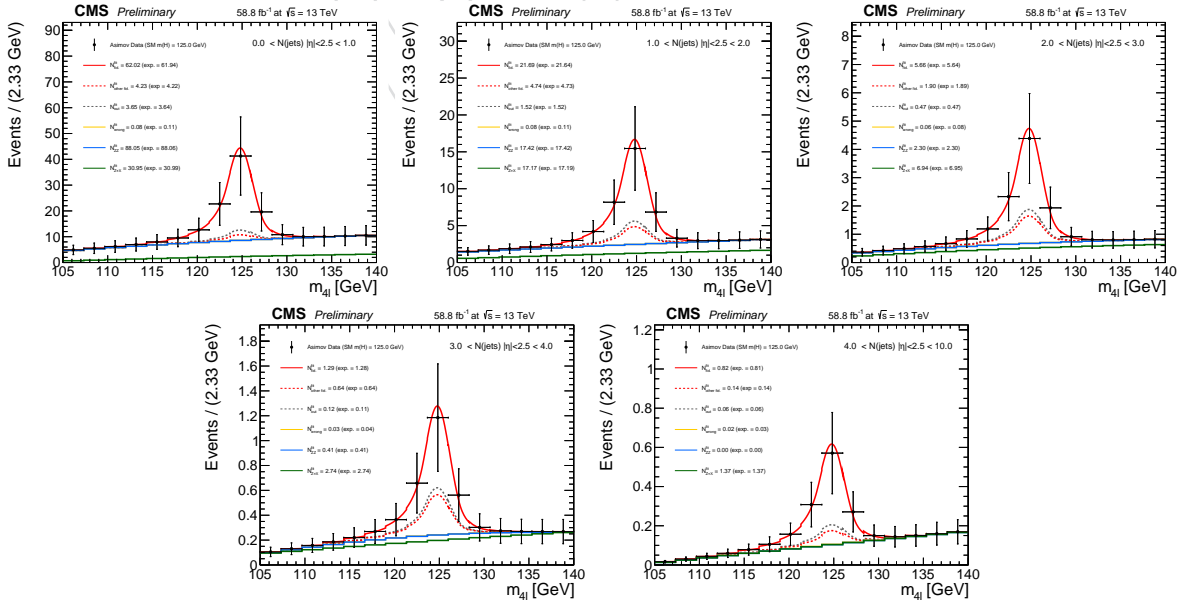


Figure 55: Result of simultaneous fit for the differential fiducial cross section measurement for $N(\text{jets})$ in each differential bin. The combined 4ℓ final state is shown. The results are shown for 2018 only.

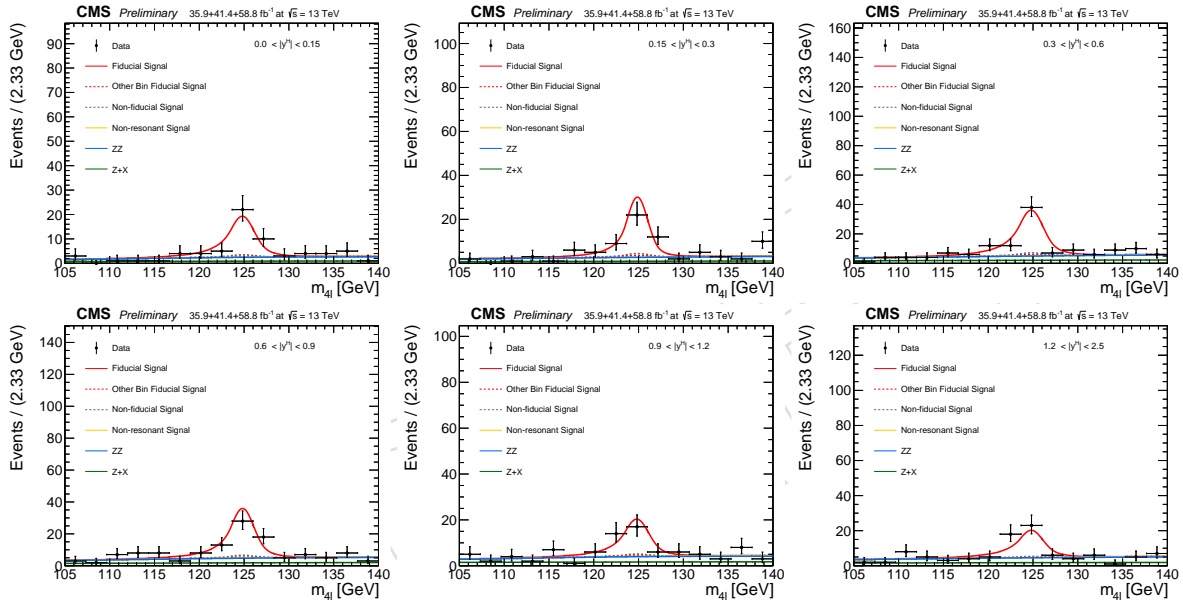


Figure 56: Result of simultaneous fit for the differential fiducial cross section measurement for $y(H)$ in each differential bin. The combined 4ℓ final state is shown. The results are shown for 2018 only.

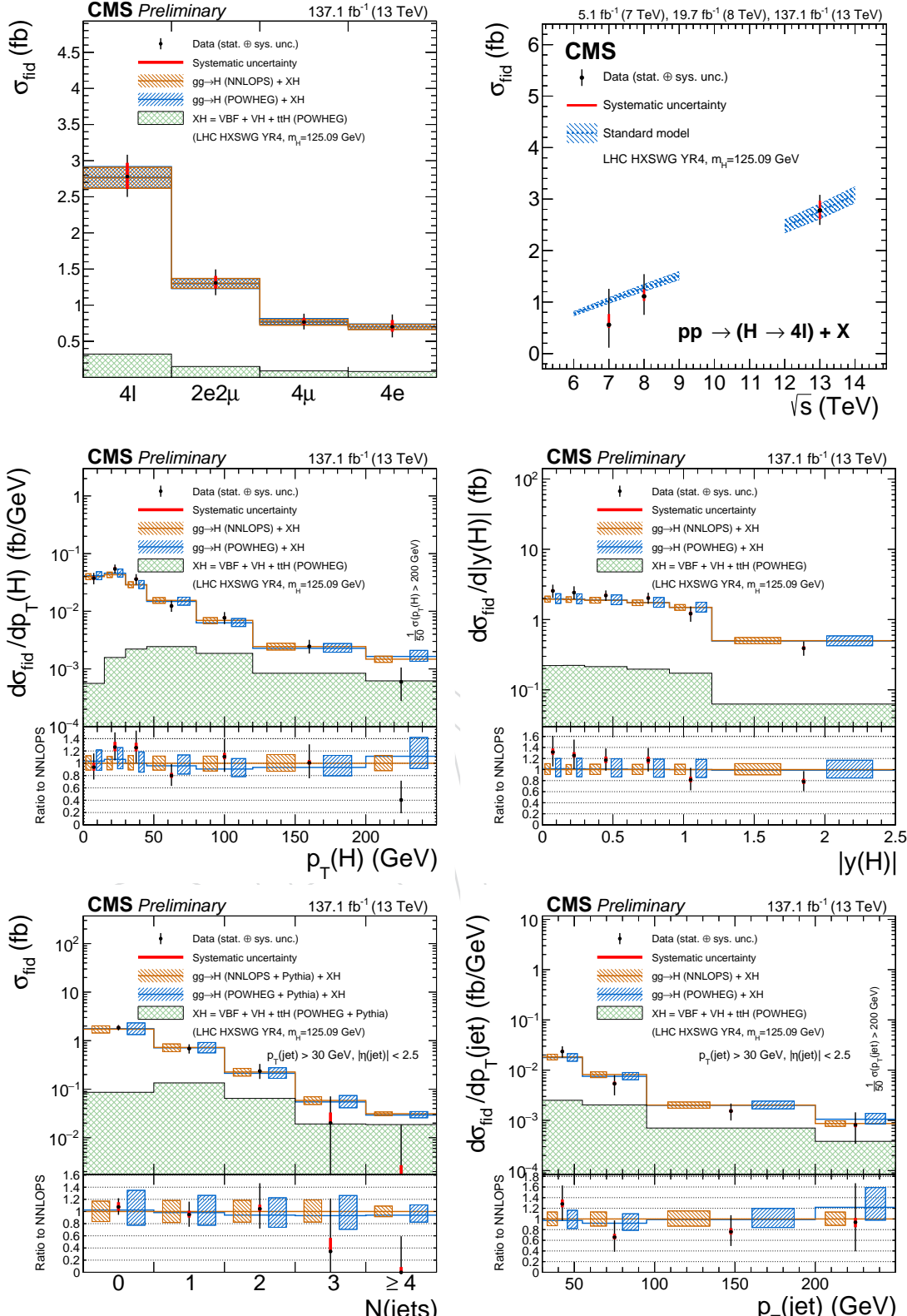


Figure 57: The measured inclusive fiducial cross section in different final states (top left). The measured fiducial cross section as a function of \sqrt{s} (top right). The acceptance is calculated using POWHEG at $\sqrt{s}=13$ TeV and HRES [56?] at $\sqrt{s}=7$ and 8 TeV and the total gluon fusion cross section and uncertainty are taken from Ref. [?]. The fiducial volume for $\sqrt{s}=6-9$ TeV uses the lepton isolation definition from Ref. [18], while for $\sqrt{s}=12-14$ TeV the definition described in the text is used. The results of the differential cross section measurement for $p_T(H)$ (middle left), $|y(H)|$ (middle right) and $N(\text{jets})$ (bottom left), p_T of the leading jet (bottom right). The acceptance and theoretical uncertainties in the differential bins are calculated using POWHEG. The sub-dominant component of the signal (VBF + VH + tH) is denoted as XH.

References

- [1] CMS Collaboration, "Observation of a new boson at a mass of 125 GeV with the CMS experiment at the LHC", *Phys. Lett. B* **716** (2012) 30,
doi:10.1016/j.physletb.2012.08.021, arXiv:1207.7235.
- [2] ATLAS Collaboration, "Observation of a new particle in the search for the Standard Model Higgs boson with the ATLAS detector at the LHC", *Phys. Lett. B* **716** (2012) 1,
doi:10.1016/j.physletb.2012.08.020, arXiv:1207.7214.
- [3] F. Englert and R. Brout, "Broken Symmetry and the Mass of Gauge Vector Mesons", *Phys. Rev. Lett.* **13** (1964) 321, doi:10.1103/PhysRevLett.13.321.
- [4] P. W. Higgs, "Broken symmetries, massless particles and gauge fields", *Phys. Lett.* **12** (1964) 132, doi:10.1016/0031-9163(64)91136-9.
- [5] P. W. Higgs, "Broken Symmetries and the Masses of Gauge Bosons", *Phys. Rev. Lett.* **13** (1964) 508, doi:10.1103/PhysRevLett.13.508.
- [6] G. Guralnik, C. Hagen, and T. Kibble, "Global Conservation Laws and Massless Particles", *Phys. Rev. Lett.* **13** (1964) 585, doi:10.1103/PhysRevLett.13.585.
- [7] P. W. Higgs, "Spontaneous Symmetry Breakdown without Massless Bosons", *Phys. Rev.* **145** (1966) 1156, doi:10.1103/PhysRev.145.1156.
- [8] T. Kibble, "Symmetry breaking in nonAbelian gauge theories", *Phys. Rev.* **155** (1967) 1554, doi:10.1103/PhysRev.155.1554.
- [9] CMS Collaboration, "Precise determination of the mass of the Higgs boson and tests of compatibility of its couplings with the standard model predictions using proton collisions at 7 and 8 TeV", *Eur. Phys. J. C* **75** (2015) 212,
doi:10.1140/epjc/s10052-015-3351-7, arXiv:1412.8662.
- [10] ATLAS Collaboration, "Measurements of the Higgs boson production and decay rates and coupling strengths using pp collision data at $\sqrt{s} = 7$ and 8 TeV in the ATLAS experiment", *Eur. Phys. J. C* **76** (2016) doi:10.1140/epjc/s10052-015-3769-y,
arXiv:1507.04548.
- [11] ATLAS, CMS Collaboration, "Combined Measurement of the Higgs Boson Mass in pp Collisions at $\sqrt{s} = 7$ and 8 TeV with the ATLAS and CMS Experiments", *Phys. Rev. Lett.* **114** (2015) 191803, doi:10.1103/PhysRevLett.114.191803, arXiv:1503.07589.
- [12] CMS Collaboration, "Measurements of the Higgs boson production and decay rates and constraints on its couplings from a combined ATLAS and CMS analysis of the LHC pp collision data at $\sqrt{s} = 7$ and 8 TeV", CMS Physics Analysis Summary CMS-PAS-HIG-15-002, 2015.
- [13] CMS Collaboration, "Measurement of the properties of a Higgs boson in the four-lepton final state", *Phys. Rev. D* **89** (2014) 092007, doi:10.1103/PhysRevD.89.092007,
arXiv:1312.5353.
- [14] CMS Collaboration, "Study of the Mass and Spin-Parity of the Higgs Boson Candidate via Its Decays to Z Boson Pairs", *Phys. Rev. Lett.* **110** (2013) 081803,
doi:10.1103/PhysRevLett.110.081803, arXiv:1212.6639.

- [15] CMS Collaboration, "Constraints on the spin-parity and anomalous HVV couplings of the Higgs boson in proton collisions at 7 and 8 TeV", *Phys. Rev. D* **92** (2015) 012004, doi:10.1103/PhysRevD.92.012004, arXiv:1411.3441.
- [16] CMS Collaboration, "Constraints on the Higgs boson width from off-shell production and decay to Z-boson pairs", *Phys. Lett. B* **736** (2014) 64, doi:10.1016/j.physletb.2014.06.077, arXiv:1405.3455.
- [17] CMS Collaboration, "Limits on the Higgs boson lifetime and width from its decay to four charged leptons", *Phys. Rev. D* **92** (2015) 072010, doi:10.1103/PhysRevD.92.072010, arXiv:1507.06656.
- [18] CMS Collaboration, "Measurement of differential and integrated fiducial cross sections for higgs boson production in the four-lepton decay channel in pp collisions at $\sqrt{s} = 7$ and 8 tev", arXiv:1512.08377.
- [19] CMS Collaboration, "Measurements of properties of the higgs boson in the four-lepton final state at $\sqrt{s}=13$ tev with full run ii data", CMS Physics Analysis Summary CMS-PAS-HIG-19-001, 2019.
- [20] PPD, "Ppd twiki for 2016 data and mc samples", *CMS Twiki* (2018).
- [21] I. Brivio, Y. Jiang, and M. Trott, "The SMEFTsim package, theory and tools", *JHEP* **12** (2017) 070, doi:10.1007/JHEP12(2017)070, arXiv:1709.06492.
- [22] J. Aebischer et al., "WCxf: an exchange format for Wilson coefficients beyond the Standard Model", *Comput. Phys. Commun.* **232** (2018) 71–83, doi:10.1016/j.cpc.2018.05.022, arXiv:1712.05298.
- [23] S. Alioli, P. Nason, C. Oleari, and E. Re, "NLO vector-boson production matched with shower in POWHEG", *JHEP* **07** (2008) 060, doi:10.1088/1126-6708/2008/07/060, arXiv:0805.4802.
- [24] P. Nason, "A new method for combining NLO QCD with shower Monte Carlo algorithms", *JHEP* **11** (2004) 040, doi:10.1088/1126-6708/2004/11/040, arXiv:hep-ph/0409146.
- [25] S. Frixione, P. Nason, and C. Oleari, "Matching NLO QCD computations with parton shower simulations: the POWHEG method", *JHEP* **11** (2007) 070, doi:10.1088/1126-6708/2007/11/070, arXiv:0709.2092.
- [26] E. Bagnaschi, G. Degrassi, P. Slavich, and A. Vicini, "Higgs production via gluon fusion in the POWHEG approach in the SM and in the MSSM", *JHEP* **02** (2012) 088, doi:10.1007/JHEP02(2012)088, arXiv:1111.2854.
- [27] P. Nason and C. Oleari, "NLO Higgs boson production via vector-boson fusion matched with shower in POWHEG", *JHEP* **02** (2010) 037, doi:10.1007/JHEP02(2010)037, arXiv:0911.5299.
- [28] H. B. Hartanto, B. Jager, L. Reina, and D. Wackerlo, "Higgs boson production in association with top quarks in the POWHEG BOX", *Phys. Rev. D* **91** (2015), no. 9, 094003, doi:10.1103/PhysRevD.91.094003, arXiv:1501.04498.

- 1099 [29] G. Luisoni, P. Nason, C. Oleari, and F. Tramontano, “ $HW^\pm/\text{HZ} + 0$ and 1 jet at NLO with
 1100 the POWHEG BOX interfaced to GoSam and their merging within MiNLO”, *JHEP* **10**
 1101 (2013) 083, doi:10.1007/JHEP10(2013)083, arXiv:1306.2542.
- 1102 [30] Y. Gao et al., “Spin determination of single-produced resonances at hadron colliders”,
 1103 *Phys. Rev. D* **81** (2010) 075022, doi:10.1103/PhysRevD.81.075022,
 1104 arXiv:1001.3396. [Erratum: doi:10.1103/PhysRevD.81.079905].
- 1105 [31] NNPDF Collaboration, “Parton distributions for the LHC Run II”, *JHEP* **04** (2015) 040,
 1106 doi:10.1007/JHEP04(2015)040, arXiv:1410.8849.
- 1107 [32] P. Nason and G. Zanderighi, “ W^+W^- , WZ and ZZ production in the
 1108 POWHEG-BOX-V2”, *Eur. Phys. J.* **C74** (2014), no. 1, 2702,
 1109 doi:10.1140/epjc/s10052-013-2702-5, arXiv:1311.1365.
- 1110 [33] J. M. Campbell and R. K. Ellis, “MCFM for the Tevatron and the LHC”, *Nucl. Phys. Proc.
 1111 Suppl.* **205** (2010) 10, doi:10.1016/j.nuclphysbps.2010.08.011,
 1112 arXiv:1007.3492.
- 1113 [34] J. M. Campbell, R. K. Ellis, and C. Williams, “Bounding the Higgs width at the LHC
 1114 using full analytic results for $gg \rightarrow e^-e^+\mu^-\mu^+$ ”, *JHEP* **04** (2014) 060,
 1115 doi:10.1007/JHEP04(2014)060, arXiv:1311.3589.
- 1116 [35] J. Alwall et al., “The automated computation of tree-level and next-to-leading order
 1117 differential cross sections, and their matching to parton shower simulations”, *JHEP* **07**
 1118 (2014) 079, doi:10.1007/JHEP07(2014)079, arXiv:1405.0301.
- 1119 [36] CMS Collaboration, “Performance of electron reconstruction and selection with the CMS
 1120 detector in proton-proton collisions at $\sqrt{s} = 8$ TeV”, *JINST* **10** (2015) P06005,
 1121 doi:10.1088/1748-0221/10/06/P06005.
- 1122 [37] CMS Collaboration, “Measurement of the properties of the higgs boson in the four-lepton
 1123 final state at $\sqrt{s} = 13$ tev”, CMS Physics Analysis Note CMS-AN-15-277, 2016.
- 1124 [38] CMS Collaboration, “Measurement of the properties of the Higgs boson in the
 1125 four-lepton final state at $\sqrt{s} = 13$ TeV”, CMS Physics Analysis Note CMS-AN-15-277,
 1126 2016.
- 1127 [39] R. Salerno and M. Ahmad, “Measurements of properties of the Higgs boson in the
 1128 four-lepton final state at $\sqrt{s}=13$ TeV”, *CMS AN* **2016/442** (2016).
- 1129 [40] T. Sculac and D. Sperka, “Measurements of properties of the Higgs boson in the
 1130 four-lepton final state at $\sqrt{s}=13$ TeV with 2017 data”, *CMS AN* **2017/342** (2017).
- 1131 [41] CMS Collaboration, “New results on the study of higgs boson production in the
 1132 four-lepton final state at $\sqrt{s} = 13$ tev”, CMS Physics Analysis Note CMS-AN-16-217, 2016.
- 1133 [42] E. Brondolin and G. Petrucciani, “Measurement of the muon-tracking efficiency using the
 1134 tag and probe method on 2015 runii data”, *CMS AN* **2015/215** (2015).
- 1135 [43] JetMETPOG, “Jet id for 2018”, *CMS Twiki* (2018).
- 1136 [44] JetMETPOG, “Jet pu id for 2017”, *CMS Twiki* (2017).
- 1137 [45] JetMETPOG, “Jec mc for 2018”, *CMS Twiki* (2018).

- 1138 [46] PPD, “L1 pre-firing twiki recipe”, *CMS Twiki* (2018).
- 1139 [47] BTAGPOG, “B-tagging for 2018”, *CMS Twiki* (2018).
- 1140 [48] M. Grazzini, S. Kallweit, and D. Rathlev, “ZZ production at the LHC: Fiducial cross
1141 sections and distributions in NNLO QCD”, *Phys. Lett. B* **750** (2015) 407 – 410,
1142 doi:<http://dx.doi.org/10.1016/j.physletb.2015.09.055>,
1143 arXiv:1507.06257.
- 1144 [49] J. M. Campbell, R. K. Ellis, and C. Williams, “Vector boson pair production at the LHC”,
1145 *JHEP* **07** (2011) 018, doi:[10.1007/JHEP07\(2011\)018](https://doi.org/10.1007/JHEP07(2011)018), arXiv:1105.0020.
- 1146 [50] M. Bonvini et al., “Signal-background interference effects in $gg \rightarrow H \rightarrow WW$ beyond
1147 leading order”, *Phys. Rev. D* **88** (2013) 034032, doi:[10.1103/PhysRevD.88.034032](https://doi.org/10.1103/PhysRevD.88.034032),
1148 arXiv:1304.3053.
- 1149 [51] K. Melnikov and M. Dowling, “Production of two Z-bosons in gluon fusion in the heavy
1150 top quark approximation”, *Phys. Lett. B* **744** (2015) 43,
1151 doi:[10.1016/j.physletb.2015.03.030](https://doi.org/10.1016/j.physletb.2015.03.030), arXiv:1503.01274.
- 1152 [52] C. S. Li, H. T. Li, D. Y. Shao, and J. Wang, “Soft gluon resummation in the
1153 signal-background interference process of $gg(\rightarrow h^*) \rightarrow ZZ$ ”, (2015).
1154 arXiv:1504.02388.
- 1155 [53] G. Passarino, “Higgs CAT”, *Eur. Phys. J. C* **74** (2014) 2866,
1156 doi:[10.1140/epjc/s10052-014-2866-7](https://doi.org/10.1140/epjc/s10052-014-2866-7), arXiv:1312.2397.
- 1157 [54] S. Catani and M. Grazzini, “An NNLO subtraction formalism in hadron collisions and its
1158 application to Higgs boson production at the LHC”, *Phys. Rev. Lett.* **98** (2007) 222002,
1159 doi:[10.1103/PhysRevLett.98.222002](https://doi.org/10.1103/PhysRevLett.98.222002), arXiv:hep-ph/0703012.
- 1160 [55] M. Grazzini, “NNLO predictions for the Higgs boson signal in the $H \rightarrow WW \rightarrow l\nu l\nu$ and
1161 $H \rightarrow ZZ \rightarrow 4l$ decay channels”, *JHEP* **02** (2008) 043,
1162 doi:[10.1088/1126-6708/2008/02/043](https://doi.org/10.1088/1126-6708/2008/02/043), arXiv:0801.3232.
- 1163 [56] M. Grazzini and H. Sargsyan, “Heavy-quark mass effects in Higgs boson production at
1164 the LHC”, *JHEP* **09** (2013) 129, doi:[10.1007/JHEP09\(2013\)129](https://doi.org/10.1007/JHEP09(2013)129),
1165 arXiv:1306.4581.
- 1166 [57] LHC Higgs Cross Section Working Group, “Handbook of LHC Higgs Cross Sections: 3.
1167 Higgs Properties”, CERN Report CERN-2013-004, 2013.
1168 doi:[10.5170/CERN-2013-004](https://doi.org/10.5170/CERN-2013-004), arXiv:1307.1347.
- 1169 [58] HZZ, “Higgs boson transverse momentum in powheg and hres”, *CMS meeting* (2015).
- 1170 [59] ATLAS and CMS Collaborations, LHC Higgs Combination Group, “Procedure for the lhc
1171 higgs boson search combination in summer 2011”, ATL-PHYS-PUB/CMS NOTE 2011-11,
1172 2011/005, CERN, 2011.
- 1173 [60] G. Cowan, K. Cranmer, E. Gross, and O. Vitells, “Asymptotic formulae for
1174 likelihood-based tests of new physics”, *Eur. Phys. J. C* **71** (2011) 1554, doi:[10.1140/epjc/s10052-011-1554-0](https://doi.org/10.1140/epjc/s10052-011-1554-0),
1175 10.1140/epjc/s10052-013-2501-z,
1176 arXiv:1007.1727.
- 1177 [61] CMS Collaboration, “Measurement of differential cross sections for Higgs boson
1178 production in the diphoton decay channel in pp collisions at $\sqrt{s}=8$ TeV”, *Eur. Phys. J. C*
1179 **76** (2015) 13, doi:[10.1140/epjc/s10052-015-3853-3](https://doi.org/10.1140/epjc/s10052-015-3853-3), arXiv:1508.07819.